Development of systems based on visible light communications for high added value applications

by

JUAN SEBASTIAN BETANCOURT PERLAZA

A dissertation submitted in partial fulfillment of the requirements for the degree of Doctor of Philosophy in

Electrical Engineering, Electronics and Automation

Universidad Carlos III de Madrid

Advisor(s):
Dr. José Manuel Sánchez Pena
Dr. Juan Carlos Torres Zafra

Tutor:
Dr. José Manuel Sánchez Pena

October, 2023

"*To my wife Maria Soley, my brother Juan Manuel, and my parents Edith Beatriz and Carlos Alberto. To my grandparents.*"

Thank you!

Acknowledgements

First of all, I would like to thank God for guiding my path and allowing me to grow every day.

Although this thesis work is the conclusion of a part of my journey, this journey began a long time ago. At each stage of my life, very important people have helped me to grow, try, and never give up in my constant search for knowledge and experience. I cannot list all of these people here, but they are always in my mind and have helped shape the person I am today. Nevertheless, I will dedicate a few words to some of them.

Firstly, I would like to thank my wife, Maria Soley, for supporting me every day, not only in this project but in my life in general, for giving me strength, and for helping me to focus on the important things and never give up. Thanks also to my family, especially my parents and brother, who always look out for me and help me in any way they can, even if I never ask for it.

To my tutor Jose Manuel for belief in my capacity to conduct this work, to always be a helping hand, and be willing to share all his knowledge and experience. In this way, several professors have also been of great support and guidance, and with humility have share their knowledge and have work side by side with me. Thanks to Juan Carlos, Ricardo, Enrique, and Luis. Thanks also to Robert Schober for hosting me in Erlangen during my three months of visiting research.

I would also like to thank my lab mates, Randy, Carlos, and Lorena, for showing me different ways of thinking and making this work much easier by sharing their knowledge and time.

This work would not have been possible without the invaluable support of:

- Universidad Carlos III de Madrid
- The Photonic Displays and Applications (GDAF) group
- The Microelectronic Design and Applications (DMA) group
- The Institute for Digital Communications (IDC) from the Friedrich-Alexander-Universität Erlangen-Nürnberg

- SINFOTON2 program from Comunidad de Madrid (SINFOTON2-CM,S2018/ NMT-4326-SINFOTON2-CM)
- The CDTI (Centre for the Development of Industrial Technology, Ministerio de Ciencia e Innovación) throughthe European Regional Development Fund (ERDF)
- The Madrid Government (Comunidad de Madrid) under the Multiannual Agreement with UC3M in the line of “Fostering Young Doctors Research” (GEOVEOLUZCM-UC3M)
- The MEDIALIFI project (financed by OPTIVA MEDIA)

Published and submitted content

[1] Torres, Juan and Montes, Aitor and Mendoza, Sandra and Fernández, Pedro and **Betancourt Perlaza, Juan Sebastian** and Escandell Varela, Lorena and del Valle, Carlos and Sánchez-Pena, José. A Low-Cost Visible Light Positioning System for Indoor Positioning. Published in Sensors, 9 September 2020. doi: **10.3390/s20185145**.

- The content of this work is reported in Chapter 1.
- The role of the author in this publication was software design and visualization, mainly supporting the integration of the system with the smartphone and the Android application development.

[2] **Betancourt Perlaza, Juan S.** and Torres Zafra, Juan C. and Morales Céspedes, Máximo and Martínez-Sarriegui, Iñaki and del Valle, Carlos I. and Sánchez Pena, José M. An Enhanced Method for Dynamic Characterization of High-Power LEDs for Visible Light Communication Applications. Published in Electronics, 18 January 2022. doi: **10.3390/electronics11030292**.

- This work is partially included and its content is reported in Chapter 2.
- The role of the author in this publication was the co-conceptualization, software support, results visualization, and main writing, performing the testing of the different methods and also supporting the data acquisition to contrast the results of the newly proposed method and its effectiveness on LED characterization.

[3] **Betancourt P., Juan Sebastian** and Lozada Domínguez, Randy and San Millan Heredia, Enrique. Phase Characterization and Correction in a Hardware Implementation of an OFDM-Based System for VLC Applications. Published in IEEE Photonics Journal, 22 March 2023. doi: **10.1109/JPHOT.2023.3260447**.

- This work is partially included and its content is reported in Chapter 3.
- The role of the author in this publication was the co-conceptualization, data acquisition, algorithm implementation support, data visualization, results validation and main writing. The results of the paper have been

evaluated both in simulations and in a real optical system, different from the prototype developed in this thesis work.

[4] Lozada D., Randy and **Betancourt P., Juan Sebastian** and San Millán H., Enrique. Time Synchronization Technique Hardware Implementation for OFDM Systems with Hermitian Symmetry for VLC Applications. Published in IEEE Access, 27 April 2023. doi: **10.1109/ACCESS.2023.3271143**.

- This work is partially included and its content is reported in Chapter 3.
- The role of the author in this publication was the co-conceptualization, data collection and validation, and test environment setup. The results of the paper have been evaluated both in simulations and in a real optical system, different from the prototype developed in this thesis work.

Other research merits

[1] **Juan Sebastian Betancourt P.** and Juan C. Torres, Carlos Iván del Valle Morales, Iñaki Martínez Sarriegui and José Manuel Sánchez Pena. Low-Cost Visible Light Communication System for Indoor Positioning. LatinDisplay 2021, 17-19 March 2021, Brazil. The autor was the responsible of the poster presentation at the congress.

[2] **Juan S.Betancourt Perlaza** and Juan C. Torres and Máximo Morales and Iñaki Martínez-Sarriegui and Carlos I. del Valle and José M. Sánchez Pena. Characterization of high-power white leds for VLC applications. Published in Measurement: Sensors as part of the proceedings of IMEKO 2021 World Congress, December 2021. doi: **10.1016/j.measen.2021.100215**.

- The role of the author in this publication was co-design, visualization of results, and main writing. The autor was also the responsible of the poster presentation at the congress.

[3] **Perlaza, Juan S. Betancourt** and Zafra, Juan C. Torres and Morales-Cespedes, Máximo and Qidan, Ahmad Adnan and Bentura, Benjamín and Armada, Ana García and Pena, José M. Sánchez. Measurement of the Modulation Bandwidth of High-Power Chip-on-Board LEDs for VLC systems. Published in 2022 13th International Symposium on Communication Systems, Networks and Digital Signal Processing (CSNDSP), 20-22 July 2022, Porto, Portugal. doi: **10.1109/CSNDSP54353.2022.9908014**.

- The role of the author in this publication was the co-conceptualization, results visualization, and main writing. The autor was also the responsible of the poster presentation at the congress.

Abstract

The discovery of the blue Light-emitting diodes (LEDs) in the last decade of the last century changed the way we as a society approach the need for artificial lighting, as the combination of the blue light emitted by the LED with a yellow phosphor layer reactive to the blue wavelength generates white light. White LEDs are more efficient than incandescent bulbs and last longer, which is a benefit not only for the end user but for everyone as the energy used for lighting could be significantly reduced and therefore the impact on the environment. LEDs not only improve the efficiency of existing light bulbs, but because they are based on semiconductors, their switching speed is several orders of magnitude higher than other types of illumination technologies.

On the other hand, the radio frequency spectrum is becoming saturated due to the incredible rate at which more and more devices are being connected wirelessly. The growing market of Internet of things (IoT) devices and the concept of the smart home, where everything can be connected and controlled from the palm of your hand, has limited the available bandwidth for data exchange with the Internet. However, because wireless communications can penetrate walls and travel tens of meters, even in low-power devices, our devices are not the only ones fighting for a space to transmit information, but we share the available channel with all of our neighbors' devices. This ability of signals to cross physical borders also threatens our data security, as the data may be accessible to third parties.

Considering these two ideas, Visible light communication (VLC) is gaining a lot of interest in recent years, as it can provide a secure connection limited to the light spot where it is transmitted. In this way, LED bulbs will not only cover our need for lighting but also support part of the communication, helping to free up the radio frequency channel. VLCs also offers alternatives in places with high electromagnetic interference, and the bandwidth is fully available for each transmitter. VLC has also been recognized as a viable technology for indoor positioning, as the system can know where it is, based on transmitter localization (LED lamp). This is particularly useful because it can achieve centimeter accuracy, which is impossible with other positioning systems such as satellite navigation.

Therefore, this thesis work aims to design and develop a working VLC system that supports multiple end applications. The intended system must be small and

inexpensive to be attractive for future adaptations. With this we try to gain knowledge about the inherent challenges that VLC systems have and, with it, help VLC technology to go one step further to be useful and adaptable to our daily lives.

First, we realized that LEDs are a main element in any VLC system, and therefore the more knowledge we have about it, the better performance we can achieve with this type of solution. VLC uses Intensity modulation/Direct detection (IM/DD) to transmit information, and to do so, the intensity of the LED is varied over time by modulating the current injected into the device. For this reason, the knowledge of the electrical equivalent of the LEDs is a useful tool for the correct design of VLC systems. In this thesis work, we have proposed a method to electrically characterize high-power white LEDs and, with it, create an equivalent electrical circuit useful for simulation and driver design.

Then, we study the different modulation formats used in wireless communication channels and the modulation formats that can only be implemented with VLC, such as Color shift keying (CSK). In this aspect, we have noticed that even if the modulation formats are mature and well known, VLC channels present some peculiarities that need to be explored more deeply in order to adapt the modulations to this type of channel. In the case of this thesis, we explore the implementation of an Orthogonal frequency division multiplexing (OFDM) modulation in a VLC channel, and with it, we found a novel way to perform the time synchronization and phase correction in a pilot-based OFDM. The requirement that the transmitted signal be real was overcome by using the hermitian symmetry property of the Inverse fast Fourier transform (IFFT).

In summary, we were able to develop a working VLC system in all stages, hardware, firmware, and software, reaching transmission speeds up to 234 kbps. The system works with a custom Android application designed for this prototype. The received light information is transformed into bits at the receiver and then sent through Bluetooth low energy (BLE) to the Android device. The application processes the received data and displays useful information to the user. In this prototype, the information is used for indoor localization, but it is not limited to that. The system also supports the addition of Augmented reality (AR) glasses to enhance the user experience. The transmitter prototype is an LED bulb, which can be connected directly to the power grid with a GU-10 or GUZ-10 socket. The VLC receiver measures $34.5x46.6x17.6mm$, and it is powered by a CR2032 battery.

Contents

List of Figures

List of Tables

List of acronyms

VLC Visible light communication

OWC Optical wireless communication

FSO Free-Space optical ommunication

OCC Optical camera communication

LiFi Light-fidelity

WiFi Wireless-fidelity

LED Light-emitting diode

RF Radio frequency

RX Receiver

TX Transmitter

LTE Long-term Evolution

CRI Color Rendering Index

IR Infrared

PD Photodetector

TIA Transimpedance amplifier

PCB Printed Circuit Board

GBW Gain-bandwidth product

GPIO General-purpose Input/Output

BLE Bluetooth low energy

USB Universal Serial Bus

SWD Serial Wire Debug

SoC System on chip

FLL Frequency-Locked Loop

CSK Color shift keying

OOK On-Off keying

PAM Pulse amplitude modulation

PPM Pulse position modulation

VPPM Variable pulse position modulation

PWM Pulse width modulation

SNR Signal-to-noise ratio

LoS line-of-sight

FOV Field of view

APD Avalanche photodiode

DAC Digital-to-analog converter

MOSFET Metal-oxide-semiconductor field-effect transistor

FET Field-effect transistor

BJT Bipolar junction transistor

IRS Intelligent reflecting surface

MEMS Micro-electromechanical system

MOEMS Micro-opto-electromechanical system

AWGN Additive white Gaussian noise

IM/DD Intensity modulation/Direct detection

CoB Chip On Board

NRZ Non-return-to-zero

RZ Return-to-zero

LTI linear time-invariant

ISI Intersymbol interference

FDM Frequency division multiplexing

FSK Frequency shift keying

OFDM Orthogonal frequency division multiplexing

QAM Quadrature amplitude modulation

FFT Fast Fourier transform

IFFT Inverse fast Fourier transform

CP Cyclic prefix

CFO Carrier frequency offset

SFO Sampling frequency offset

PN Phase noise

DAC Digital-to-analogue converter

ADC Analogue-to-digital converter

MNC Maximum normalized correlation

PHY Physical Layer

MAC Media Access Control

DLL Data Link Layer

AR Augmented reality

VR Virtual reality

IoT Internet of things

M2M Machine-to-Machine

USRP Universal SoftwareRadio Peripheral

BER bit error rate

RLL Run Length Limiting

RD Running Disparity

SHR Synchronization Header

FLP Fast Locking Pattern

TDP Topology-dependent Pattern

PHR Physical Header

PSDU Physical Service Data Unit

MHR MAC Header

GATT Generic Attribute Profile

ATT Attribute protocol

UUID Universal Unique Identifier

OS Operative System

OCR Optical Character Recognition

LASER Light amplification by stimulated emission of radiation

API Application Programming Interface

IMU Inertial Measurement Unit

1 Introduction

The number of mobile connected devices will grow to be almost 13.1 billion devices, and there will be approximately 3.6 devices per capita in 2023. Forecasting a huge growth for IoT and Machine-to-Machine (M2M) [1]. The increase on mobile connected devices suggest that the saturation problems of the radio frequencies that we are experiencing will increase in the future.

Therefore, researchers have focused their efforts on new ways to use the available spectrum more efficiently and to explore new parts of the electromagnetic spectrum, shown in Fig. 1.1, as new communication channels. In this matter, the use of other wavelengths in the electromagnetic spectrum has been found to be a viable and feasible solution to alleviate the use of radio frequencies. One of the important aspects that have limited the expansion to other frequency ranges has been the impact on human health or low speeds.

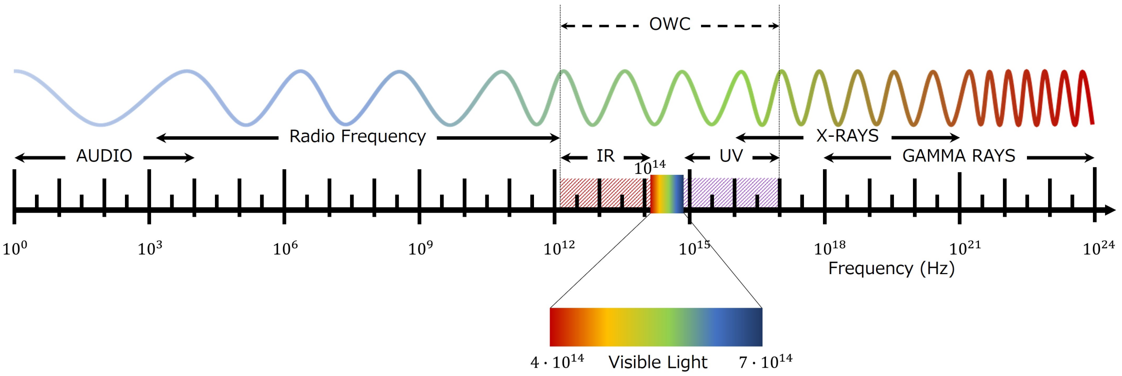

Figure 1.1: Electromagnetic spectrum.

This creates an opportunity for Optical wireless communications (OWCs) to become an interesting alternative and support to communication networks [2]. OWC is even mentioned in the literal 4.3.2 of the "100 Radical Innovation Breakthroughs for the future" by the European Commission [3]. The crowded radio frequency spectrum requires some devices to migrate to another part of the electromagnetic spectrum. OWCs can be used for either indoor or outdoor communication links and can also achieve high data rates (even higher than radio frequency). In addition, OWC has robustness against electromagnetic interference and a high level of protection against intrusion. OWC encloses multiple concepts as VLC, Free-Space optical ommunication (FSO), Optical camera communication (OCC), and Light-fidelity (LiFi) (Fig. 1.2). OWCs refers to any data transmission that is performed by the use of light signals, including infrared, visible, and ultraviolet [4].

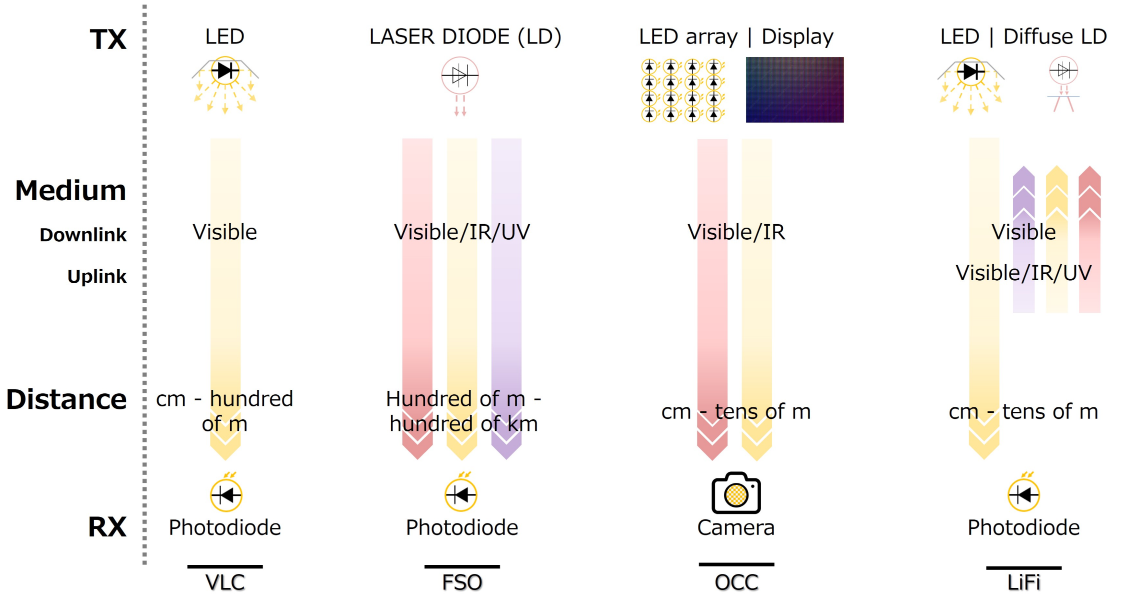

Figure 1.2: Different types of OWC transmissions.

In recent years, VLC has attracted more interest as artificial lighting becomes more efficient since electricity used for lighting accounts for nearly 20% of electricity consumption and 6% of CO_2 emissions worldwide [5]. With the adaptation of high-power white LEDs, the use of light sources beyond mere illumination is becoming a reality, as in the case of this work. VLC refers to any communication that uses the visible light spectrum as a communication channel (Fig. 1.1). VLC commonly uses LEDs as transmitters and Photodetectors (PDs) as receivers.

FSO can be interpreted as a synonym for OWC, but the term has actually been used to refer to large-scale wireless transmissions. In fact, FSO can be considered the wireless equivalent of fiber optic communications, as it defines point-to-point communications over relatively long distances [6]. FSOs are primarily used to enable low-cost wireless backhaul links. Applications under this concept tend to focus on channel modeling and the impact of atmospheric turbulences or geometric misalignments due to the large outdoors link distance between transmitter and receiver.

In the case of OCC systems, the transmitted signal could be generated by any device, e.g., a LED or a display, but, different from other concepts, the receiver is always a camera sensor. The evolution of the CMOS sensors used in current cameras and their close relationship with the smartphone market has stimulated the research in OCC, trying to obtain the maximum of its capacities [7]. OCC cannot reach high speeds or long distances, but it offers practical and fast implementation solutions with very low initial investment in infrastructure.

Finally, the term LiFi was firstly mentioned by the professor Harald Haas on a 2011 TED Talk. LiFi refers to multi-user bidirectional communication with high data rates [4], and usually the optical link uses the infrared or visible spectrum. The increasing need for high data rates for entertainment applications and the rapid development of AR and Virtual reality (VR) impulse the need for high power links that the Radio frequency (RF) spectrum will not be able to handle [6].

1.1. Motivation

VLCs are now at a stage where the theoretical concepts are evolving into actual applications. In the implementation phase, new challenges that could not be seen in the simulation phase have to be overcome. The popularization of VLCs has attracted the interest of several companies and even supports the creation of new companies whose core business is focused only on light communication. An example of this is the LiFi consortium, where big names in the electronics industry, such as Panasonic, General Electric, and Philips have joined forces with leading companies in the field of light communication, such as Oledcomm or PureLiFi (co-founded by professor Harald Hass).

This implies that the market is still evolving in this area, and the companies that can offer innovative solutions will make a name for themselves in this field. In addition, the interest of large companies suggests that this technology will play an essential role in future communications.

On the other hand, VLC takes advantage of the existing lighting infrastructure to create a communication channel without the need for major changes or investment in new equipment. This fast and easy deployment of VLC transmitters is only possible thanks to the evolution of lighting technology. At the end of the past century, the invention of the blue LED allowed the creation of white light with semiconductor devices, which are more efficient than traditional light sources. In addition, semiconductor devices are able to switch very quickly (high data rates), and also, concepts such as those used in fiber optics can be applied to wireless light modulations. Therefore, solutions can be designed to be quickly adapted by users, e.g., a VLC beacon can be included in a lamp that just needs to be plugged in like any other "non-communicating" bulb.

The renovation of the lighting infrastructure is still underway, opening another opportunity to equip the new lighting devices with communication capabilities from the very beginning. Large facilities such as supermarkets or office buildings can benefit greatly from the precise localization that VLC can provide, such as targeting advertisements, special products, office locations, or the availability of a conference

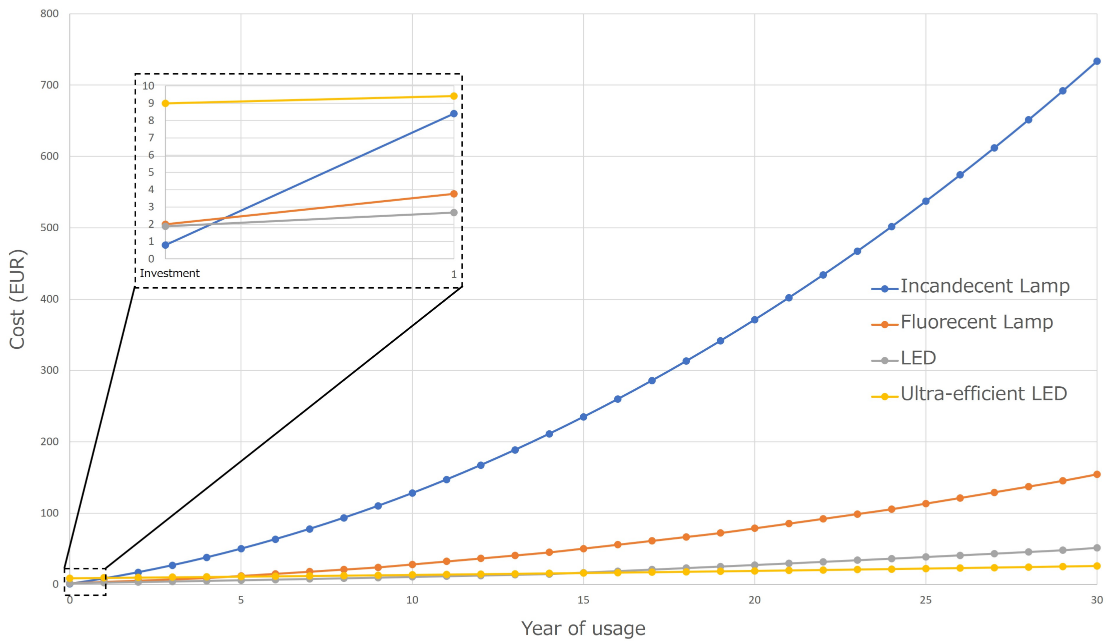

Figure 1.3: Light sources operation cost and maintenance. [1,2]

room. The low implementation cost is also a key factor, as there are a lot of light sources in a single building, and even the maintenance cost over time is significantly less than incandescent and fluorescent lamps, as presented in Fig. 1.3 [1], [2].

The invention of the high efficient blue light was so important that in 2014, Isamu Akasaki, Hiroshi Amano, and Shuji Nakamura received the nobel prize in physics. The most relevant events related to the high efficient white LED are shown in Fig. 1.4.

In addition, as mentioned earlier, the need to move some of the wireless communications out of the radio frequency spectrum due to a large number of newly connected devices motivates us and other researchers to use VLCs as an alternative. VLC provides a harmless communication channel that can be even faster than RF, and the confinement characteristic of visible light allows to have a completely free channel for each lamp, avoiding saturation as the number of connected devices increases. Also, VLC is unregulated [8], allowing the system to use the entire frequency spectrum for data transmission. In addition, VLC does not interfere with current RF communications, and neither RF signals can affect VLC links.

In conclusion, VLC currently offers new opportunities and challenges that, if addressed, will support marketable solutions in multiple areas. Applications in commercial facilities, smart home devices, support for wireless communications, and even a viable communication channel for high wireless data-consuming devices can be handled with visible communications.

[1] The base prices of each light bulb where obtained from www.amazon.es on 07-Jul-2023.
[2] The energy price was the one of jun/23 obtained from www.ree.es on 07-Jul-2023.

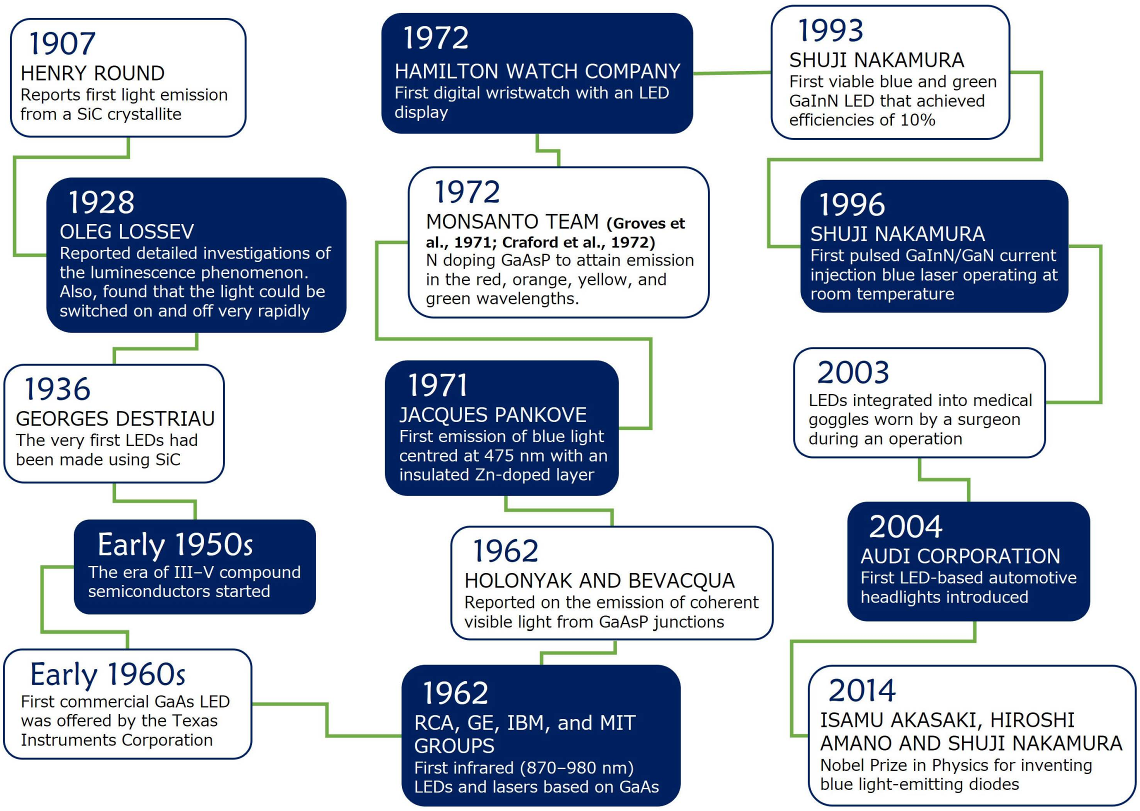

Figure 1.4: LED history timeline.

In this context, this thesis work aims to contribute to the development of new VLC devices and systems that can be used both in info-entertainment applications (such as passenger transportation or shopping malls) and in cultural facilities (as could be museums, tourism centers, among others). It also offers an inclusive platform that will contribute to blurring the division line for access to information for people with disabilities.

1.2. State of the Art

VLC designs can be divided into two major groups. The first group of solutions attempts to reach the limits of VLC, trying to achieve high data rates with very specialized and expensive hardware and very complex modulation protocols. Complex protocols require high computational power and very fast clocks on both the transmitter and receiver sides. These kinds of works give a glimpse of what is possible with current technology, but in most cases, it is not practical or worth the money for a broad and competitive consumer-oriented solution. In this matter, part of the research is focused on developing specialized modules for complex modulation that will reduce the size, complexity, and price of the final device while maintaining the advantages of complex modulation [9].

On the other hand, the second group of solutions optimizes resources to bring an optimal solution for the required application (as it is the target of our work), knowing that each solution has its peculiarities and not always it is required the peak of technology to cover the requirements. Nevertheless, it is important to highlight the requirements and constraints of the target solution, e.g., in IoT, lower throughputs are acceptable because the priority is to have a low-cost, low-energy consumption device.

In the first case, we have very interesting solutions, but due to their high price, they are mainly aimed at the business-to-business (B2B) market. Most of them are part of LiFi solutions offered by leading companies in the sector. An example could be the LiFi-XC™ Evaluation KIT from PureLiFi which offers a downlink of 43 Mbps at a distance of 1m to 6m and a 60-degree Field of View [10]. The system consists of an access point that can be connected to a roof lamp and contains the IR uplink receiver and also has a USB receiver that allows bi-directional communication with the access point. The USB receiver has a small size, which makes it easily accepted by users. As pureLiFi is leading the commercial solutions in this area, they have attracted a lot of investment from a mix of public and private parties. This injection of money allows them to stay on top and create disruptive solutions faster, which is also good for everyone involved in the subject as it creates more interest.

Alternatively, there are solutions that, even when implemented, are tested and designed for controlled environments. Some of these will be reviewed to give us a

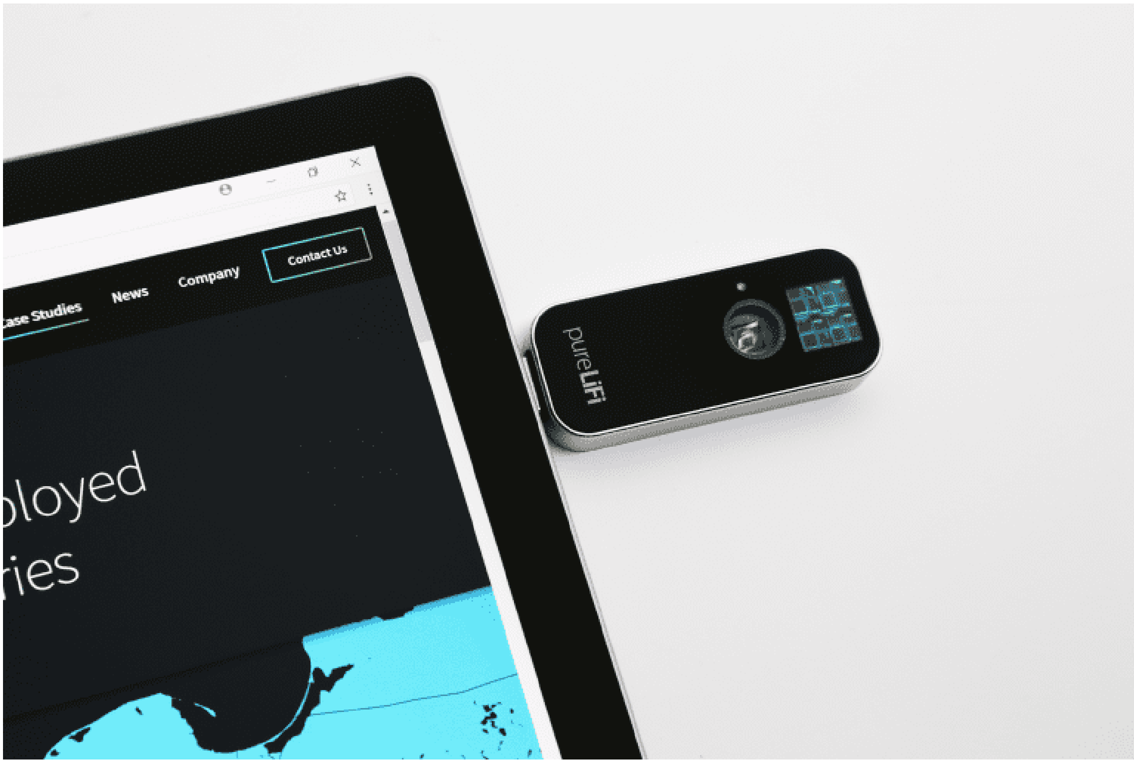

Figure 1.5: USB receiver of the LiFi-XC™ solution offered by PureLiFi. (Image obtained from https://www.purelifi.com/products/lifi-xc/)

better picture of what has been achieved. One of the studies was conducted by Le Minh *et al.*, who achieved data rates of 100 Mb/s using OOK-NRZ modulation (section 3.1). The paper focuses on the equalization of the LED to increase the available bandwidth. Also, since the LED used had a high amount of yellow component (the LED used was the Luxeon LXHL-MW1B), a blue filter was used at the receiver to increase the link bandwidth since the blue component of the LED switches faster than the yellow one. The blue filter had an efficiency of 60%, and with the loss of the yellow power, the link was tested only at a distance of 10 cm between the transmitter and receiver. [11].

On other work performed by Sayco *et al.*, a prototype for VLC communication is designed using a computer to codify and decodify the message. This gaves the prototype a powerfull software configuration but limit it in terms of movement and application enviroments. A relevant found is that as they used a Universal SoftwareRadio Peripheral (USRP), the input and output impadences of the VLC link must be correctly matched to the ones of the USRP. To obtain the maximum signal posible at the receiver a plano-convex lens was used to concentrates the incoming light onto the photodiode active surface. With that configuration they were able to obtain a bit rate of 2.5 Mbps at distances up to 160 cm with a bit error rate (BER) of $9.76637 \cdot 10^{-}5$ [12].

Likewise, Martinek *et al.* perform a study on a real implementation of two different VLC systems. One for indoor applications, which is more appropriate to describe here, and the other focused on outdoor vehicular communications. For the indoor environment, the work evaluates the performance of several Quadrature amplitude modulation (QAM) modulations and the maximum distances that can be achieved with each one. The test system consists of a 44W Philips LED Fortimo DLM 3000/840 Gen3 and a Thorlabs PDA36A-EC photodetector. The software used to generate the transmitted signal and collect the received signal is performed using virtual instrumentation (LabVIEW SDR), which provides a powerful platform but also requires powerful computing equipment. The maximum transmission speed was 20 Mbps, obtained with a bandwidth of 4 MHz and 32-QAM modulation, but at a maximum distance of 90 cm. In contrast, the maximum transmission distance was 325 cm with a transmission speed of 2 Mbps using a bandwidth of 1 MHz and 4-QAM modulation [13].

Torres *et al.* focused on developing a low-cost prototype that supports indoor localization and data transmission in indoor environments and low-power lighting sources. The work prioritized size overall, leaving the maximum transmission speed in a second layer. The channel is coded using Frequency shift keying (FSK), and each packet contains 21 bits divided into 6 bits for synchronization, three and four bits for the lamp and packet ID, respectively, and 8 bits for the message. The receiver used was the BPW21R Si-photodiode and the receiver data was sampled using the internal Analogue-to-digital converter (ADC) of the user's smartphone (connected to the audio jack), and therefore this prototype can only be used with smart devices that have a 3.5 mm audio jack. For the transmission, a commercial desk lamp with an LED is used, which produces an illumination of 88 and 24 lux at a distance of 100 and 200 cm, respectively. The system was tested to work up to 200 cm from the center of the light source at a transmission rate of 441 bps. [14].

An integrated testing VLC platform was presented by Galisteo *et al.*, this platform is called OpenVLC, and it is an open-source project to allow researchers to test different functions on real scenarios quickly. The solution supports TCP/IP communication and software configurable MAC and PHY layers, which provides flexibility to the applications. The design is a custom shield that works with the BeagleBone Black (BBB). The BBB runs Linux operating system and costs about 57 euros. They achieved data transmission up to 100 kb/s was achieved for distances from 20 to 150 cm between the transmitter and receiver. The used LED was a SENCART 2W LED, and the photodiode was an OSRAM SFH-206 [15].

In contrast, the prototype designed and implemented in this thesis will try to keep the receiver cost as low as possible without sacrificing the communication performance of the channel. The available bandwidth on the transmitter side is 15 MHz, almost ten times the bandwidth of the LED thanks to the equalizer circuit. Nevertheless, due to the capabilities of the microcontroller, the transmission is performed with a clock of 250 kHz. This is mainly because we wanted to select a low-cost, small-sized, high-performance microcontroller, and 250 kHz is fast enough for most IoT communication, user localization, and custom information data requirements. On the receiver side, we bring flexibility to the system by supporting a BLE connection with the user's smart device, and the total price of the receiver (including the SoC) was 7.56 € at the prototyping stage. We use an OOK-NRZ modulation format with a transmission speed of 233 kbps over distances from 27.5 to 170 cm using a Fresnel lens on the receiver side.

1.3. Objectives

The main objective of this thesis is to develop all the stages of a VLC system for indoor environments, making it versatile enough to be adaptable to multiple and different solutions while keeping it simple, small, and low-cost. One of the focus applications is developing a system that allows deaf or visually impaired people to access surrounding information. The design must define transmitter control, receiver signal adaptation, channel modulation, and coding. In addition to the hardware, the software responsible for the data transmission, the decoding at the receiver side, and the final visualization for the user must also be designed. With this in mind, the following specific objectives are defined.

First, it is necessary to define the types of transmitters and receivers used in

VLCs in order to select those that better fit the desired solution. Then, the electronics around the transceivers that will allow a light source to also function as a communication transmitter must be evaluated, and then a custom design for the prototype must be made.

In addition, signal conditioning on the receiver side is required to extract the information as reliably as possible while keeping the solution small. The receiver must also be able to communicate with a mobile device.

Furthermore, the most commonly used modulations for this type of channel and their limitations must be reviewed to select the one that will allow data transmission. The packet structure (MAC layer) must also be defined for the system requirements.

At the application level, an application capable of processing the received information must be designed. The application must support the use of AR to provide the user with customized information based on the received optical data.

1.4. Structure of Dissertation

This thesis contains four technical chapters, where contributions have been presented in all of them. Below, a brief description of each chapter is outlined.

Chapter 2 introduces visible light communication, highlighting the two main elements of these communication channels, the LEDs and the PDs. The characteristics of each are discussed, and a novel method of electrically characterizing high-power white LEDs is presented. In addition, the control required to enable the LEDs to operate not only as a light source but also as a communications transceiver is presented. On the other hand, the PDs generates relatively small currents with the incoming light. Therefore, it is necessary to add some signal conditioning elements to produce a signal that can be measured and decoded at the receiver side.

Chapter 3 focuses on the most commonly used modulation formats in OWC. In particular, the two baseband modulations specified in IEEE 802.15.7 are examined. On the other hand, multicarrier modulations are also presented, highlighting the special requirements of OFDM when implemented on VLC channels. A novel time synchronization and phase estimation and correction are also discussed. Finally, a brief overview of the current VLC standards is presented.

Chapter 4 introduces an element used to support OWC, called Intelligent Reflective Surfaces (IRSs). IRSs, are mainly used to allow the connection between two elements where the line-of-sight (LoS) path is blocked. These types of surfaces can be reconfigured to redirect the beam from the transmitter to the receiver. It can also be used to split the beam and also to counteract the effects of geometric misalignments. In particular, a study case is developed and discussed to evaluate the behavior of a IRS based on micromirrors in a free-space optical application.

Chapter 5 presents the design of a VLC system, including all phases and elements: conception, simulation, implementation, and verification. The process outlines the hardware and software development related to the transmitter and receiver. Also, the communication protocol followed in the communication highlights the mechanisms used to ensure a constant level of illumination. The design process should begin with the definition of the hardware and software tools to be used. Then, a system-level design must be defined to outline all the steps. The hardware implementation that will support the software communication requirements is also designed. Finally, the top-level software must be designed to provide the user with the most transparent access to the information being transmitted.

Chapter 6 gathers the main conclusions of the different chapters and presents a series of future lines derived from the results obtained in this work.

2 Visible Light Communication

"Give me six hours to chop down a tree and I will spend the first four sharpening the ax"

Abraham Lincoln

The concept of VLC refers to the use of the part of the electromagnetic spectrum that contains wavelengths visible to the human eye as information carriers. These wavelengths typically range from 390 to 780 nm [16] and can theoretically achieve higher data speeds because the available inherent bandwidth is greater than that of RF. Radio waves, especially those used for Wireless-fidelity (WiFi), have wavelengths from 5 cm to 15 cm. Thus, the wavelength of VLC is about 5,000 times shorter than the shortest wavelength of radio waves.

Although there were some inventions related to VLC in the past, the research in this field of knowledge resumed around the end of the last century. One of the precursors of VLC is the photophone (invention of Graham Bell in 1880), which used sunlight to send messages by changing a transmitting mirror from concave to convex, depending on the voice. The modulated light is then received using a parabolic reflector to concentrate the light in the sensor [17]. An analogy to the photophone can be used in today's designs, where the changing mirror in the transmitter is replaced by a LED that changes the amount of light generated. The parabolic reflector at the receiver is replaced by a lens, and the sensor is now a small photodiode.

But an important question comes to mind when we think about wireless communications. Why do we not continue to use radio waves? Radio waves are well known, and solutions based on them are embedded in our daily lives. In addition, wireless radio communications are regularized and widely used for both military and commercial purposes, with WiFi and Long-term Evolution (LTE) being very popular.

However, as more and more devices are connected wirelessly, the available spectrum is beginning to become crowded, reducing the channel available to each device.

The number of connected devices will exceed 10 billion in 2021, and the projection for 2030 goes to nearly 30 billion connected devices, three times more connected devices in ten years [18].

Therefore, solutions that can support the reduction of radio channel usage have been gaining interest in recent years. Here VLC plays a key role, especially for indoor purposes, but with high potential for all kinds of applications.

The evolution of lighting devices from incandescent bulbs to LEDs also stimulates the research on VLCs. This is because the ability to produce white light using LEDs has driven the lighting market to adopt this new technology, which has increased not only the electro-optical efficiency but also the lifetime of the bulbs. In addition, LEDs are semiconductor devices, making them more suitable and faster than incandescent bulbs for communication purposes. Today, many devices use LEDs as a light source. TV screens, smartphones, and automobiles, among others, are equipped with LEDs. Moreover, the technology popularization helps to lower the LEDs prices. Other advantages that the LEDs bring with them are:

- Its easier fabrication process and ability to build more than one LED in the same board, e.g., Chip On Board (CoB) LEDs.
- Reliability, because degradation is slower, and commutation does not necessarily reduce device life.
- A simplified driver circuit and linear relationship between input power and emitted light (at least inside bandwidth limits and small signal conditions).

In VLC, two different propagation modes are possible, one being the LoS and the other the non-LoS, due to reflections [19]. The non-LoS can only exist in confined enviroments, where the surfaces surounding the light sources are close enough to receive the emitted light and reflect it in other directions. The reflections create a multipath channel that can be negligible for certain conditions, as low speed transmission, a square-law detection on the detector, or a low-power transmitter.

LoS links have very little path loss, there is often no multipath dispersion, and they can reduce the effects of ambient light. But they require a good alignment between Transmitter (TX) and Receiver (RX), and therefore the communication can only be maintained if the LoS is not blocked. The LoS link can also be directed and undirected, which depends primarily on the emitting angle of the transmitter. On the other hand, the non-LoS path can be used as the primary communication link if there are obstacles in the way between the TX and RX. The non-LoS link provides robustness to the system, but, on the other hand, a lot of power is lost in the channel, which means that more power must be injected into the transmitter to have a Signal-to-noise ratio (SNR) good enough to ensure communication. External elements such as reflective surfaces or the size of the room also affect this type of communication.

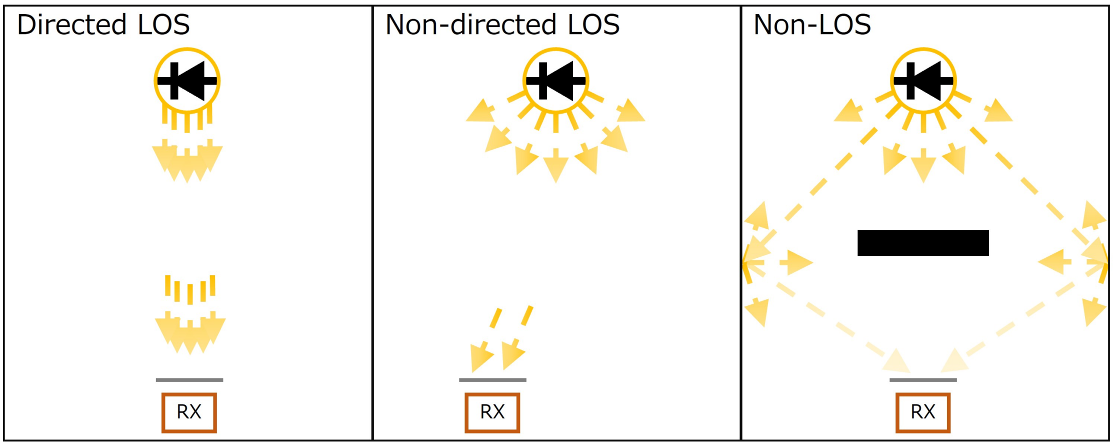

Figure 2.1: Propagation modes for an indoor VLC channel.

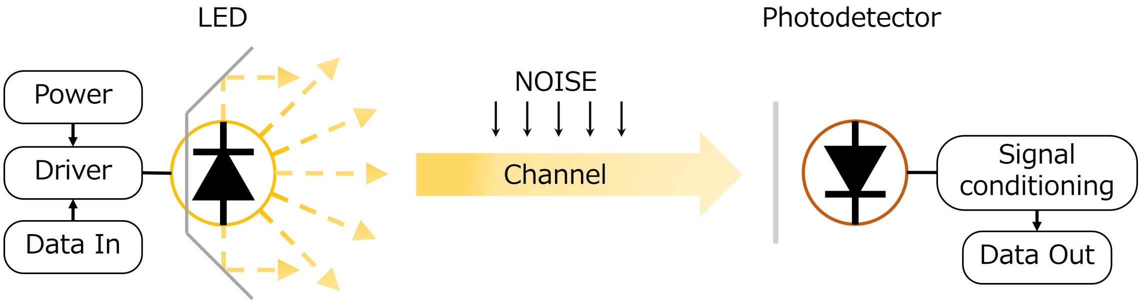

Figure 2.2: Conceptual overview of a VLC system.

In the following sections, we will take a closer look at the main components of a light communication system, such as the one shown in Figure 2.2.

2.1. Optical Sources and Detectors

The main elements responsible for converting electrical information into visible light and vice versa will be discussed first. Without them, the capabilities of VLC systems, such as speed, cost, or low impact deployment, are limited. Both LEDs and PDs are semiconductor devices that use the P-N junction to emit/absorb energy. The bias direction of the external field affects the P-N diode's conduction.

2.1.1. Basic Properties of an LED

In a forward-biased p-n junction, the recombination of holes and electrons takes place inside the structure, especially near the junction. The energy of the unbound free electrons must be transferred to another state for this recombination to occur. Some of this energy is lost as heat, and some as light (photons) [20]. Each semiconductor has its unique band gap, which is directly related to the wavelength and frequency of the emitted light [21]. Therefore, depending on the semiconductor material, a p-n junction can generate more heat or more light and can also affect the wavelength of the generated light (color). Table 2.1 lists some examples of common semiconductor compounds used to make LEDs and the light they produce [22].

Table 2.1: Different LED fabrication semiconductor materials.

Semiconductor	Color	Wavelength
GaAs, AlGaAs	Infrared	$\lambda > 760$
AlGaAs, GaAsP, AlGaInP, GaP	Red	$610 < \lambda < 760$
GaAsP, AlGaInP, GaP	Orange	$590 < \lambda < 610$
GaAsP, AlGaInP, GaP	Yellow	$570 < \lambda < 590$
InGaN/GaN, GaP, AlGaP	Green	$500 < \lambda < 570$
InGaN/GaN	Blue	$450 < \lambda < 500$
InGaN	Violet	$400 < \lambda < 450$
AlGaN, AlGaInN	Ultraviolet	$\lambda < 400$

An ideal LED should convert each electron that jumps the gap into a photon. The ratio of the number of electrons injected into the LED to the number of photons emitted from an active area per second is known as the internal quantum efficiency of the LED [23]. In reality, this 100% recombination never happens, and even if it did, some of the photons would be trapped in the device, but researchers are constantly looking to make LEDs devices more efficient, as many major industries have direct involvement in LED technology. An increase in efficiency or energy consumption, even a small one, will carry billionaire gains in industries like mobiles.

To expres it numerically, the internal quantum efficiency can be described by the ratio of the generated photon flux to the injected electron flux (electrons per second) [24]:

$$\Phi = \eta_i \frac{I}{q} \tag{2.1}$$

Where I is the injected current; and q is the elementary charge ($q = 1.602176 \cdot 10^{-19}\ C$).

However, as mentioned earlier, not all of the photons generated are effectively emitted from the device. Therefore, the radiant flux of the device depends not only on the internal quantum efficiency but also on the extraction efficiency (η_e). Taking this into account and using the Planck relation [25], the optical output power expressed as a function of current is given by [26]:

$$P_o = E\eta_e\Phi = h\nu\eta_e\Phi = h\nu\eta_i\eta_e\frac{I}{q} \tag{2.2}$$

Where h is the Planck constant ($6.626 \cdot 10^{-34}\ \ Js$) and ν is the frequency of the photon. Although the output optical power is directly related to the current injected into the LED, the efficiency of the transmitter increases more slowly at

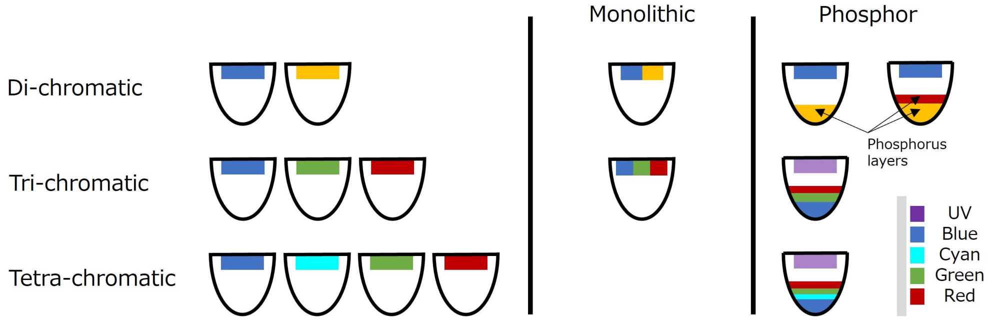

Figure 2.3: LED based approaches for white light.

higher currents. This can be explained by the fact that, at high currents, the device has an overflow of carriers which can be lost as heat. Therefore, as a result of this behavior, there is an optimum current level at which the optical power/injected current is maximum.

As one of the advantages of VLC is the use of the transmitter for communication and illumination purposes, the type of LEDs that better suits these kinds of solutions is the white LEDs. As shown in table 2.1, none of the semiconductors used for LEDs can create a broad spectrum emission (white light). Nevertheless, researchers have found two solutions to this challenge.

First, white light is a combination of colors, and therefore it can be obtained by using different LEDs in one package [27]. The RGB LEDs can produce white light among other colors by combining the three primary colors of light, which are red, blue, and green. This capacity of the RGB to create multiple colors is also a drawback in terms of the Color Rendering Index (CRI) of the generated white light, as a little shift in the current of any of the LEDs will cause a color change. The other approach is to use the photons generated by the LED to excite a phosphor layer. The phosphor reacts to the photons with a given wavelength and re-emits them in another wavelength. The most used combination in the illumination market is the one obtained by using a blue LED and a phosphorus layer that emits in yellow. Also, phosphors are very stable and are capable of quantum efficiencies close to 100 %, which explains why this method is widely used [16]. There are other multiple forms to obtain white light using LEDs, although they are not used as much as the two previously described, some of them are depicted in Fig 2.3.

Another reason why the RGB LEDs are not as widely used as a lighting source is that the complexity and cost are higher than the phosphor-based white LEDs. The spectrum of the three most popular approaches to generating white light is shown in Fig. 2.4 [28].

Another relevant optical characteristic of the LEDs is the directionality. Directionality refers to the angle of emission of the photons exiting the LEDs. A lower directionality is bad for illumination purposes, as the illuminated area is smaller,

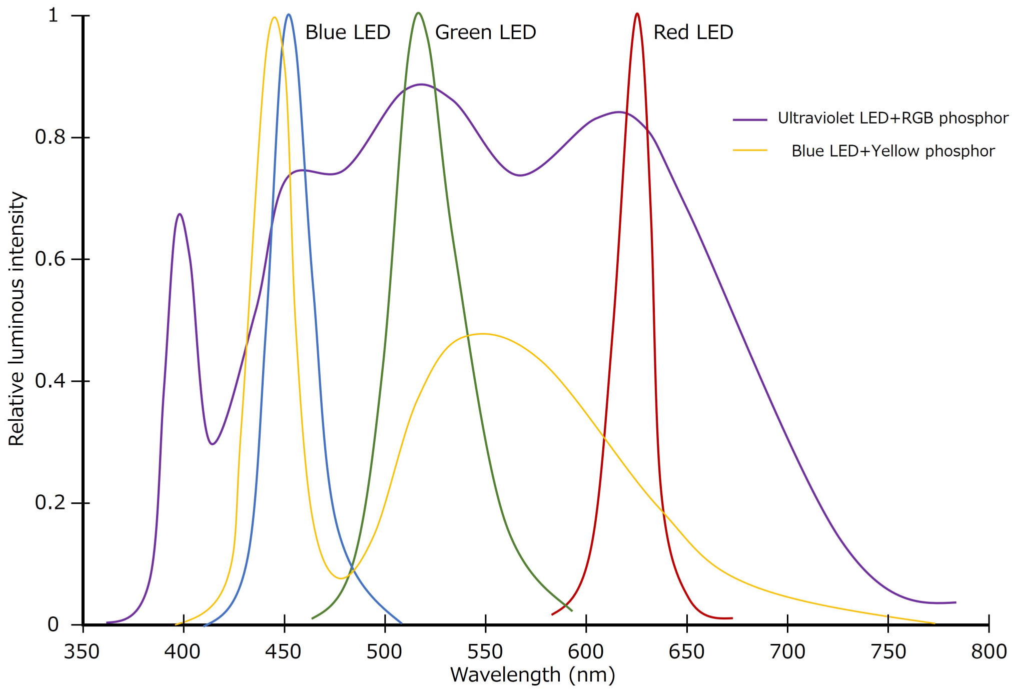

Figure 2.4: Spectral power distribution for the more common white LEDs.

but it is good for data transmission as more power is concentrated in the same area (meaning more distance or better SNR) [29]. A generalized Lambertian radiation pattern is often used to represent the radiation characteristics of a single LED. Where the radiant intensity of a Lambertian pattern at any angle θ is given by $I(\theta) = I_0 cos(\theta)$. The way to measure the directionality of a light source is the half-power angle. A common way to represent the emission angles of a light source is the radiation pattern. The radiation pattern describes the relative light intensity in each direction from the light source [30]. An example of this diagram is shown in Fig. 2.5.

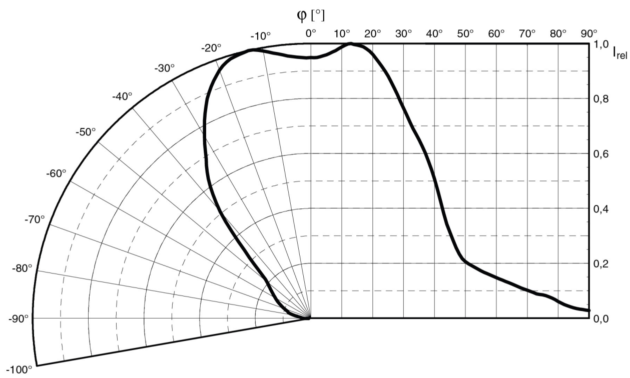

Figure 2.5: Lambertian radiation pattern.

2.1.1.1. LED equivalent circuit model

Because LEDs are just another type of diode, their current-voltage characteristics are very similar to those of a conventional p-n diode. The current-voltage characteristic of the diode is then modeled as a nonlinear resistor, following [31]:

$$I_d = I_o \left(e^{\frac{qV_d}{\eta kT}} - 1 \right) \tag{2.3}$$

where K is the Boltzmann constant, T is the junction temperature (in Kelvin degrees), V_d is the junction voltage, I_o represents the device leakage current, and the factor η is a nonideality fitting parameter.

The equivalent LED circuit includes two behaviors that can be modeled as capacitances, known as diffusion and barrier (or depletion) capacitance, which are nonlinear electronic elements. One is related to the electronic charge of the atomic ions, and the other is related to excess minority-charged carriers injected under direct polarization conditions [32]. Thus, the AC equivalent circuit of an LED is shown in Fig. 2.6. Along with the capacitances, the LED model also takes into account two resistances, a parallel resistance r_p, and a parasitic resistance inside the LED R_s [33].

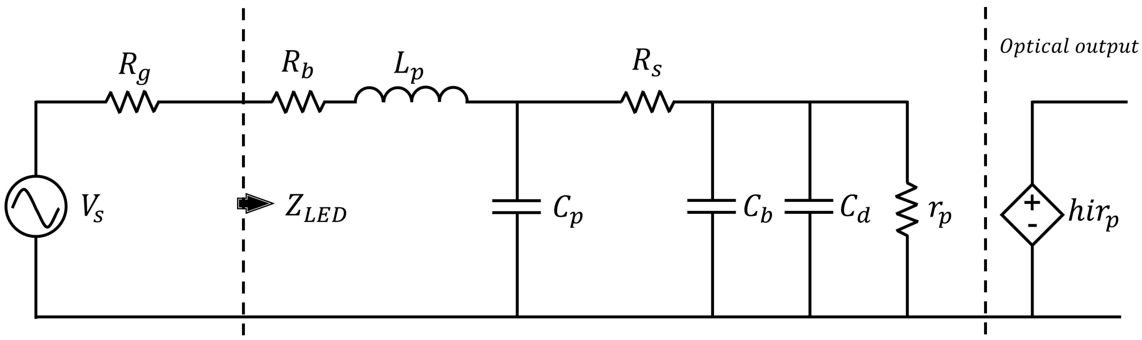

Figure 2.6: Equivalent circuit to model the LED.

The equivalent circuit allows us to understand the behavior of the LED, and it is therefore relevant for better design and more efficient drivers, modulation circuits, and equalizers. There are some obstacles to obtaining the values of the elements of the equivalent circuit. Even so, a novel method has been proposed to obtain the different elements of the equivalent circuit, which will be explained in section 2.2.

When the LED is also used as a transmitter, its bandwidth becomes an important parameter. The electrical bandwidth of the LED, which can be defined by the equivalent circuit, can be different from the bandwidth of the emitted optical signal. In particular, for phosphor-based white LEDs, several works have found that the phosphor layer has a slow time response, and therefore the yellow component is the one that limits the transmission bandwidth to a few MHz [34–36].

In addition, LED can be modulated in on-off or linear modes. First, when the device is turned on and off, the bandwidth is dominated by the internal capacitance of the device. The charge/discharge dynamics of these elements are slow, and also the signal is distorted by the non-linear behavior of the LED. In return, the transmitted signal is larger. On the other hand, driving the LED in the linear region (keeping it on) increases the bandwidth of the device, and the signal will not suffer distortion in the transmission.

2.1.2. Basic Properties of a Photodetector

As in an LED, the electron-hole recombination was responsible for the emission of photons of a certain wavelength, the opposite process is also possible. This means that if a P-N junction is irradiated with photons, some of them will give enough energy to the electrons to be released. This effect is known as photon absorption [37]. The photocurrent of the photodiode is described as:

$$I_{ph} = q\left(\frac{\eta P_{opt}}{h\nu}\right) \tag{2.4}$$

The total number of photons arriving at the surface per unit time is $(P_{opt}/h\nu)$, where P_{opt} is the incident optical power, $h\nu$ is the photon energy, and η is the quantum efficiency. This final parameter is very dependent on the semiconductor material and wavelength. The quantum efficiency can be defined as the number of electron-holes generated per photon:

$$\eta = \left(\frac{I_{ph}}{q}\right)\left(\frac{P_{opt}}{h\nu}\right)^{-1} = (1-r)\left(1-e^{\alpha(\lambda)d}\right) \tag{2.5}$$

Where r is the Fresnel reflection coefficient of the semiconductor-air interface, d is the width of the absorption region, and α is the absorption coefficient. The range of wavelengths at which substantial photocurrent can be generated is limited because α is a highly wavelength-dependent function.

As it happened with LEDs, the wavelength sensitivity and the absorption coefficient depend on the semiconductor material used in the photodetector. A good measure to compare the performance of the device is the spectral responsivity. The responsivity can be defined as the ratio of the generated photocurrent (I_p) to the incident optical power (P_{opt}) and can be defined by using (2.4):

$$\mathcal{R} = \frac{I_{ph}}{P_{opt}} = \eta\frac{q}{h\nu} = \eta\frac{q\lambda}{hc} \tag{2.6}$$

The relationship between the responsivity and the wavelength of some of the semiconductors used in PD is shown in Fig. 2.7.

On the other hand, the photosensitive area must be as uniform as possible, which means that the conversion of incident light into current must be the same at every point in this area (2.6), i.e., $p \in \mathcal{A} \Rightarrow \Delta\mathcal{R}_p = \mathcal{R}$. Although this is never true in actual devices, for most Si-based photodiodes, the responsivity on the 80% of the sensitive area has a variation of only 2% [38], an example of a typical responsivity uniformity curve is shown in Fig. 2.8.

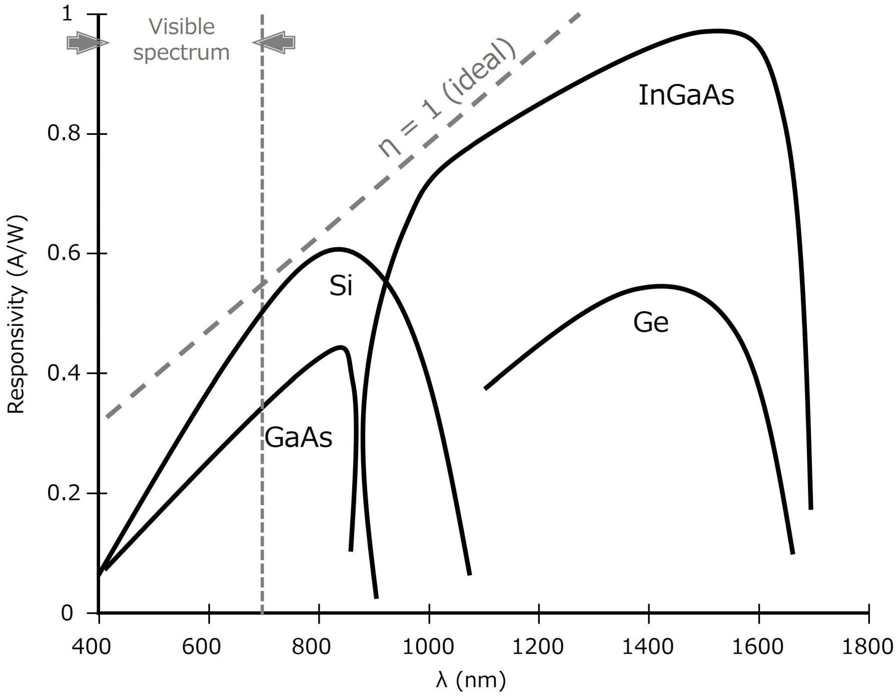

Figure 2.7: Spectral responsivity.

Another similarity with the LEDs is that the Field of view (FOV) of the PD is represented by a Lambertian pattern (Fig. 2.5). The FOV of the PD is defined where the directivity is reduced to half. As expected, the FOV can be reduced or increased by additional optical elements, such as lenses.

Since the photodiode is desired to collect as much of the transmitted signal as possible, it is natural to focus on a large area PD. However, the larger the PD, the larger its internal capacitance, and therefore it will have a slower response, which affects its bandwidth. This internal capacitance is due to the depletion zone formed between the semiconductors, which acts as a dielectric component between two charged elements, as in a capacitor. An alternative to increase the detection area while maintaining the bandwidth can be an array of PDs. This solution could also help to increase the receiver FOV by placing the PDs on a non-planar surface. For small photodiodes have been reported bandwidths of tens of MHz, even reaching hundred of MHz [39].

The PDs have a wide range where the transfer between input optical power and output current is linear. However, clipping can also occur in the receiver when a high amount of light drives it into saturation. This could be a problem in outdoor applications where the solar radiation can inside directly the PD, but for indoor applications, the transmitted signal must be in the range of the limits imposed by the eye safety regulations, and with the inherent path attenuation it is highly unlikely to drive the PD into saturation.

The photodiode can be operated in two different modes, the photoconductive

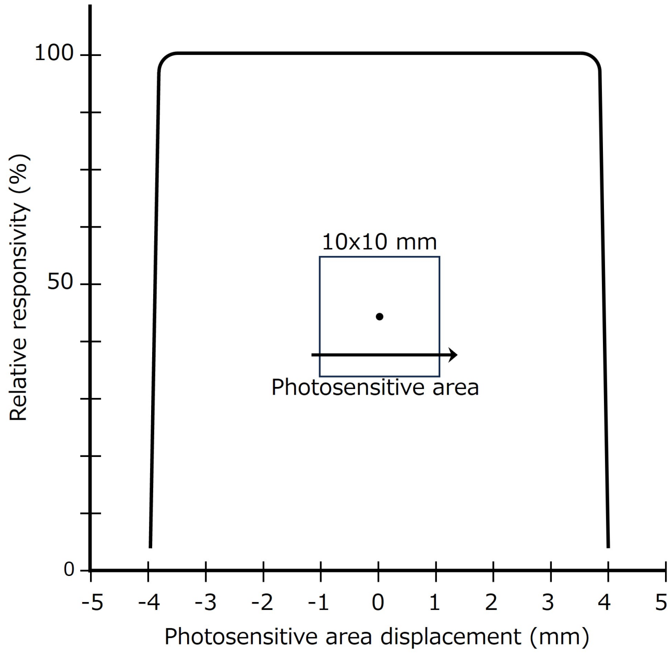

Figure 2.8: Typical Si photodiode responsivity uniformity.

mode, and the photovoltaic mode. In the photoconductive mode, the PD is biased with a reverse voltage, causing the depletion region to be wider. This widening of the depletion region has several advantages. First, a wider depletion region makes the photodiode more sensitive. Second, as the depletion capacitance can be defined by the change in electric charge per change in voltage [40, 41]:

$$C = \frac{dQ}{dV} \tag{2.7}$$

The junction capacitance, which is directly related to the depletion layer width, will be smaller. In addition, the junction capacitance can also be described by the dimensional characteristics of the diode as follows:

$$C = \epsilon_r \epsilon_0 \frac{A}{d} \tag{2.8}$$

Where ϵ_r is the permittivity of the semiconductor, ϵ_0 is the vacuum permittivity, A is the area of the p-type and n-type regions, and d is the width of the depletion region. Third, it also increases the range of linear operation. The negative effect is that the dark current of the PD increases with reverse polarization. On the other hand, in photovoltaic mode the device output is a non-linear logarithmic relation between the incident radiation and the device voltage. This mode is mostly used in energy-harvesting applications [26].

2.1.2.1. Types of photodiodes

There are several types of photodiodes. Some of them include the P-N photodiode, the P-i-N photodiode, the metal-semiconductor photodiode, and the Avalanche photodiode (APD), among others. However, both the P-i-N photodiode and the APD, which are the most widely used in optical communications, will be discussed further. Although both are available in Si technology, P-i-N photodiodes are simpler and cheaper, while APD photodiodes can provide higher sensitivity at the expense of higher voltage requirements and cost [42]. A cross-sectional comparison of the two is shown in Fig. 2.9.

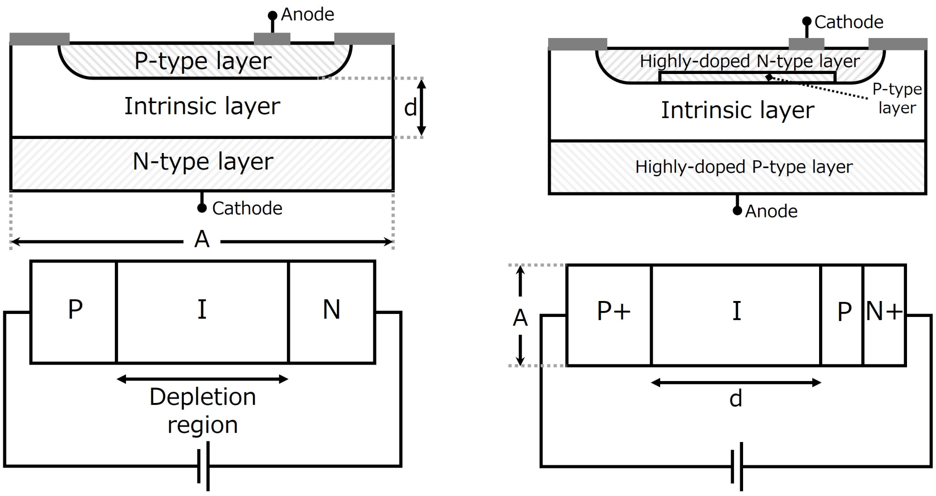

(a) P-i-N

(b) Avalanche

Figure 2.9: P-i-N and APD Photodiode cross-sections.

P-i-N (P-type, intrinsic, N-type) photodiodes were developed as a solution for two of the major drawbacks of the P-N photodiode. First, as mentioned earlier, the smallest the depletion zone, the bigger the junction capacitance, which makes P-N PDs unable to operate at high frequencies. Second, and also due to the small depletion zone, the area where the photons can effectively generate an electron-hole pair is reduced, making them to be absorbed outside the depletion region.

An Avalanche photodiode (APD), on the other hand, take advantage of the avalanche effect to improve performance, one photon can now generate more than one electron-hole. Free carriers passing through a strong field zone gather enough energy to create other free carriers. This effect can only be achieved at high reverse voltages to generate a strong enough electric field. This advantage is also a drawback, the avalanche multiplication process is random, so not every electron-hole pair created at a certain distance in the depletion region experiences the same multiplication, resulting in the so-called avalanche noise.

The various noise sources that can be found in the detector are of particular importance when it comes to preserving the integrity of the information. Since the received power is low due to the free space channel, the generated current can be of the same order as some of the noise, making it impossible to recover the information. In addition to the avalanche noise (when this is the case), the other noise sources are quantum noise, background noise, dark current, and thermal noise.

2.1.2.2. Si photodiode equivalent circuit model

When it comes to the equivalent model of a Si photodiode (in reverse biasing conditions), it can be defined as a current source, dependent on the incident light (I_{ph}), with a parallel capacitor, which is no other than the junction capacitance (C_j). The capacitance equation (2.8) can be reformulated in terms of the applied reverse voltage as:

$$C_j = \frac{\epsilon_r \epsilon_0 A}{\sqrt{2\mu\rho\left(V_r + V_{bi}\right)}} \tag{2.9}$$

Where $\mu = 1400\ cm^2/Vs$ is the mobility of the electrons at 300 K, ρ is the resistivity of the silicon, V_{bi} is the built-in voltage of silicon, and V_r is the reverse bias voltage. Furthermore, two resistances must be added to the equivalent circuit, one due to the contacts of the Si device to the exterior (R_s), and the other that represents the slope of the current-voltage curve at the origin (R_{sh}) as shown in Fig. 2.10 [43–45].

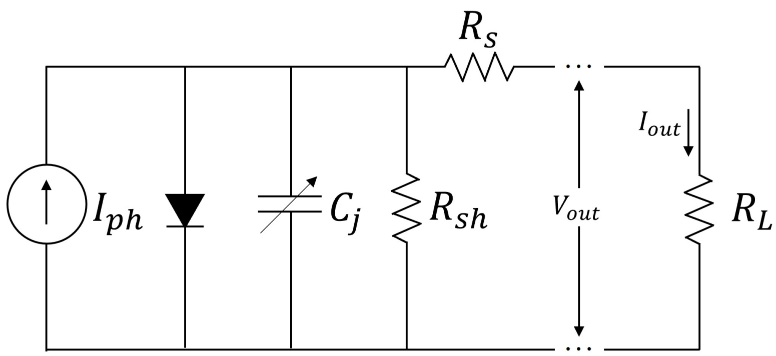

Figure 2.10: Equivalent circuit to model the PD.

As can be seen in Fig. 2.10, the output current (I_{out}) is then the addition of three different currents. One is the current generated by the incident light (I_{ph}), the other two are leak currents that flow through the ideal diode (I_D), and the one flowing through the R_{sh} resistor (I_{Rsh}). Since the diode current can be rewritten in terms of the reverse saturation current according to 2.3, the output current follows [46]:

$$I_{out} = I_{ph} - I_o\left(e^{\frac{qV_D}{\eta kT}} - 1\right) - I_{Rsh} \tag{2.10}$$

V_{out} in an open circuit (no load) can then be easily obtained from the current equation by setting I_{out} to zero. Since V_{out} is then equal to V_D without load, it can be defined as:

$$V_{out} = \frac{\eta kT}{q} \cdot ln\left(\frac{I_{ph} - I_{Rsh}}{I_o} + 1\right) \tag{2.11}$$

However, in an ideal PD, the parallel resistance, also known as the shunt resistance (R_{sh}), is infinite, and the series resistance is zero, so its effect on the previous equations can be neglected in most cases. Therefore, the leakage current depends on the reverse saturation current of the ideal diode and the device temperature. Also, the ideal diode behaves more like an open circuit as the reverse voltage is increased.

2.2. Electrical characterization of LEDs

To understand the dynamic response of lighting LEDs, it is essential to know the equivalent circuit that models its behavior. Although there have been studies to derive the equivalent circuit of the LEDs, e.g., in [47], the results obtained are limited to a currents below 36 mA, which hinders its implementation for high-power LEDs.

For this reason, we have proposed in [48] a novel measurement methodology to determine the electrical equivalent circuit of LED emitters at medium/high frequencies. The electronic equivalent circuit represents the physical behavior of the LEDs. This allows the dynamic response of the LEDs to be defined by the combination of passive electronic elements.

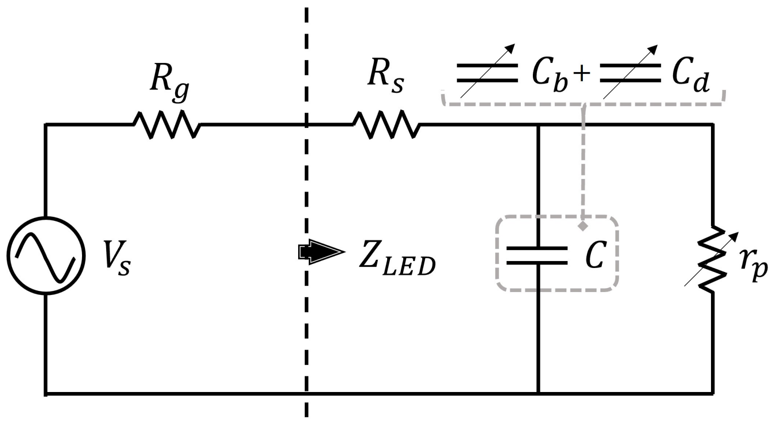

Figure 2.11: Simplified equivalent circuit to model the LED.

The simplified equivalent LED circuit is based on the one shown in Fig. 2.6, ignoring the parasitic components (R_s, R_p, and C). Since the two capacitances are in parallel and cannot be measured independently, they are combined into an equivalent capacitance, hereafter called the joint capacitance. The simplified equivalent circuit is shown in Fig. 2.11. Note that the response of the LED in time and frequency is determined by the joint capacitance, i.e., the sum of the barrier and diffusion capacitance.

By using a previously calibrated lock-in amplifier, we obtained the impedance of the LED by performing a current shift. Since the value is inversely proportional to the polarizing current, the impedance tends to become constant as more current is applied to the LED. This "constant" value corresponds to R_s. Also, the value of R_p can be defined as $\frac{\eta KT}{q}$, where K is the Boltzmann constant, η is an experimental coefficient that depends on the LED, T is the junction temperature (in Kelvin degrees), and q is the electron charge.

The equation that models the resulting capacitance value is the following:

$$C = \frac{\sqrt{R_p^2 - |Z(\omega)|^2}}{R_p \cdot \omega \cdot |Z(\omega)|} \tag{2.12}$$

where $|Z(\omega)|$ is the value of the measured impedance obtained through the lock-in amplifier at frequency ω. Then, to obtain the modulus of the impedance the LED is polarized with a small current. This is because the capacitance value varies with the current, but as the current used is below the threshold, the measured capacitance value is assumed constant.

2.3. Driving

When it comes to driving the LED, the device needs not only the switched signal but also a stable operating point (DC bias). These two elements seek different advantages. The trade-off for high-speed applications is a lower signal excursion, and on the other hand, when a large current needs to be driven, the bandwidth of the system is reduced. Thus, the driver must be carefully selected depending on the application.

On the other hand, the received signal typically generates currents of less than tens of uA. Therefore, circuits that can amplify the signal while inducing minimal noise to recover the transmitted information are essential.

2.3.1. LED drivers

LEDs always need a polarization point that determines the level of illumination. The information voltage signal must be converted into a modulation current, since LEDs usually have a linear relationship between current and optical power, which makes the communication process much easier. This information can be transmitted in two ways. First, the LEDs can be commutated ON and OFF to generate two values (light and its absence). Second, the modulated signal can have a small amplitude and can be transmitted continuously over the linear range of the LED (keeping it always ON).

2.3.1.1. Switching drivers

These drivers have the advantage of simplicity in implementation, but the trade-off is that the modulation can only be done in pulse-based modulation schemes (as could be On-Off keying (OOK), Pulse position modulation (PPM) or Variable pulse position modulation (VPPM)) [49]. The information (bits) can be injected directly into the controller without the need for a Digital-to-analogue converter (DAC).

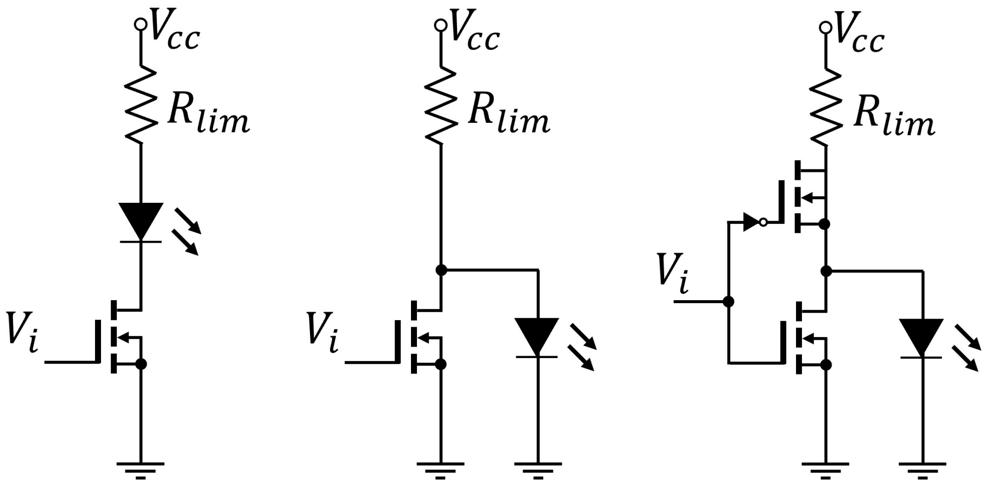

(a) Non-inverter (b) Inverter (c) Inverter with discharge

Figure 2.12: MOSFET as a switch to control the on-off states of an LED.

The control signals usually have a low current, requiring active elements to drive the LED current. Transistors, when the circuit is properly designed, can act as switches in control applications. When it comes to driving LEDs, both Bipolar junction transistors (BJTs) and Metal-oxide-semiconductor field-effect transistors (MOSFETs) have their unique advantages and disadvantages. BJTs are less expensive and easier to drive but have limited switching speed and can be prone to thermal runaway [50]. MOSFETs, on the other hand, have a higher switching speed and tend to be more efficient due to their lower power dissipation, but are generally more expensive and more complex to drive [51]. In terms of size, MOSFETs tend to be smaller than BJTs, making them more suitable for applications where space limiting is an issue.

The simplest circuit is to use the transistor in series with the LED as depicted in Fig. 2.12. A resistor is added to the loop to control the current that will flow through the LED, and then the illumination level will depend on the resistance value (and in the selected modulation). The control voltage must be large enough to drive the MOSFET into saturation region. A problem arises when the transistor is turned off, because the internal capacitance of the LED and the large resistance present in the transistor create a slow discharge dynamic ($\tau = 1/RC$). To overcome this, a discharge transistor can be added in parallel to the LED, allowing the circuit to reach higher switching frequencies [52]. When the LED is off in the non-inverter configuration, all of the supply voltage (V_{cc}) is between the transistor terminals (V_{gs}). Therefore, the transistor must be selected to have a breakdown voltage higher than the supply voltage.

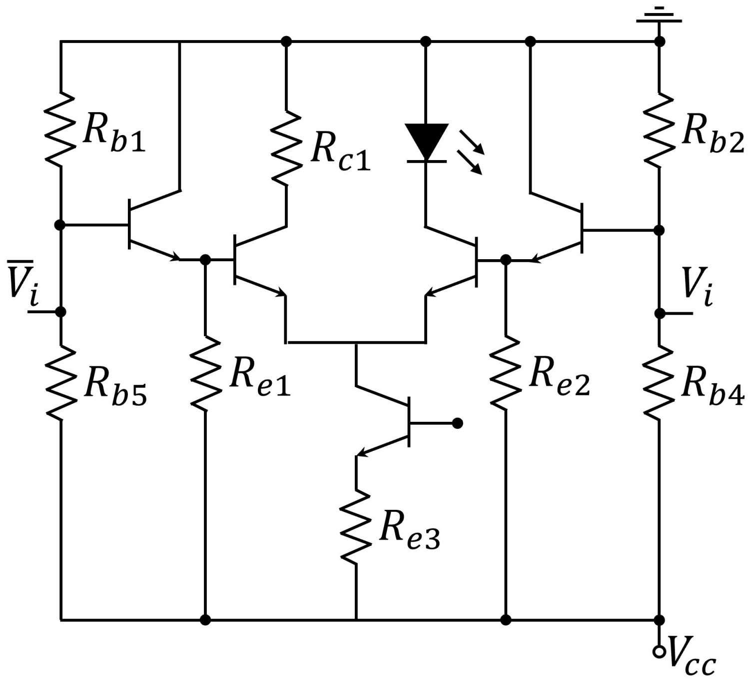

Figure 2.13: Emitter coupled drive circuit.

The inverting behavior (LED on when transistor off) can be achieved by using the MOSFET in parallel with the LED. To improve the dynamic behavior of this configuration, as in the non-inverter, a transistor can be added to discharge the internal capacitance of the LED when it is off. The circuits shown in Fig. 2.12 are also compatible with BJTs technology, but a resistor on the base must be added to convert the input voltage into a current.

Another relevant drive circuit is the emitter-coupled circuit shown in Fig. 2.13. The LED serves as a load in a collector, generating a drive current for the device. Although the circuit has the appearance of a linear differential amplifier, it operates in switching mode. The lack of saturation in this circuit allows to obtain a high switching bandwidth and also reduces the base drive requirements for the transistors. This is because the circuit prevents the degradation of the turn-off time caused by the accumulation of stored charge in the base region of the transistor [53]. The circuit is also very stable over a wide temperature range.

2.3.1.2. Analog drivers

Analog drivers, contrary to the previous ones, must have high linearity, and the controlled current must follow the input signal not only in amplitude but in phase. The input signal is assumed to be time continuous. To ensure linearity, the LED polarization point must be in the linear region, and the input signal must not exceed the linear range of it. Therefore, the driver must be adjusted to the particularities of the chosen LED to ensure low distortion [54].

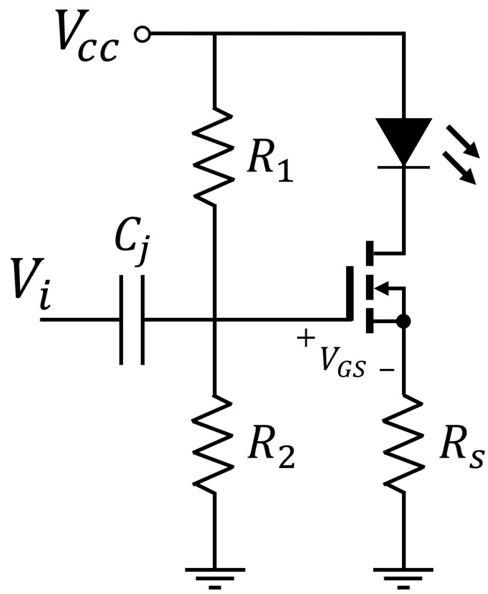

Figure 2.14: Voltage-divider bias arrangement driver circuit.

One possible driver could be a voltage divider bias configuration where the LED replaces the collector resistor (Fig. 2.14). In this configuration, the bias current (therefore the LED operating point) is independent of the transistor's internal transimpedance gain. This is important because the polarization point must be maintained to avoid signal clipping and cannot rely on such a volatile parameter that can change from transistor to transistor and is highly temperature dependent. This configuration can be used with both BJT and MOSFET. The quiescent collector current is approximately half the peak value, and thus, the circuit is biased in a Class A mode of operation.

When analyzing it in DC, as $I_G = 0$, the gate voltage V_G is equal to the voltage in R_2 and can be obtained by a voltage divider of the resistors R_1 and R_2. Then, to obtain V_{GS} just need the voltage in the source resistor, which following ohm's law is $I_S R_S \approx I_D R_S$.

$$V_{GS} = \left(\frac{V_{cc} R_2}{R_1 + R_2} \right) - I_D R_S \tag{2.13}$$

Since V_G is fixed by the voltage divider, different values of R_S will change the point where the curves intersect (working point) as shown in Fig. 2.15 [20]. This factor is very interesting for the LED control because its illumination depends on R_S. The higher R_S, the lower the current through the LED. It can also be seen in the figure that large temperature changes will cause small variations in the operating point.

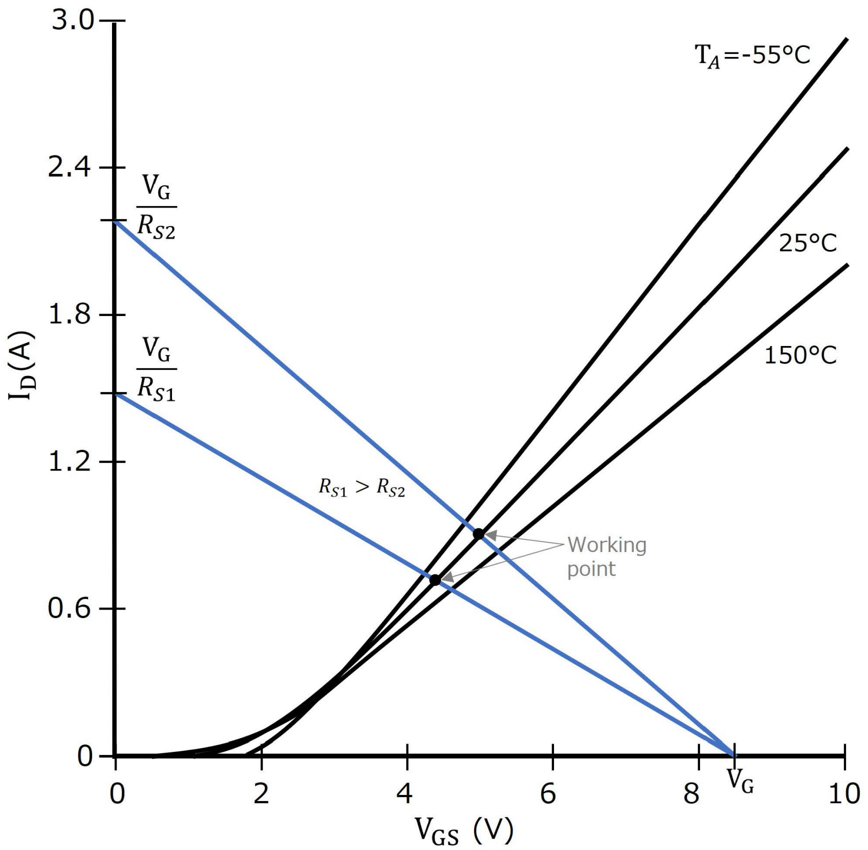

Figure 2.15: Effect of R_S on the transistor working point.

In terms of power dissipation, other multiple parameters are relevant. For the case of the transistor, V_{DS} must be lower than the maximum drain-to-source breakdown voltage. V_{DS} can be defined as follows:

$$V_{DS} = V_{cc} - I_D R_S - V_{diode} \tag{2.14}$$

But even if V_{DS} is less than the breakdown voltage, the transistor has a maximum power dissipation equal to $V_{DS} I_D$. As the transistor gets larger, these parameters increase, giving more room for power dissipation but also increasing the internal capacitance, making the device slower. On the other hand, a lot of power is also dissipated at R_S, so the maximum power dissipation of R_S must be chosen carefully.

Another driver can be a differential amplifier with a constant-current source circuit [53] as the one shown in Fig. 2.16. The LED is connected to one of the nodes of the differential amplifier, modulating it directly. The transistor Q_3 works as a current source that can be approximated to an ideal constant current source in parallel with a high impedance resistor, which improves the function of the circuit while limiting the maximum LED current [20]. The voltage applied to Q_2 (V_{ref}) sets the operating point of the LED.

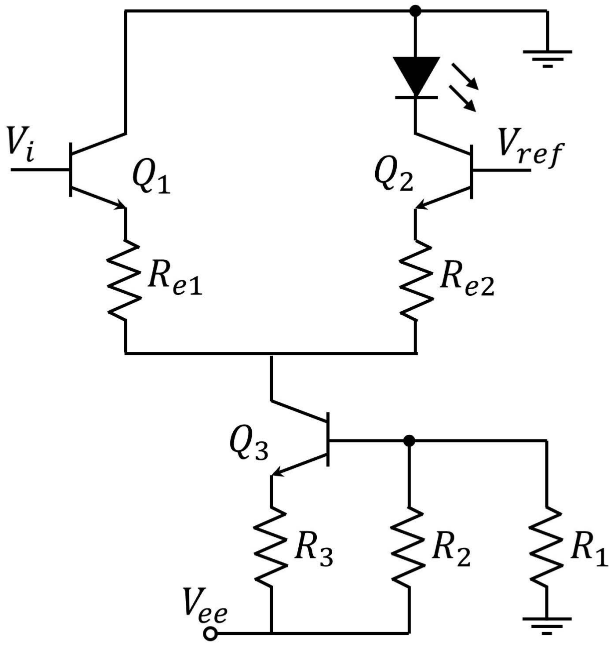

Figure 2.16: Differential amplifier driver circuit with constant-current source.

2.3.2. Photodetector conditioning circuits

Several designs have been proposed to amplify the photodetector current, both BJTs and Field-effect transistors (FETs) can be used for this purpose. The most common configurations based on transistors are the common emitter (or source) and the regulated cascode [55]. The low-impedance voltage amplifier is the simplest and is designed with a BJT transistor due to its low input impedance. Thermal noise can be reduced by using a transistor that has high gain at low emitter currents. The common gate configuration is less used because the high impedance of the photodiode reduces the power gain. On the other hand, is the regulated cascode configuration. This configuration takes advantage of the high transconductance of a BJT in the common base configuration, lowering the input resistance by the common emitter stage voltage gain.

Transimpedance amplifiers (TIAs) are preferred in most solutions because they offer high bandwidth with low input impedance while avoiding the major drawbacks of other configurations such as low sensitivity or limited bandwidth [56]. Even though the TIA can be configured in an open loop, the low control and easy saturation of these types of configurations make them undesirable. Therefore close-loop TIAs are going to be explored further.

Amplifier gain and bandwidth maximization have been relevant topics in electronic circuit design for a long time, mostly because many considerations must be taken into account to properly design a single supply amplifier, e.g. stability and voltage range limitations. The most basic configuration for the TIA is to use a feedback resistor that will dictate the gain of the stage. The TIA is configured as an invertig amplifier, meaning that the photodiode is connected to the inverting input. The ideal TIA transfer function considering the photodiode an ideal current source will be:

$$V_{out} = -I_{ph} R_f \tag{2.15}$$

As the photodiode can not be considered an ideal current source, its internal capacitance affects the behavior of the TIA gain stage and must be taked into account in the design (subsection 2.1.2).

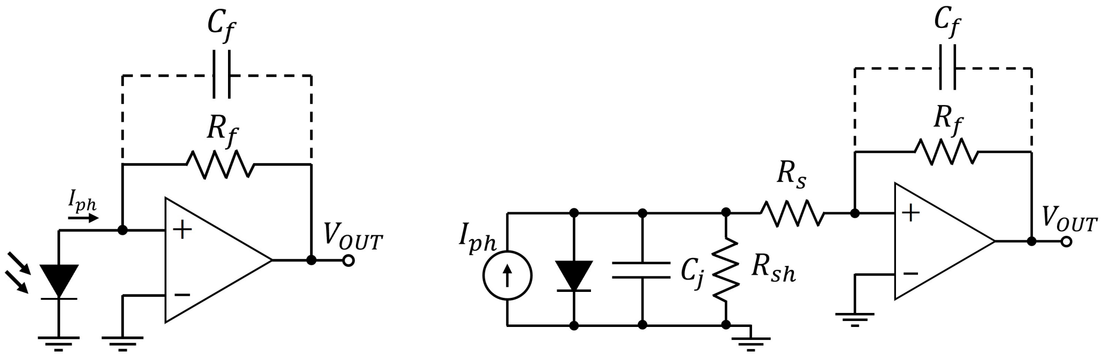

(a) TIA + photodiode (b) TIA + photodiode equivalent circuit

Figure 2.17: Basic transimpedance amplifier configuration

The stability of the circuit is determined by the noise gain (also known as the noninverting closed-loop gain). This is because any noise signal can cause oscillation in an unstable circuit. To obtain the transfer function the equivalent circuit of the photodiode and the feedback capacitor (C_f) must be taken into account (R_s is depreciated as its value is much smaller than R_f). The feedback capacitor is needed to maintain stability because it compensates for the photodiode capacitance [57]. Therefore, the transfer function follows the equation:

$$A_{close}(f) = \frac{R_f + R_{sh}}{R_{sh}} \cdot \frac{1 + j2\pi f (R_f || R_{sh})\,(C_f + C_{in})}{1 + j2\pi f R_f C_f} \tag{2.16}$$

Being the pole frequency:

$$f_p = \frac{1}{2\pi R_f C_f} \tag{2.17}$$

and the zero frequency:

$$f_z = \frac{1}{2\pi (R_f || R_{sh})\,(C_f + C_{in})} \tag{2.18}$$

Where C_{in} is the sum of the diode capacitance C_j and the amplifier input capacitance C_a, and common mode capacitance C_{cm}.

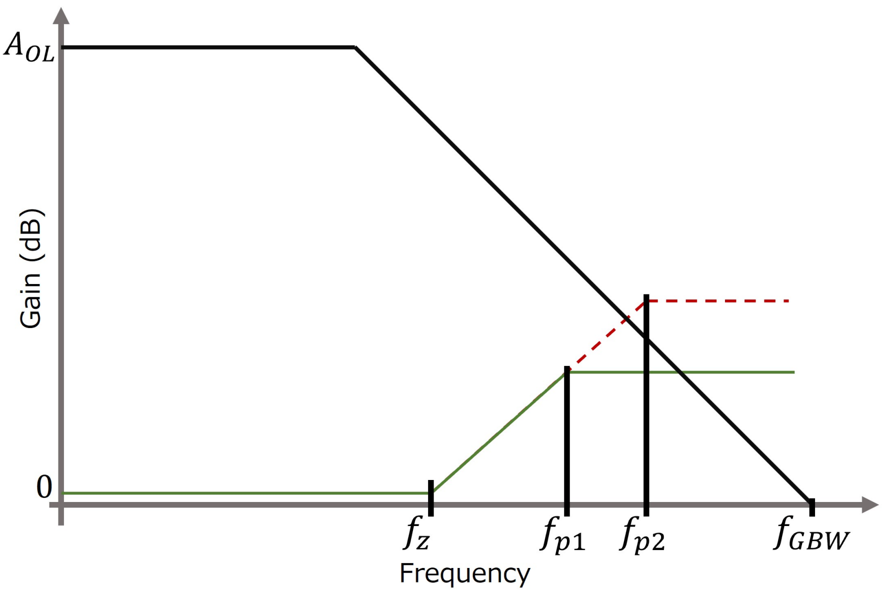

Figure 2.18: Multiple feedback response curves and open loop gain of a typical transimpedance amplifier.

Since the internal photodiode resistance R_{sh} is several orders of magnitude larger than the feedback resistance R_f ($R_{sh} >> R_f$), the result of the parallel combination will be equal to R_f. Also, as $(R_f||R_{sh}) \approx R_f$ and $C_f + C_{in} > C_f$ the zero will be always lower than the pole. If f_p is outside the open-loop gain curve, the system will be potentially unstable. Fig. 2.18 shows two feedback responses, where f_{p1} is a stable TIA and f_{p2} is potentially unestable.

Assuming that the capacitances are dominant for the high-frequency asymptote of the noise gain, the open-loop gain can be obtained by dividing Gain-bandwidth product (GBW) by f_p. Simple substitution produces a quadratic equation that can have only one real, positive solution, which gives a very good approximation of C_f [58]:

$$C_f = \frac{1}{4\pi R_f GBW}\left[1 + \sqrt{(1 + 8\pi R_f C_{in} GBW)}\right] \tag{2.19}$$

The transimpedance bandwidth, with some simplifying assumptions, can be obtained applying (2.20).

$$f_P \approx \sqrt{\frac{GBW}{2\pi R_F C_D}} \tag{2.20}$$

If the TIA have single supply, the amplifier lower voltage cannot reach 0 V. Therefore, when no light is detected ($I_{ph} = 0$) the output will saturate near to 0 V when the non-inverting input is grounded. In that sense, a resistor divider is used to bias the amplifier input above ground.

To prevent the input current from producing a voltage higher than the TIA power supply after amplification, the following equation can be applied:

$$R_f = \frac{V_{o(max)} - V_{o(min)}}{I_{ph(max)}} \tag{2.21}$$

2.4. Photobiological safety

Through close cooperation, the Commission Internationale de l'Eclairage (CIE), the Illuminating Engineering Society of North America (IESNA), and the International Electrotechnical Commission (IEC) have addressed the photobiological safety of lamps and lamp systems, including luminaires, on a global scale. The standards they have produced are the CIE S009, IEC 62471:2008, and the IESNA/ANSI RP-27 series [59]. Although not identical, the documents have a similar structure.

LEDs have a high radiance and luminance levels due to its small size, the luminance values can be greater than 10^7 cd/m^2. For comparison fluorescent lamps (1000 to $10,000$ cd/m^2) and halogen lamps (10^5 to 10^6 cd/m^2). Therefore, concerns have been raised regarding the extremely high brightness of most LEDs (even in low-powered applications). Three main criteria are used to analyze and evaluate the lighting environment: visual comfort, visual performance, and safety. The lighting solution is evaluated based on a number of variables such as brightness dis-

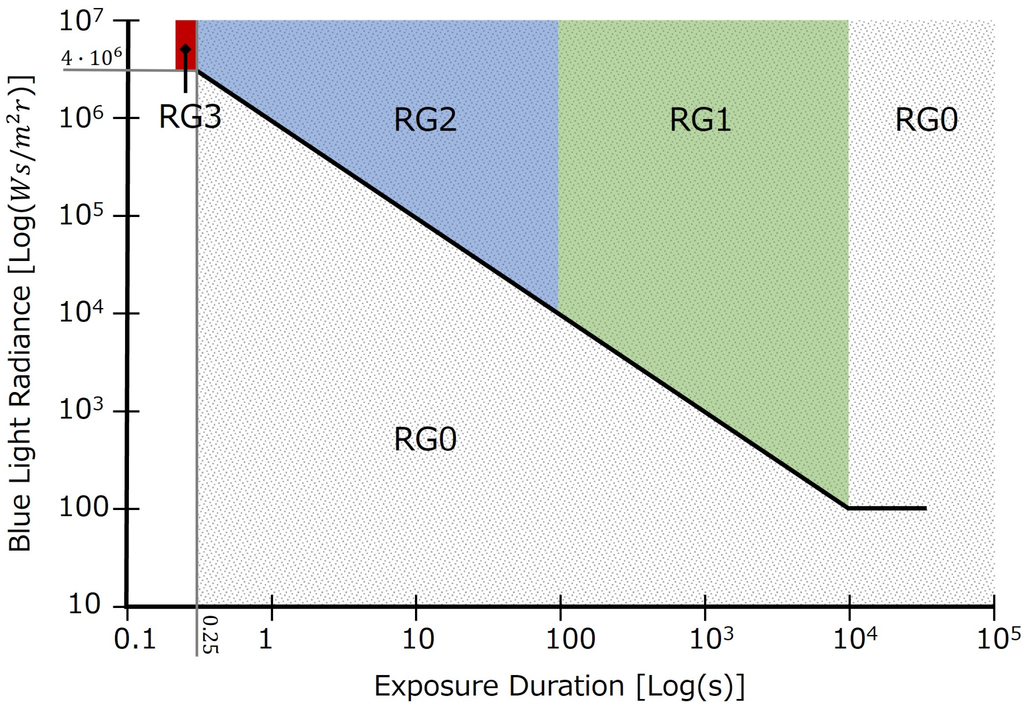

Figure 2.19: Blue-light hazard radiance ranges for the different risk groups (RG). Both axes are ploted in a logarithmic scale

tribution, illuminance, directionality and variability of light, color rendering, glare, and flicker [26].

In the case of LEDs, the current white light sources contain only the blue light hazard. The different hazard groups defined in CIE S009 and IEC 62471 are shown in Fig. 2.19 (based on [59]). Risk Group 0 is the exempt group, which represents no photobiological hazard under normal conditions. Risk Group 1 (low risk) includes products that present a risk only under very prolonged exposures. Risk Group 2 (moderate risk) is the group of devices that allow less exposure time than Group 1. Risk group 3 (high risk) should be avoided, these devices are potentially hazardous even for momentary exposures. Then, while the irradiance is under 100 W/m2 at a distance of 0.2 m in maximal directivity direction within 1000 s, non-coherent diffuse continuous-wave-modulated LEDs are exempt from classification and pose no photobiological hazard for the human eye in the standard IEC 62471:2008 [30].

In terms of flickering, frequencies over 5 kHz in motion or 200 Hz in static are desired to avoid the stroboscopic effect. Therefore modulations applied to the LEDs will not have a negative effect as the modulation is always over the hundred kHz. On the other hand, when dimming, there is a possibility of a modulation of this kind, depending on the technique used for dimming [59].

3 Modulation formats for VLC

"It is not nearly so important how well a message is received as how well it is sent..."
Neale Donald Walsch

As in any communication process, the message should be encoded by the sender and decoded by the receiver. Since the message is theoretical and intangible, its further transmission requires codifying it into symbols. The process of converting the message into these symbols is called modulation. Also, the inverse process of recovering the message from the symbols is known as demodulation.

OWCs have been used since ancient times. An example of it could be which can be considered the first explicitly described communication method, developed by historian Polybius, in which torches were used in order to exchange information. This was done by establishing an agreement between emitter and receiver where the alphabet was represented by a set of five torches and five different tables. Making it possible to have 5^2 different combinations (ancient Greek alphabet had 24 letters). Therefore any message can by send by the combination of torches showed to the receiver side. Sending the message letter by letter for long distances [60].

Therefore, the modulation format used to transmit the information is a key element and must be known to correctly demodulate the information and make the message recoverable. In addition, the modulation format can improve or degrade communication because it is affected by the channel characteristics, e.g., in the case of the torches, the communication process is different on a clear night than on a foggy day. When it comes to OWC systems, the majority use IM/DD [6, 53] where the transmitter modulates the light intensity, and the receiver detects and converts the light changes into electrical changes before electrical demodulation and demultiplexing. The optical modulations are limited to the characteristics of the channel, since the optical information must be real and cannot be negative, these characteristics are two of the biggest differences compared to the RF modulation techniques.

The information can be modulated by using the characteristics of the wave to create a clear and different representation for each symbol. There are basically three different ways in which the carrier can be modulated to encode the information, amplitude, frequency, and phase angle. Although the frequency and phase modulations do not appear to be intensity modulations, they may be transmitted by varying the signal amplitude. On the receiver side, as mentioned earlier, the light changes are converted to electrical variations and then decoded using the amplitude, frequency, phase, or a combination of them.

The chosen modulation must be power efficient since the total power available in the transmitter is limited by the dynamic range of the LEDs and also by power safety considerations. It should also be noted, that while more complex modulations are bandwidth and power efficient, and in most cases more robust, they are more expensive to implement in terms of overall price, design time, and deployment. Therefore, simpler implementations are still an alternative and are attractive for certain solutions. An overview of the most common modulation schemes used in OWC systems will be discussed further.

3.1. OOK

On-Off keying (OOK) modulation is one of the most widely used modulation schemes in OWCs due to its simplicity, power efficiency, and resistance to nonlinearity [26]. OOK can be defined as the simplest form of Pulse amplitude modulation (PAM)

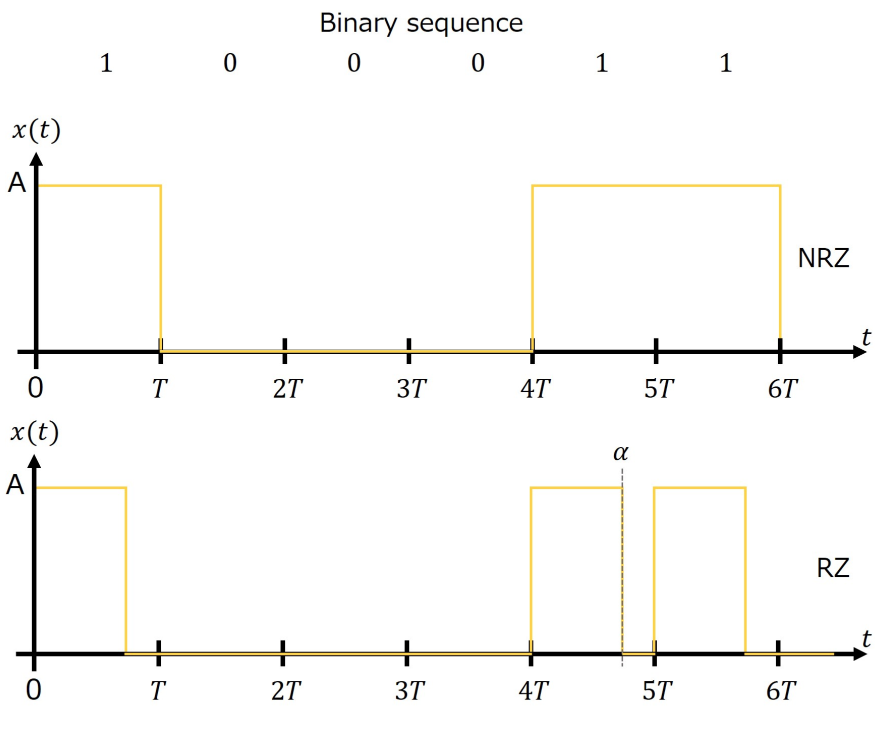

Figure 3.1: OOK signal waveform for NRZ and RZ formats.

known as binary PAM or just 2-PAM. The discrete information can be used directly as the baseband signal to be transmitted, where the digital one represents the maximum optical power, and the digital zero represents no power for the case of unipolar (positive) signals. Also, the digital information can be used as modulator of a carrier signal (filtering it), codifying the information as presence or absence of optical signal energy.

Assuming a pulse repetition of T_{ook}, the optical pulse that represents a digital one can be as long as the symbol duration αT_{ook} where $\alpha = 1$ or can be confined inside it, where $\alpha < 1$. These two different pulse formats are known as Non-return-to-zero (NRZ) and Return-to-zero (RZ), respectively. A comparison of the NRZ and RZ waveforms is shown in Fig. 3.1. When comes to compare the NRZ and RZ formats, the reduced duration of the one directly impacts the power efficiency by having more time the signal at low level. However, the spectral efficiency is worst as the required bandwidth is given by $1/\alpha T_{ook}$. In most of the cases NRZ is prefered over RZ, as VLC channels usually have a limited bandwidth. In addition, the bit recovering system required for NRZ is simplier than RZ as each symbol transmitted occupates the maximum time allowed in the continuous time signal (T_{ook}) [26].

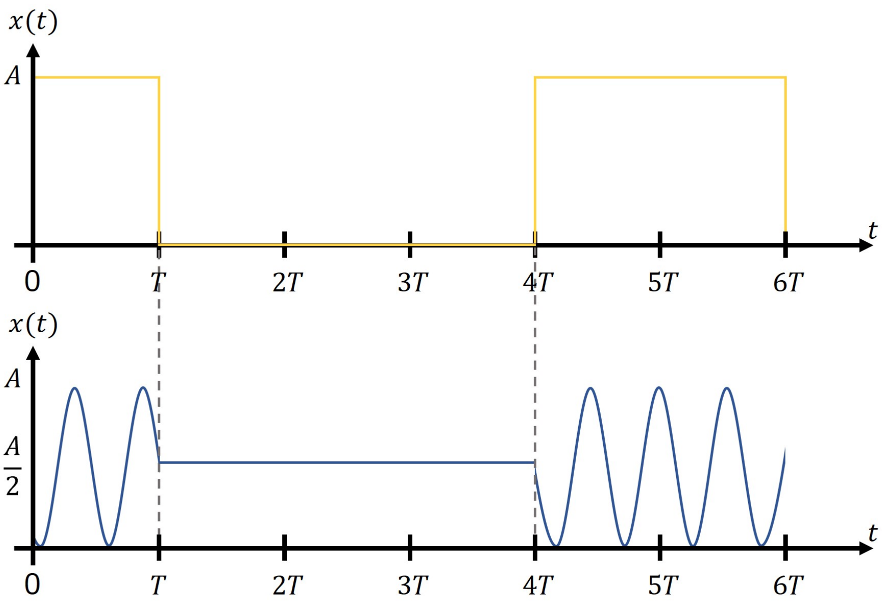

Figure 3.2: Binary amplitude modulated carrier signal.

If the digital information is encoded directly as a baseband signal, the channel bandwidth required to transmit the information without significant distortion must be about $1/\alpha T_{ook}$ [61]. As mentioned above, the transmitted signal cannot be negative, so the carrier signal is shifted into the positive range by adding a DC level to the signal. Fig. 3.2 shows the waveform of the continuous carrier signal after amplitude modulation. The equation that models the transmitted signal for the amplitude-modulated carrier is:

$$s(t) = \sum_{k=0}^{K} a[k] \cdot p(t - k(\alpha T_{ook})) \cdot cos(\omega_c t + \theta_c) \tag{3.1}$$

Where the baseband signal is a special case of the previous equation, where the carrier signal is just DC, i.e., there is neither frequency nor phase ($\omega_c = 0$ and $\theta_c = 0$). The resulting equation for a baseband PAM is then:

$$\hat{s}(t) = \sum_{k=0}^{K} a[k] \cdot p(t - k(\alpha T_{ook})) \tag{3.2}$$

Where $a[k]$ is a discrete signal that dictates the pulse amplitude at time t, in the case of OOK $a[k] \in [0, 1]$, K is the number of transmitted symbols, and $p(t)$ is given by:

$$p(t) = \begin{cases} A/\alpha, & t \in [0, \alpha T_{ook}] \\ 0, & \text{otherwise} \end{cases} \tag{3.3}$$

On the receiver side, the signal is then sampled every T_{ook} and then compared to a threshold to determine if it is a one or a zero. The ideal threshold is halfway between the expected power of the one and the zero in a channel with equiprobable symbol occurrences. In addition, the transmitted signal is affected by the channel characteristics, and then the received signal can be modeled as:

$$z(t) = \mathcal{R} \cdot (h(t) * s(t)) + \eta(t) \tag{3.4}$$

Where $h(t)$ is the impulse response of an linear time-invariant (LTI) channel, $\mathcal{R}$ is the photodetector responsivity given in (2.6), and $\eta(t) \sim N(0, \sigma^2)$ represents the channel noise as an Additive white Gaussian noise (AWGN) with two-sided power spectral density N_0 and variance σ^2 [62]. The block diagram of the OOK model is shown in Fig. 3.3, where $f(t)$ is a receiver filter.

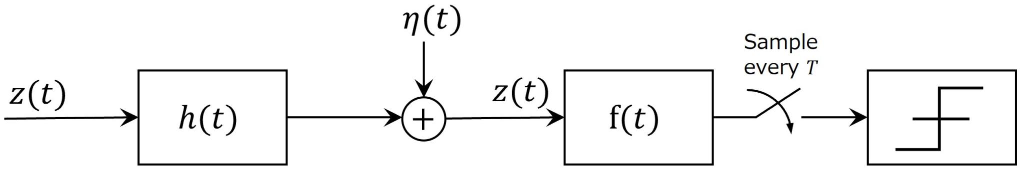

Figure 3.3: Block diagram of an OOK system.

The bit error probability of an OOK modulation in an AWGN channel is given by [63]:

$$P_e = \mathcal{Q}\left(\frac{SNR}{2}\right) \tag{3.5}$$

Where $\mathcal{Q}$ is the Q-function and the SNR is:

$$SNR = \frac{\mathcal{R}^2 P_r^2}{N_0 R_b} \tag{3.6}$$

where P_r is the average received optical power and R_b is the bit rate. It is important to note that the error probability of the transmitted ones and the error probability of the transmitted zeros are different in a VLC system when a photodiode is used as the detector. In fact, most of the bit errors will occur in the transmitted ones because the receiver could not convert the received light into the desired current, but in very rare cases, when the transmitted power is zero, the photodetector generates a high enough current with no light.

Furthermore, although the pulses are perfectly square in an ideal system, this is not true in a real system where the limited bandwidth of the system filters the infinite frequencies that make up a square signal. As a result, the energy of each symbol is dispersed, resulting in some cases of overlapping symbols Intersymbol interference (ISI) that interfere with proper symbol identification at the receiver.

3.2. PPM

In Pulse position modulation (PPM), each symbol, which always has the same time duration, is divided into L time slots of equal length, where L is the number of different pulses that can be encoded in each symbol. Then, as the name suggests, the information is encoded in the slot where the impulse is placed within a symbol [64]. All other time slots of the symbol are kept at a low level. Therefore, it can be concluded that the power efficiency of PPM is lower compared to the NRZ OOK, but this technique, like the RZ, requires higher bandwidth and is more complex to implement. The high power efficiency makes this modulation widely used in low-

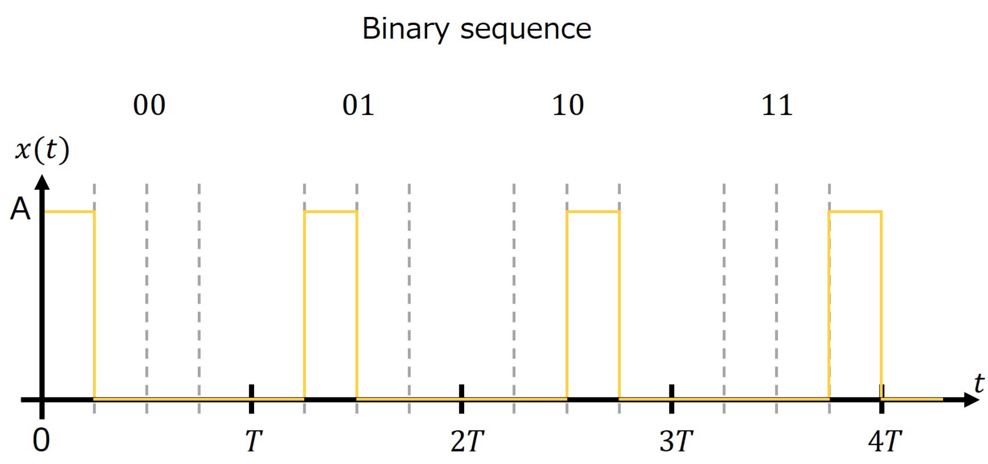

Figure 3.4: Time waveform of a 4-PPM.

power (handheld) devices. The time slots L are usually chosen as powers of two to make it easy to encode n bits in each position, where $n = log_2 L$ [65].

A good analogy to understand modulation is the method used by Polybius, explained at the beginning of this chapter, where the torches represent each time slot, so in each time (selected table), the number of torches, in this case, the position of the pulse, will dictate the information contained in that time slot, and the process will repeat in each time slot until the message is sent. Fig. 3.4 shows the different waveforms that can occur in a 4-PPM without losing generality. To maintain the same throughput as OOK, the time duration of the PPM symbol T_{ppm} must be shorter than the OOK bit duration by a factor of L/n. The PPM time domain signal can be expressed as [63]:

$$x(t) = LP \sum_{k=0}^{L-1} c_k p_{ppm} \left(t - \frac{k T_{ppm}}{L} \right) \tag{3.7}$$

Where $c_k \in c_0, c_1, c_2, ..., c_{L-1}$ is the PPM codeword, LP is the peak power average constant to ensure that $|x(t)| \leq P$, and $p_{ppm}(t)$ is given by:

$$p_{ppm}(t) = \begin{cases} 1, & t \in \left[(l-1)\frac{T_{ppm}}{L}, l\frac{T_{ppm}}{L} \right] \\ 0, & \text{otherwise} \end{cases} \tag{3.8}$$

For $l \in 1, 2, ..., L$. Where l is the position of the active subinterval of the k'th symbol.

From the previous explanation, it can be deduced that the transmitter and receiver must be perfectly synchronized for correct pulse position identification. An error in symbol windowing will result in incorrect pulse position identification and therefore, a bit error. The bit probability in PPM, unlike in OOK modulation, is unbalanced for $L > 2$ since there are L-1 zeros in each symbol and only one slot with power. Therefore, the optimal threshold is a complicated function that includes the number of slots per symbol L and the signal and noise powers. However, if we consider an AWGN with low error probability, the PPM time slot error probability can be defined as [26]:

$$P_{sle} = \mathcal{Q} \left(\sqrt{\frac{Ln}{2}} \frac{\mathcal{R} P_r}{sqrt(N_0 R_b)} \right) \tag{3.9}$$

3.2.1. VPPM

Variable pulse position modulation (VPPM) uses a binary PPM (2-PPM) for communication and adds dimming control with Pulse width modulation (PWM) [66]. Specifically, the time slot duration of the high pulse is no longer fixed and can be changed to achieve the desired average power on transmission. Since the PPM is binary, the symbol representing the zero and the symbol representing the one have the same average power, which makes it unlikely that there will be flicker noise in the transmission signal [67]. The value of each symbol is defined by the position of the high pulse within the period. Fig. 3.5 shows different dimming levels of a given VPPM scheme. A zero is encoded when the high pulse begins the symbol, and a one is encoded when the high pulse ends the symbol.

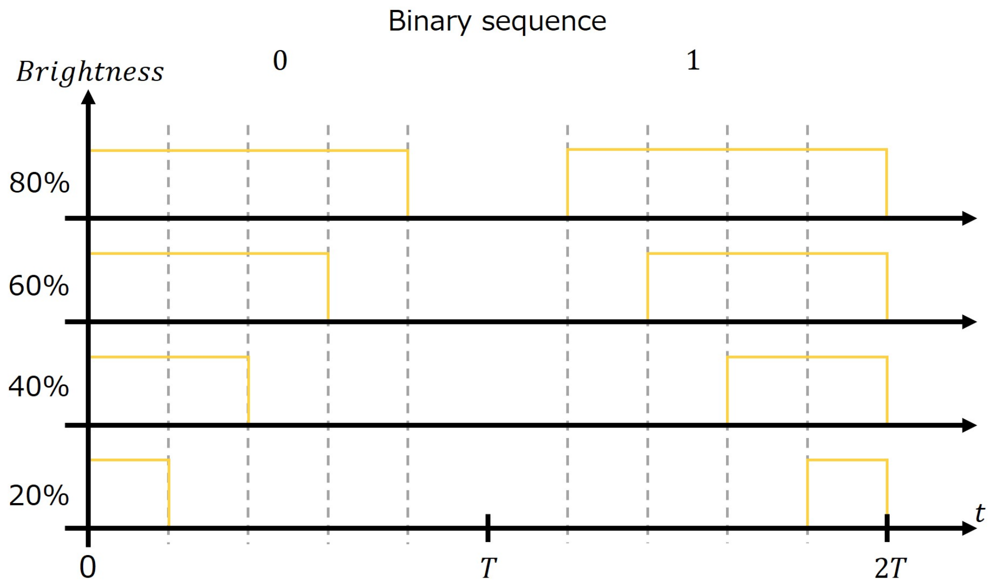

Figure 3.5: Different dimming levels on a VPPM scheme.

The continuous time VPPM signal can be modeled as [68]:

$$x(t) = \sum_{k=0}^{K} s(t - kT_{vppm}) \tag{3.10}$$

Where $T_{vppm} = T_s + T_g$ is the signal periode, where T_s is the symbol duration and T_g is the time guard added to avoid ISI, and $s(t)$ is given by:

$$s(t) = \begin{cases} \sqrt{E_s \cdot \frac{d}{50}} \cdot \varphi_0(t, d), & b = 0 \\ \sqrt{E_s \cdot \frac{d}{50}} \cdot \varphi_1(t, d), & b = 1 \end{cases} \tag{3.11}$$

Where $b \in 0, 1$ is the binary data, E_s is the symbol energy, $d \; \forall \; 0 \leq d \leq 100$ is the dimming level, and $\varphi_i(t, d) \; \forall \; i = [0, 1]$ is the basis function that depends on the dimming level. The basis depicted in Fig. 3.6 follows [68]:

$$\varphi_0(t, d) = \begin{cases} \sqrt{E_s \cdot \frac{100}{dT_s}}, & 0 \leq t \leq \frac{dT_s}{100} \\ 0, & \text{otherwise} \end{cases}$$

$$\varphi_1(t,d) = \begin{cases} \sqrt{E_s \cdot \frac{100}{dT_s}}, & \left(1-\frac{d}{100}\right) T_s \le t \le T_s \\ 0, & \text{otherwise} \end{cases} \tag{3.12}$$

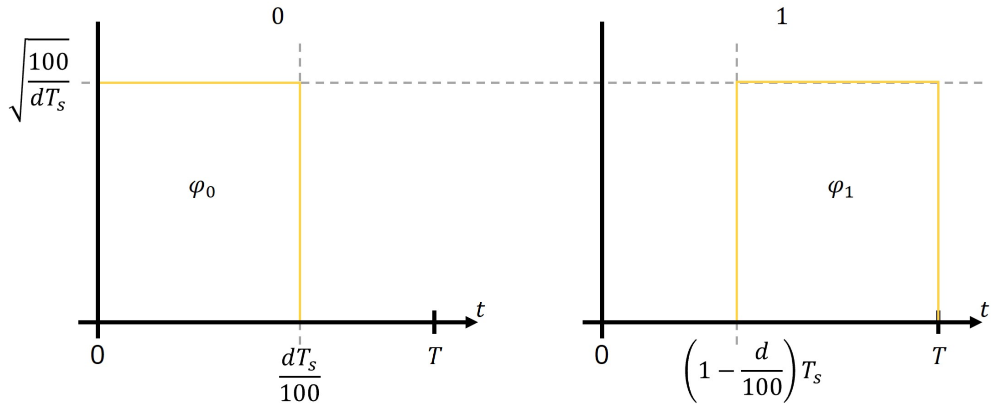

Figure 3.6: Signal representation of the basis function.

Assuming that the channel has equiprobable symbol occurrences, the error probability of VPPM is given by [68]:

$$\begin{aligned} P_e &= P\{b=0\} \cdot P_{e|b=0} + P\{b=1\} \cdot P_{e|b=1} \\ &= \frac{1}{2} \operatorname{erf} c \left(\gamma \cdot \sqrt{\frac{E_s}{2N_0}} \cdot \sqrt{\frac{d \cdot (1-\alpha)}{50}} \right). \end{aligned} \tag{3.13}$$

3.3. PWM

In Pulse width modulation (PWM), the information within the symbol is codified using the pulse width maintaining its position, different from PPM where the pulse width is always equal. But, as in PPM, the synchronization between transmitter and receiver must be good enough to window each symbol correctly. PWM offers dimming options as in the case of VPPM, and each symbol can codify more than one bit. Saying that the symbol length is given by $log_2 L$, where L is the number of different widths in each PWM symbol, with a symbol rate $T_{pwm} = log_2 L/R_b$, where R_b is the input bit rate. The PWM time domain signal can be expressed as [65]:

$$x(t) = A \sum_{k=0}^{K} p_{pwm}\left(t - kT_{pwm}\right) \tag{3.14}$$

Where A is the power factor that ensures that the signal has the desired signal power average P, given by:

$$A = \frac{2L}{L+1} P \tag{3.15}$$

And $p_{pwm}(t)$ is given by:

$$p_{pwm}(t) = \begin{cases} 1, & t \in \left[0, l\frac{T_{ppm}}{L}\right] \\ 0, & \text{otherwise} \end{cases} \tag{3.16}$$

For $l \in 1, 2, ..., L$. Where l is the length of the active signal within the symbol depicted in Fig. 3.7.

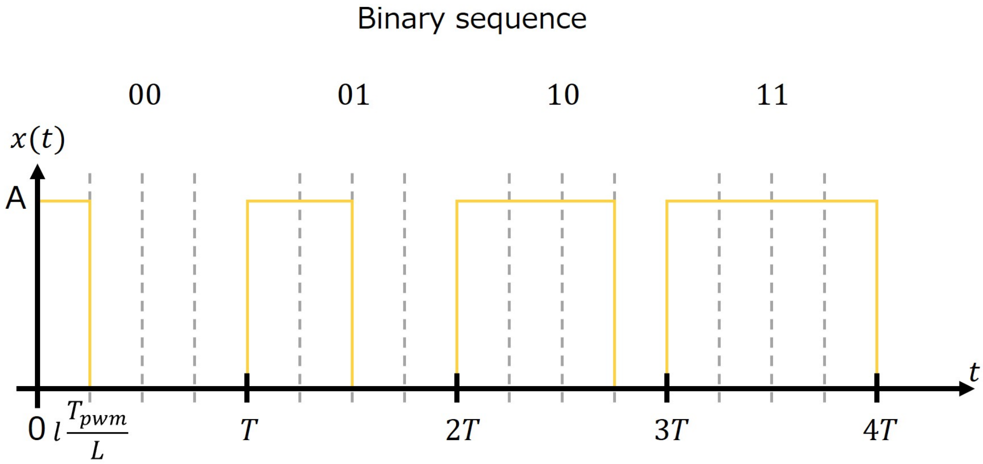

Figure 3.7: Time waveform of a 4-PWM.

3.4. Orthogonal Frequency Division Multiplexing

Orthogonal frequency division multiplexing (OFDM) is a multicarrier modulation format that, although more complex than all the modulations mentioned before, offers many advantages, such as its robustness, high bandwidth efficiency, and better optical efficiency [69]. Therefore, this method is very interesting in applications where it is necessary to explore the maximum data rate that the channel can offer (especially in low bandwidth channels like the case of the LEDs).

Nowadays, OFDM wireless transmission is a well-known technique and is integrated in our daily life in standards such as WiFi or LTE. However, its application in optical wireless channels presents unique challenges that have attracted the interest of researchers to improve and adapt OFDM for this type of applications, including VLC [62, 70, 71].

OFDM is a special case of Frequency division multiplexing (FDM) where the subcarriers can be overlapped in the frequency domain without creating ISI due to the orthogonality principle, resulting in higher spectral efficiency as shown in Fig. 3.8. The orthogonal characteristic of the subcarriers allows the recovery of each subcarrier at the receiver without complicating the analog structure of the receptor, as in OFDM the modulation and demodulation of the temporal signal are achieved

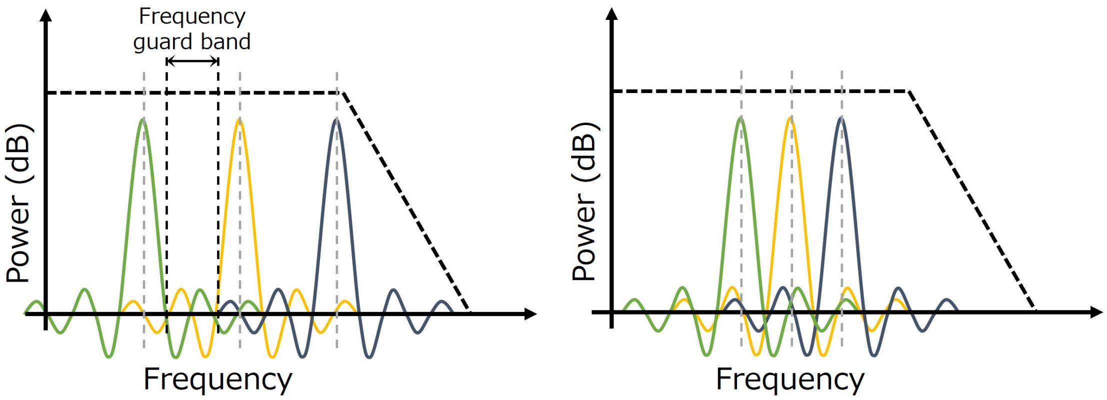

(a) (b)

Figure 3.8: Spectral distribution of (a) FDM signal and (b) OFDM signal

digitally employing the IFFT and Fast Fourier transform (FFT), respectively. It is then clear that the guarantee of orthogonality between the carriers is a must to avoid the loss of the transmitted information.

Another relevant aspect is the time dispersion induced by the channel. As mentioned earlier, the limited bandwidth of the system disperses the energy of each symbol, resulting in ISI. In serial data transmission, the symbol period is inversely proportional to the bit rate. Therefore, at higher data rates, the symbol duration will be very small, increasing the channel ISI since the delay is comparable to the symbol duration. Here, OFDM provides a solution. In OFDM, the channel is divided into N low-rate subcarriers, then each of these subcarriers is individually modulated using any traditional modulation technique (e.g., OOK, QAM, PPM) [72], and then transmitted in parallel. This means that the symbol duration on each subcarrier is N times longer than other single-carrier modulation for the same data rate [73].

It can be concluded that the higher the number of subcarriers, the better, since more data can be sent in parallel in channels with larger delay spreads. However, as N increases, the width of the subcarriers in frequency becomes smaller, resulting in the need for very precise elements on both sides of the communication to avoid any distortion, making the system more complex and costly. Therefore, the number of subcarriers must be chosen to meet the needs of the channel while keeping the system as simple as possible. The OFDM time signal can be defined as [74]:

$$s_n(t) = \sum_{k=0}^{N-1} S_{n,k} g_k \left(t - n T_{ofdm}\right) \tag{3.17}$$

Where $S_{n,k}$ are the symbols mapped to the k-th subcarrier in the chosen modulation, and n refers to the time interval. $g_k(t)$ is the k-th unmodulated subcarrier signal defined by [74]:

$$g_k(t) = \begin{cases} e^{j2\pi k \Delta f t}, & t \in [-T_g, T_s] \\ 0, & \text{otherwise} \end{cases} \tag{3.18}$$

Where $k\Delta f$ is the carrier frequency, T_s is the symbol duration, and T_g is the time guard added to avoid ISI. The total OFDM symbol duration is then $T_{ofdm} = T_s + T_g$. On the other hand, even when multiple time guard methods have been used to reduce the ISI, the most common is the Cyclic prefix (CP) [75]. The CP method consists in adding a copy of the last part of each symbol at the beginning of it. The size of the CP should be defined greater than the maximum expected channel delay to avoid loss of orthogonality [70]. The CP is removed in the receiver after time synchronization.

Since the multiple time signals are shaped by a rectangular pulse, the frequency spectrum of each is a *sinc* function. All the N *sinc* functions are spaced by Δf in the frequency spectrum.

3.4.1. Considerations for OFDM implementations on VLC channels

In the case of VLC channels, a LED is used as a transmitter, and the modulation scheme is IM/DD. Then the transmitted time signal must be real and positive (unipolar). There are two common ways to get a real signal from OFDM. The first has two outputs from the IFFT module, creating one signal containing the real output of the IFFT (in-phase) and another containing the complex part (quadrature). These signals are converted to the analog domain using a DAC, then each modulates a sine or cosine wave (that has the same frequency). Finally, to obtain

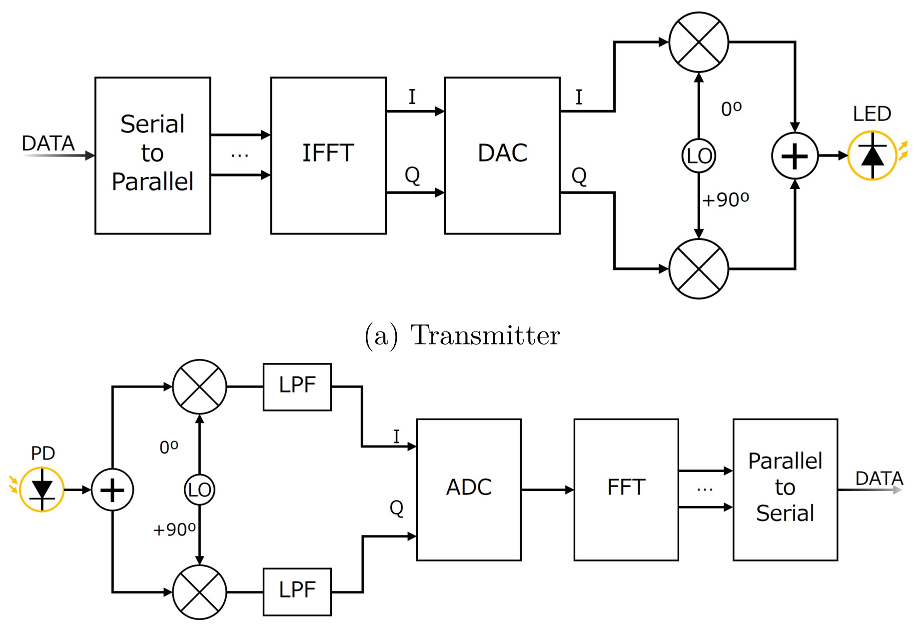

(a) Transmitter

(b) Receiver

Figure 3.9: Block scheme of I/Q OFDM.

the real transmission signal, both signals are added as shown in Fig. 3.9. On the receiver side, the same process must be followed. The signal is split and multiplied by the same baseband signal used in the transmitter, then filtered and passed to the digital domain using an ADC. The two recovered in-phase and quadrature signals are passed to the FFT module to recover the symbols (Fig. 3.9).

The second one, and the one that will be the basis from now on, achieves a real signal by taking advantage of the hermitian symmetry [76]. In a Fourier transform, if the input time-domain signal is real, then the transformed signal has a symmetrical conjugate output with respect to the central frequency [77]. In other words, each subcarrier must contain its complex conjugate to obtain a real signal output at the IFFT [78]. As a result, there are half as many subcarriers carrying information, but the design is more flexible and has less analog complexity. The hermitian symmetry of the complex data $X = [X_0, X_1, ..., X_{N-1}]$ can be defined as:

$$X_m = X^*_{N-m} \quad for \quad 0 < m < \frac{N}{2} \tag{3.19}$$

Where the DC component and the $\frac{N}{2}$ must be zero ($X_0 = X_{N/2} = 0$). Hardware downsizing and tiny solutions benefit from the reduction in implementation hardware. In addition, problems associated with I/Q imbalance are avoided. A block diagram of an OFDM system using hermitian symmetry is shown in Fig. 3.10.

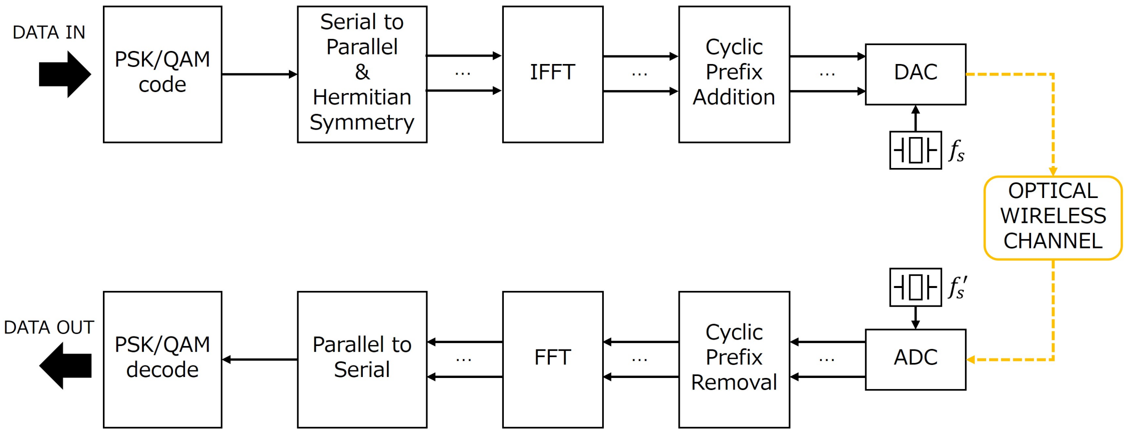

Figure 3.10: Block diagram of OFDM system with hermitian symmetry.

Although the hermitian symmetry ensures a real output from the IFFT block, the signal is still bipolar, which is not suitable for the LED. There are three common ways to convert the bipolar signal to a positive one. One is to add a DC offset high enough to ensure that the lower values are still positive (DCO-OFDM) [79], the other is to clip the signal at zero, resulting in a loss of the information contained in the negative part of the signal (ACO-OFDM) [80], the third is to create a unipolar signal by reversing the sign of the negative part of the signal while keeping the positive part intact (U-OFDM) [81].

DCO-OFDM is the most spectrally efficient of the three and is easy to implement. The modulated signal is shifted up by adding a DC signal before it is sent to the LED. This can be done with any of the previously described circuits on the subsection 2.3.1. In contrast, the DCO OFDM is very energy inefficient [79]. But in the case of VLC applications, where the transmitter is used for both lighting and communication, it is the most common and preferable approach to obtain a suitable unipolar signal without distortion, as the DC offset ensures an illumination level. A comparison between a bipolar OFDM and a DCO-OFDM is shown in Fig. 3.11.

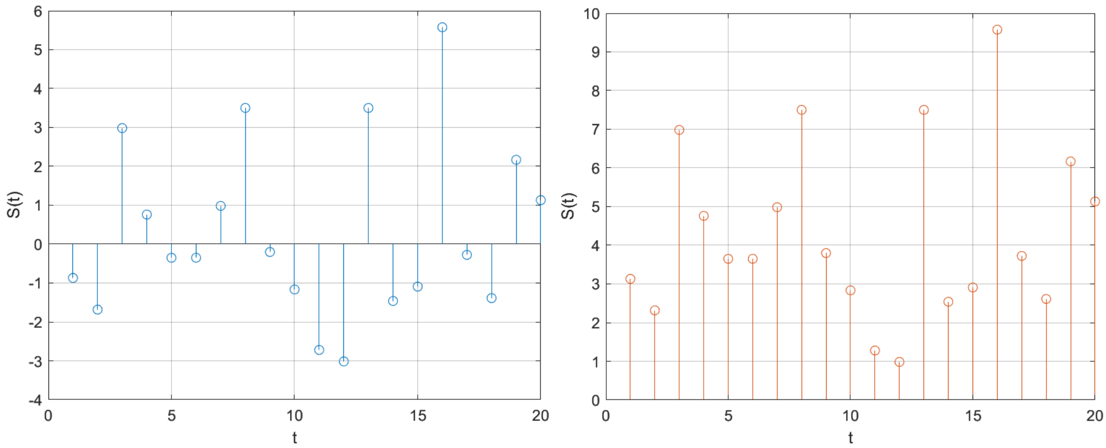

(a) (b)

Figure 3.11: Samples of a typical (a) bipolar and (b) DCO time domain OFDM signal.

ACO-OFDM appears as an option to obtain a real signal without "waisting energy" in DC. The resulting signal is clipped at zero level, and it turns out that the noise introduced by clipping only affects the even subcarrier when only the odd OFDM subcarriers are non-zero at the IFFT input, leaving the odd subcarrier -which carries the data- unaffected [62]. Therefore the spectral efficiency of ACO-OFDM is half of the DCO-OFDM. This method is preferable on the uplink side, where commonly, no illumination is needed, and the receiver device is energy limited (can even be portable). A comparison between a bipolar OFDM and a ACO-OFDM is shown in Fig. 3.12.

U-OFDM is an alternative to ACO-OFDM. In this case, the signal is not clipped, but two signal blocks are created by encoding each sample into a new pair of samples. The first sample of the new pair is set to the original value, and the second sample is set to zero if the initial OFDM sample is positive. On the other hand, if the initial OFDM sample is negative, the first sample of the new pair is set to zero, and the second sample is set to the absolute value of the original sample [81]. Then the original positive sample pairs are transmitted first in the block, followed by the original negative samples. The advantage is that no information is lost in the clipping, and the original signal can be easily recovered by subtracting the negative and positive blocks (shown in Fig. 3.13).

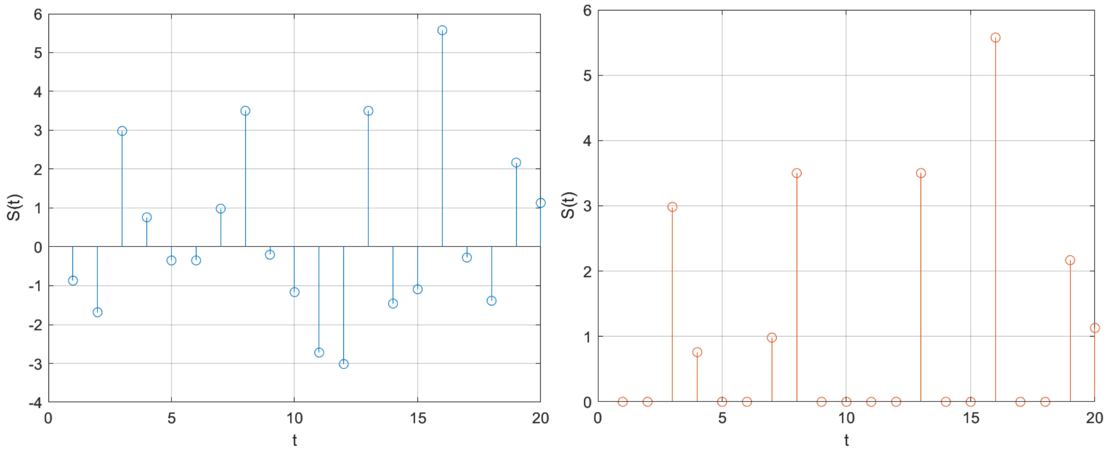

(a) (b)

Figure 3.12: Samples of a typical (a) bipolar and (b) ACO time domain OFDM signal.

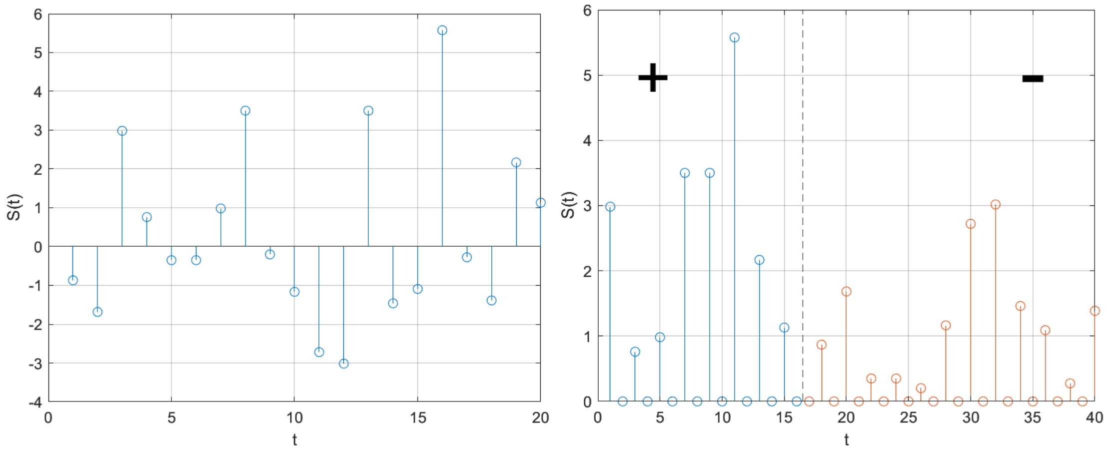

(a) (b)

Figure 3.13: Samples of a typical (a) bipolar and (b) flip(U) time domain OFDM signal.

Furthermore OFDM is very sensitive to channel effects. The channel introduces delays and distortions to the time signal that must be addressed in the receiver to avoid errors in the data [82, 83]. Some common problems that need to be addressed in the receiver are time offset, Carrier frequency offset (CFO), Sampling frequency offset (SFO), and Phase noise (PN). All of these create a phase offset in the received constellation. The time offset produces a phase offset that is the same for all subcarriers and does not vary with time. While the one caused by CFO is constant for each subcarrier but varies with time. On the other hand, the phase offset caused by SFO varies with time and depends on the position of each subcarrier.

The first goal on the receiver side is to detect the beginning of an OFDM symbol. Although this is not always an easy task as the data does not contain any special signaling to indicate the beginning. If the synchronization is not performed well, a delayed or early detection of the OFDM symbol occurs, as shown in Fig. 3.14. When the symbol is detected with delay, samples from other symbols are introduced into the FFT window, causing that the information will never be recoverable as the symbol is no longer complete in the FFT window [84].

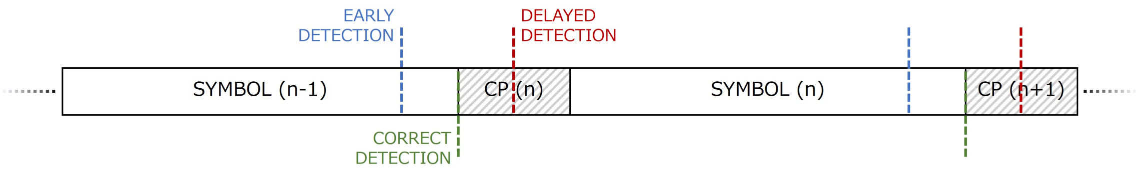

Figure 3.14: Time offset because an error in first OFDM symbol detection.

However, in the case of early detection, if the displacement samples are smaller than those contained in the CP, the symbol is complete inside the FFT, but in the wrong order (since the CP contains the last part of the symbol). The misplacement of the elements is reflected as a phase offset (rotation of the points) after the FFT. To estimate and compensate for this offset, some "special" samples containing known information, commonly known as pilots, are used. On the other hand, even when the detection of the message is correct the receiver and transmitter are isolated, meaning that the clock signal that govern each is different and independent. This leads to differences in the sampling points.

Then, to represent these phase offsets mathematically lets assume a sequence of M complex symbols are modulated into M subcarriers in the transmitter applying the IFFT, resulting in:

$$s(k) = \frac{1}{M} \sum_{i=0}^{M-1} din(i)\, e^{\frac{j2\pi ik}{M}}, \quad k = 0, ..., M-1 \tag{3.20}$$

Where $din(i)$ is the data symbol in the ith subcarrier, and $s(k)$ is the kth sample of the OFDM symbol [85]. Assuming a single-path channel, the received signal can be defined as:

$$r(k) = s(k-\tau) + w(k) \tag{3.21}$$

Where τ is the time offset and $w(k)$ is the AWGN induced by the channel. The received signal is then demodulated using FFT to extract the symbols, resulting in:

$$R(i) = din(i)\, e^{\frac{-j2\pi i\tau}{M}} \tag{3.22}$$

Where $e^{\frac{-j2\pi i\tau}{M}}$ is the phase rotation of each symbol due to the time offset τ [86]. Which shows that the induced phase offset is determined by:

$$\Delta\theta_i = \frac{2\pi}{M} i * \tau \tag{3.23}$$

Where $\Delta\theta_i$ is the angle difference between the received symbols and the transmitted ones due to a wrong detection (time offset) and the mismatch between f_s and f_s' (Fig. 3.10) in the ith subcarrier.

Therefore, to correctly estimate the SFO, it is first necessary to ensure that the symbol is detected in time and that the phase rotation after the FFT is only due to the sampling mismatch. To this end, we propose in [84] a post-FFT synchronization method to estimate the phase offset for systems with hermitian symmetry along with the implementation of a pre-FFT synchronization stage to perform the equivalent time correction with a one-sample accuracy. Both the time synchronization and the phase correction methods were developed within the framework of the MEDIALIFI project (financed by OPTIVA MEDIA), with the invaluable participation of the GDAF and GMA groups of the DTE of UC3M.

3.4.2. Proposed time synchronization technique

The proposed algorithm is independent of the encoding format used in the data carriers. To identify the beginning of an OFDM package two preambles are defined: short and long preamble [72]. In general, time synchronization has two stages: coarse synchronization and fine synchronization [87]. The start of an OFDM packet is estimated using coarse synchronization. The frequency offset is calculated using fine synchronization. These two can be performed before the FFT in non-Hermitian symmetry OFDM systems using the real and imaginary components of the received OFDM signal. Since there is no imaginary component in hermitian-symmetric OFDM systems, these techniques cannot be used. Therefore the proposed method combines a pre and post-FFT detection combined with a time correction applied to the CP elimination as shown in Fig. 3.15.

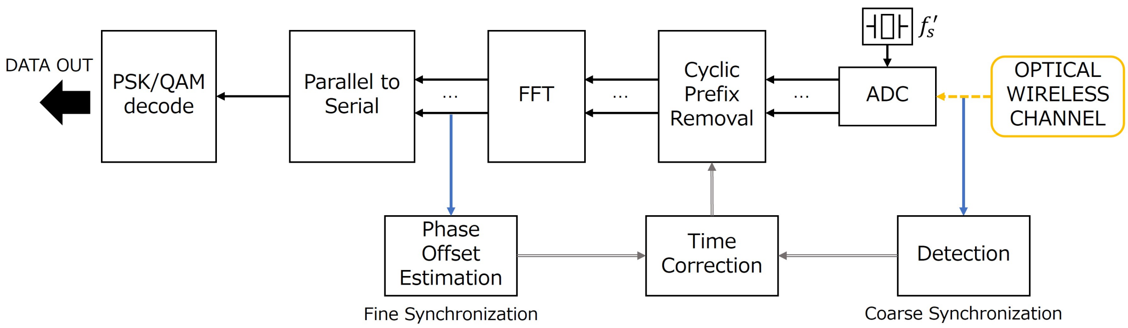

Figure 3.15: Time synchronization for OFDM system with hermitian symmetry.

The Schmidl & Cox Maximum normalized correlation (MNC) algorithm is used for the coarse detection stage. Where the metric signal is obtained from the auto-correlation normalized with respect the signal power helping to reject wrong detections when the noise cause a high enough auto-correlation value. The metric is then defined as:

$$m_n = \frac{|c_n|^2}{p_n^2} \tag{3.24}$$

Given that the hermitian symmetry ensures that the autocorrelation and the power signal do not have a complex component, the (3.24) can be expressed in the following way:

$$m_n = \frac{c_n}{p_n} \tag{3.25}$$

Where c_n is the correlation signal, and p_n is the signal power follows:

$$p[n] = \sum_{i=0}^{N_{train}-1} |S(n+i)|^2 \tag{3.26}$$

Where N_{train} is the training symbol size. A threshold is defined for the metric to ensure that a posible package has arrive. Then, to be as precise as posible, an algorithm to detect the maximum value (peak) of m_n is proposed. The algorithm compares the current sample (if the threshold is already passed) with the previous registered and then register the higher value. This simplify a lot the implementation as only two registers and a comparator are needed. An example of the behavior of the power and correlation signals in a package detection is shown in Fig. 3.16.

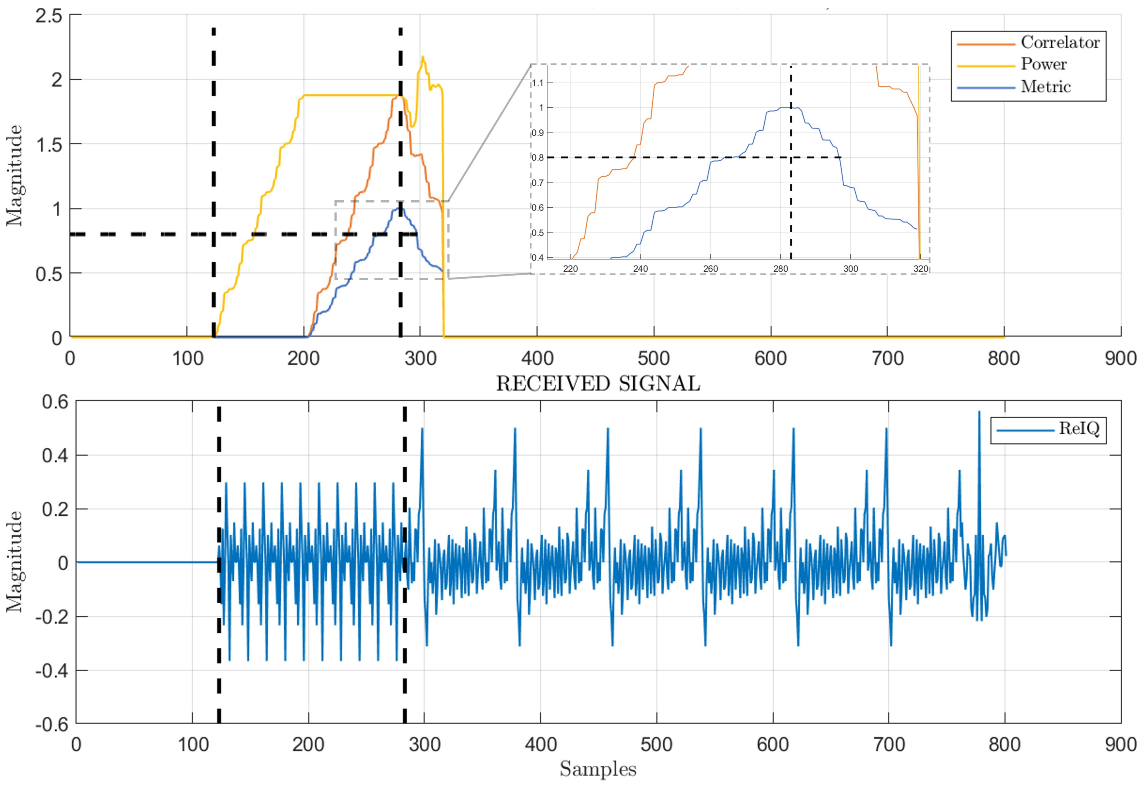

Figure 3.16: Example of the metric signal in the synchronization process of a received signal.

The inaccuracies in the signal caused by the channel can cause the correlation peak to be detected outside of the ideal sample. A control on the CP elimination process corrects the time offset by changing the number of samples removed.

Fine synchronization is achieved using (3.23). A weighted average of the first eight samples of each OFDM symbol, excluding the DC sample, is performed to obtain an average of τ. This is always done in the long preamble samples. Then an average of these samples is taken in the first three OFDM symbols, and the rest of the symbols contained in the long preamble are used to compensate for the latency of the FFT operation, since this synchronization is performed after the FFT, unlike other implementations without hermitian symmetry.

3.4.3. Proposed phase correction technique

As mentioned before, the channel-induced scattering affects the estimation of τ. We find that the receiver phase is not only affected by the SFO, but also by two channel-induced noises, called non-deterministic and deterministic noise. Thus, in [78], we propose a more accurate estimation of the phase offset of OFDM implementations on VLC channels. First, to reduce the non-deterministic noise effect, a mobile average of the pilot subcarriers is computed. The non-deterministic noise is assumed to be a AWGN with zero mean and σ^2 variance $[n_{nd} \sim \mathcal{N}(0, \sigma^2)]$, but even if the non-deterministic noise cannot be corrected, its effect can be mitigated by averaging as many samples as possible. With a sufficiently high SNR (which also depends on the modulation used), the dispersion induced by the non-deterministic noise is not enough to cause errors in the identification of the symbols. On the other hand, the deterministic noise affects all the subcarriers equally, unlike SFO which has a different effect on the subcarriers depending on its position on the symbol. Taking these noises into account, the angle difference between the transmitted and received symbols in the ith subcarrier can be defined as:

$$\Delta\beta_i = n_d + n_{nd} + \frac{2\Pi}{M} i * \tau \tag{3.27}$$

Where n_{nd} is the non-deterministic noise, and n_d is the deterministic noise which is independent of the subcarrier index $\boldsymbol{i}$. Even if the non-deterministic noise has a mean other than zero, it can be rewrited as an addition of a zero mean noise and an additional constant that represents the mean offset, as:

$$\Delta\beta_i = n_d + [n_{nd}^{mean} + n_{nd}^{\mathcal{N}(0,\sigma^2)}] + \frac{2\Pi}{M} i * \tau$$

$$\Delta\beta_i = n'_d + n_{nd} + \frac{2\Pi}{M} i * \tau \tag{3.28}$$

Where $n'_d = n_d + n_{nd}^{mean}$, being (3.28) always an equivalent of (3.27).

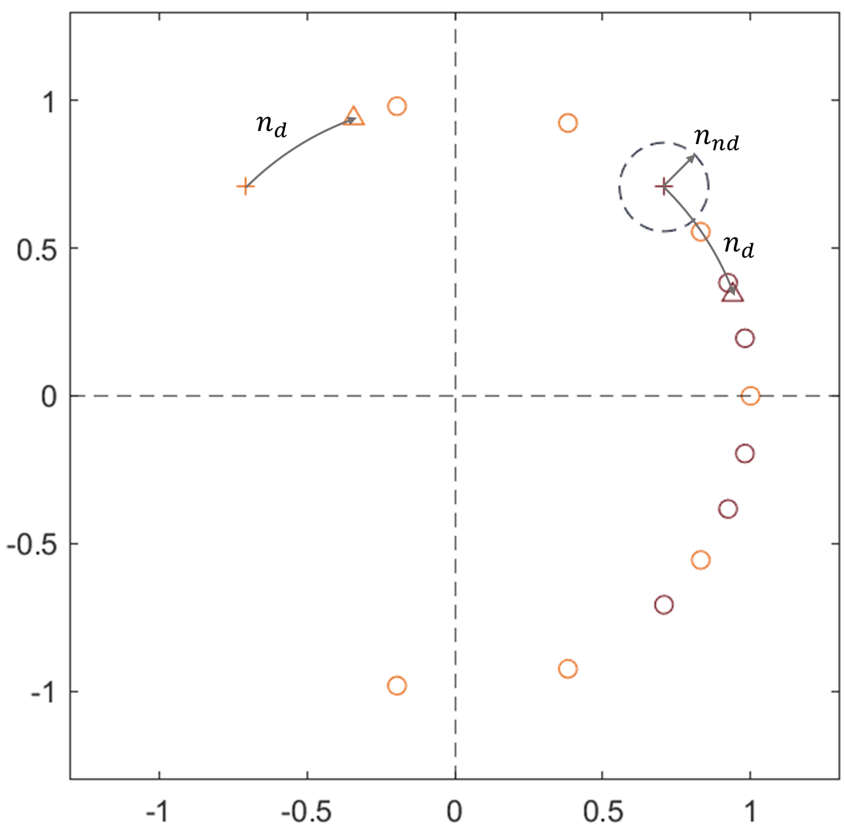

Figure 3.17: Angle error induced by non-deterministic noise, deterministic noise and sample frequency offset.

To have a better understanding of (3.27), each effect is represented in Fig. 3.17. Where $+$ is the original position of the symbol, the $\triangle$ is the deterministic noise shift, and **o** is the impact of the SFO, for offsets from one to seven.

The deterministic noise can be calculated by using any two different subcarrier angles. The angle of each one is multiplied by the position of the other, as follows:

$$i2 * \Delta\beta_{i1} = i2 * n_d + i2 * \frac{2\Pi}{64} i1 * \tau + i2 * \cancel{n_{nd1}} \approx 0 \tag{3.29}$$

$$i1 * \Delta\beta_{i2} = i1 * n_d + i1 * \frac{2\Pi}{64} i2 * \tau + i1 * \cancel{n_{nd2}} \approx 0 \tag{3.30}$$

Then both equations, (3.29) and (3.30) are subtracted to obtain the deterministic noise. Even though this proposal works for any subcarriers, as the pilots are averaged, even if the average of the 16 samples is not large enough to get to zero, the effect of the non-deterministic noise in these subcarriers can be diminished. Obtaining:

$$n_d \approx \frac{i2 * \Delta\beta_{i1} - i1 * \Delta\beta_{i2}}{i2 - i1} \tag{3.31}$$

After having a good estimation of the n_d, τ is calculated having the deterministic noise into account. To obtain a better approctimation of τ the angle of two different subcarriers following 3.27 is substracted resulting in:

$$\Delta\beta_{i1} - \Delta\beta_{i2} = \cancel{n_d} + \frac{2\Pi}{64} i1 * \tau - \cancel{n_d} + \frac{2\Pi}{64} i2 * \tau \tag{3.32}$$

$$\frac{2\Pi}{64} * \tau \approx \frac{\Delta\beta_{i1} - \Delta\beta_{i2}}{i1 - i2} \tag{3.33}$$

Then, (3.33) accomplishes the same goal as (3.23) while reducing the influence of deterministic noise on the time delay estimation.

3.5. Color shift keying

CSK is also a multicarrier modulation format, but different from OFDM, and as its name suggests, it uses the different wavelengths that make up white light (RGB) to transmit different information on each color (in parallel). Then, it is clear that this method cannot be implemented with phosphor-based LEDs. RGB LEDs, as mentioned on subsection 2.1.1, are not as widely used for lighting as the phosphor-based ones because they are expensive and complex to implement. In counterpart, the use of RGB LEDs increases the inherent bandwidth of each color. CSK modulation is then limited to the type of LED used as a transmitter. CSK is standardized in Section 12 of IEEE 802.15.7 [67].

Leaving that limitations behind, CSK symbols are mapped in the x-y chromaticity coordinates (based on the x-y chromaticity plane created by the international commission on illumination (CIE) 1931 color space [88]). The information is then transmitted by changing the intensity on each LED. To reduce flicker effects the total intensity of the RGB LED is kept constant making that $P_r + P_g + P_b = 1$, where P_r, P_g, and P_b are the intensity of each of the red, green, and blue LED, respectively [89]. In CSK the bitrate is defined by the total number of color points on the constellation.

The optical signal of the three sources is detected by a set of photodetectors that are filtered to match the wavelengths of the red, green, and blue light. In resume, the CSK channel can be defined as a three coupled IM/DD channels that can be defined as the channel gain matrix [90]:

$$H = \begin{bmatrix} h_{rr} & h_{rb} & h_{rg} \\ h_{br} & h_{bb} & h_{bg} \\ h_{gr} & h_{gb} & h_{gg} \end{bmatrix} \tag{3.34}$$

Where h_{jk} is the channel gain between the transmitter $\boldsymbol{k}$ and the receiver $\boldsymbol{j}$. Even when the gain between elements varies over time due to different factors, H

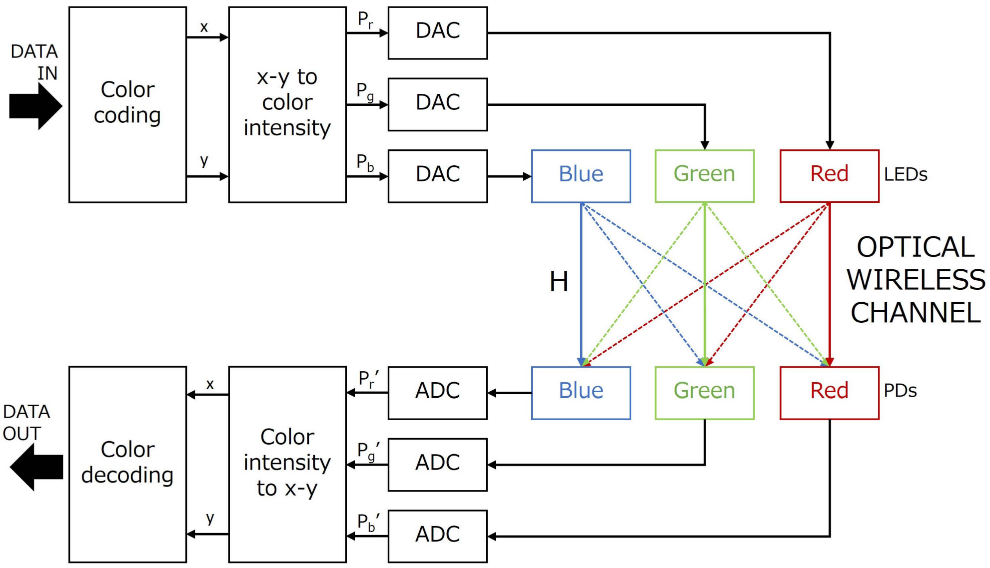

Figure 3.18: Block diagram of CSK system with a single RGB LED.

is assumed to be static. The diagonal entries h_{rr}, h_{gg}, and h_{bb} represent the ideal communication path between the color matching LED and PD, and the rest of the elements in the matrix represents the color crosstalk (interference) [91]. Then the received symbols can be defined as:

$$\begin{bmatrix} P_r \\ P_g \\ P_b \end{bmatrix} = \begin{bmatrix} h_{rr} & h_{rb} & h_{rg} \\ h_{br} & h_{bb} & h_{bg} \\ h_{gr} & h_{gb} & h_{gg} \end{bmatrix}^{-1} \begin{bmatrix} P'_r \\ P'_g \\ P'_b \end{bmatrix} + n \tag{3.35}$$

Fig. 3.18 shows the block diagram of a CSK communication system using a single RGB LED and a single pixel color sensor, with crosstalk highlighted by dotted lines. The symbols of the modulation should be a power of two to encode 2^n bits in each symbol. In the case of an RGB LED, there are only three different colors available, and to obtain a 4-CSK with it, a triangle is defined in the x-y chromaticity plane. The vertices of the triangle are defined by one of the three RGB colors, and then the fourth symbol is chosen to be a combination of the other colors, defined by:

$$\begin{aligned} x_p &= P_r \cdot x_r + P_g \cdot x_g + P_b \cdot x_b \\ y_p &= P_r \cdot y_r + P_g \cdot y_g + P_b \cdot y_b \end{aligned} \tag{3.36}$$

Where (x_p, y_p) are the coordinates of the virtual four point, and (x_r, y_r),(x_g, y_g), and (x_b, y_b) are the coordinates of each light source as shown in Fig. 3.19 Therefore, two bits can be assigned to each symbol [26].

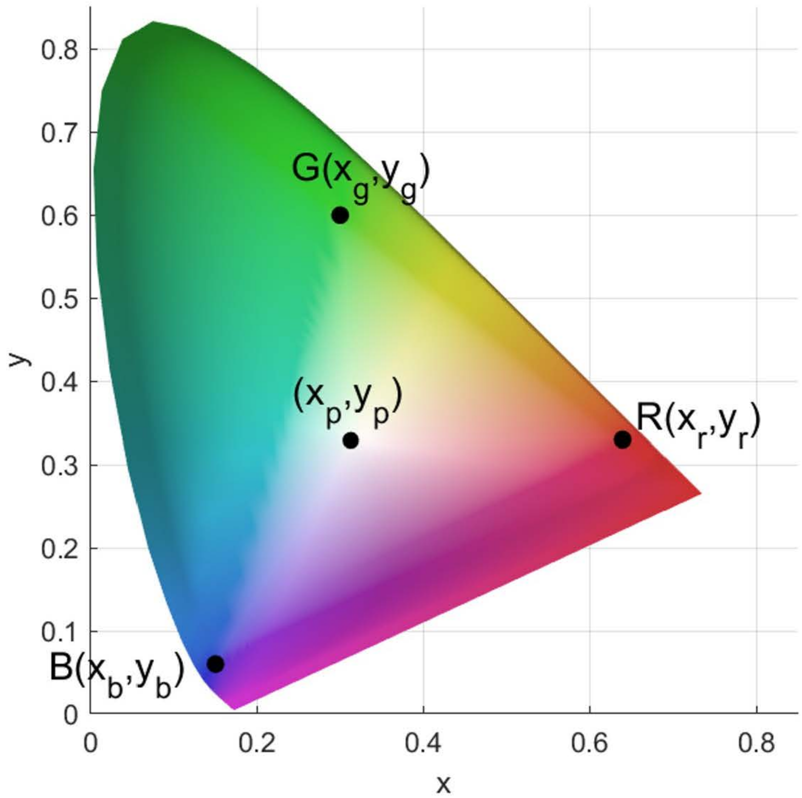

Figure 3.19: 4-CSK points on CIE 1931 x-y color coordinates.

3.6. Standards

Standardization is a key element in the communication between devices and their interconnection. Standards guarantee the adaptation of new solutions to an existing environment. In other words, they are the rules that must be followed to understand and be understood. In the case of VLC, the standardization process began in the early 00', resulting in the "Visible Light Communications Association (VLCA)" in 2014, and in 2018 VLCA became a section of the Japan Photonics Council (JPC) [92].

The IEEE has also defined a standard for VLC systems. The IEEE 802.15.7 Visible Light Communication, developed by the Task Group 7, was defined in 2011 and has undergone several modifications and updates to keep up with the latest developments in the world of visible light communications. The IEEE 802.15.7 defines three Physical Layer (PHY) types, where PHY I and PHY II consist of OOK and VPPM modulation formats and PHY III focuses mainly on CSK modulation, as it is unique to VLC systems and allows faster data rates [93]. The standard also defines a Media Access Control (MAC) layer. However, it does not consider OFDM modulations.

Another standardization group for optical wireless communications also from the IEEE is the IEEE 802.11bb Task Group, created in 2018 intending to redefine the

IEEE 802.11 to apply it to VLC [94]. The amendments to the IEEE 802.11 standard are still ongoing.

On the other hand, the recommendation ITU-T G.9991 was created by the International Telecommunication Union (ITU) [95]. It was approved in 2019 to lay the foundations for the growth of VLC systems and specifies the system architecture, PHY layer, and Data Link Layer (DLL) for high-speed indoor optical wireless communication transceivers using visible light.

There are also some Japanese standards from the Japan Electronics and Information Technology Industries Association (JEITA). The JEITA CP-1221 covers the basics of VLC systems and defines the minimum requirements to prevent interference between different optical communication devices. In addition, the JEITA CP-1222 defines a standard for visible light identification systems using 4-PPM modulation. Finally, the JEITA CP-1223 specifies a single directional VLC beacon, aiming to establish a unified standard for lower communication layers also using PPM modulation format [96].

3.7. Conclusions

The modulation format defined for the application must be chosen primarily as a trade-off between system complexity and cost and bitrate. Modulations such as OOK and VPPM are easy to implement and can also achieve high data rates but are more susceptible to ISI induced by the channel bandwidth and multipath reflections. These types of modulations can also be implemented with less hardware compared to multi-carrier modulations, and the associated algorithms responsible for encoding/decoding are also smaller and simpler, allowing implementation in smaller and low-cost microcontrollers. With OOK modulation, the NRZ implementation can handle higher bit rates than RZ, but the light intensity may be affected if multiple zeros or ones are transmitted together. In this case, bit encodings such as 4b6b or 8b10b provide DC balance. In most cases, because of its simplicity, efficiency, and reliability, the NRZ OOK is preferred when sending binary data over an optical channel.

On the other hand, OFDM modulation must be adapted to OWC channels. The use of a LED as a transceiver requires that the modulated signal be real and unipolar (positive). To achieve a real signal, the hermitian symmetry property of the FFT is used, which reduces the number of available subcarriers by half but does not require any additional hardware to achieve a real signal at the output of the IFFT. The VLC channel presents peculiarities in the estimation and correction of the received symbols. Therefore, we have proposed a time synchronization algorithm that includes a post-FFT synchronization stage to achieve time synchronization with one sample accuracy. The algorithm uses the CP elimination stage to perform the time correction. We also propose a better way to estimate the phase offset induced by the channel and the SFO. The symbol phase was found to be affected by three major shifts, the non-deterministic noise, the deterministic noise, and the one induced by the clock differences. The OFDM implementation requires a digital part capable of performing the FFT and IFFT faster enough. It also requires the use of ADCs and DACs. These add complexity to the analog design.

Finally, CSK is a multicarrier modulation unique to VLC. The limitation of this implementation is that it can only be performed with RGB LEDs, which are not as widely used as the phosphor-based white LEDs. Also, as the modulation must control each of the three LEDs independently it multiply by three the number of ellements required for the communication, making the related hardware of this kind of modulation bigger and expensier. In contrast, the dynamics of the RGB LEDs is faster than the phosphor layer, and therefore the available bandwidth of each LED is higher so that CSK based solutions could reach high transmission speeds.

4 Intelligent Reflecting Surfaces for Optical Wireless Communications

The VLC communication channel, in most cases, requires a LoS link. The necessity of a LoS link can be expanded to all kind of OWCs. This requirement limits the flexibility of the solutions in an environment where the RX devices are going to be in motion and not always in a position where are reachable in a LoS path or there is a direct blockage in the TX-RX line. To overcome this, various solutions have been explored over the years, mostly focusing on the capabilities of channel modeling [97, 98] for different scenarios or the maximum SNR that can be achieved in the non-LoS paths. Thus, the detection and decoding of the message on the receiver side become more complex and difficult to implement [99]. However, non-LoS signals in indoor environments are weak in their average strength because they are reflected randomly, and their spatial distribution is almost isotropic. In fact, in most cases, the effect of the reflected signals is neglected in the receiver signal estimation [100].

The non-LoS channel relies on many different factors that depend not only on the communication system (transmission power, transmitter/receiver device, distance between TX and RX) but also on the environment, e.g., the reflection coefficient of the surrounding surfaces or the distance of these surfaces to TX and RX. In this way, researchers have found in reconfigurable surfaces or IRSs, an alternative to configure the wireless channel. The IRSs allows to increase in the non-LoS performance of the communication system in terms of SNR, energy efficiency (as a part of the transmitted energy can be redirected and focused towards the receiver), and link reliability [100]. IRSs can be divided into two classes, one based on specular reflection (mirror-based surfaces) and others that can manipulate the electromagnetic wave in terms of amplitude and phase (meta-surfaces) [101].

Mirrors have been with us for a long time and have been used (even in ancient times) to reflect incident light to a desired location. Mirrors can only provide specular reflection with the advantage of low scattering. Therefore, to reflect the incident beam to the desired point, the angle of incidence must change, which can be translated to a change in the surface angle. That is, to deflect light, the mirror must

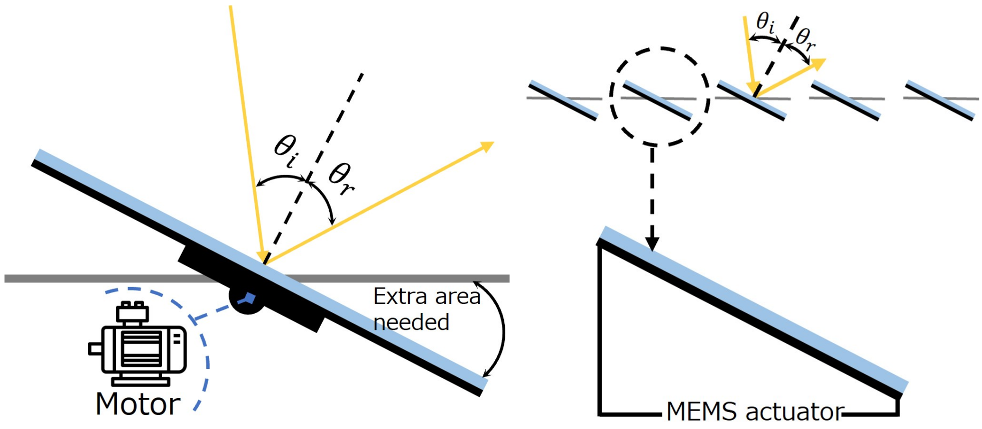

(a) Standard mirrors (b) Micro-mirrors

Figure 4.1: Mirror based IRSs

be mechanically reoriented [102]. Mirrors can be divided into two main groups, standard mirrors, and micro-mirrors, as shown in Fig. 4.1.

In the former case, a wide range of angles can be achieved by adjusting the mirrors with mechanical rotation elements. However, in cases where the amount of light to be reflected requires a large surface mirror, many problems arise, such as the necessity of a large area to be reoriented and bulky (high power-consuming) motors, which limit the deployment [103]. The second group is a combination of Micro-electromechanical systems (MEMSs) devices and optics known as Micro-opto-electromechanical systems (MOEMSs). The MEMSs can act as the actuators and support for the micromirrors, and the area of the entire device can be scaled by adding or removing cells. Since the changes can be made on each MOEMS, the IRS is kept flat at the macroscopic level, regardless of the desired angle. Another interesting aspect is that the independence of each element allows performing not only specular reflection but also focusing, splitting, and collimation functionalities [104].

Meta-surfaces, on the other hand, are two-dimensional metamaterials composed of subwavelength metallic or dielectric structures (Fig. 4.2). The combination of the materials and structures can manipulate the amplitude, phase, and polarization of the incident light to obtain the desired reflection using structural engineering. This type of IRSs allows reflections where the reflected angle is different from the incident angle and even out-of-plane reflections, known as anomalous reflections. This can be performed because of the meta-surface capacity to modify the phase of the incident light, and then create a new wavefront in the desired direction [105]. Same as in micro-mirrors, each element of the metasurface can be configured independently, in this case, not only by a mechanical stimulus but also electrical, thermal, or optical. Even more, meta-surfaces allow the control of different wavelengths, which means that the modulation for multiple users can be done on different wavelengths without interfering with one to another [100].

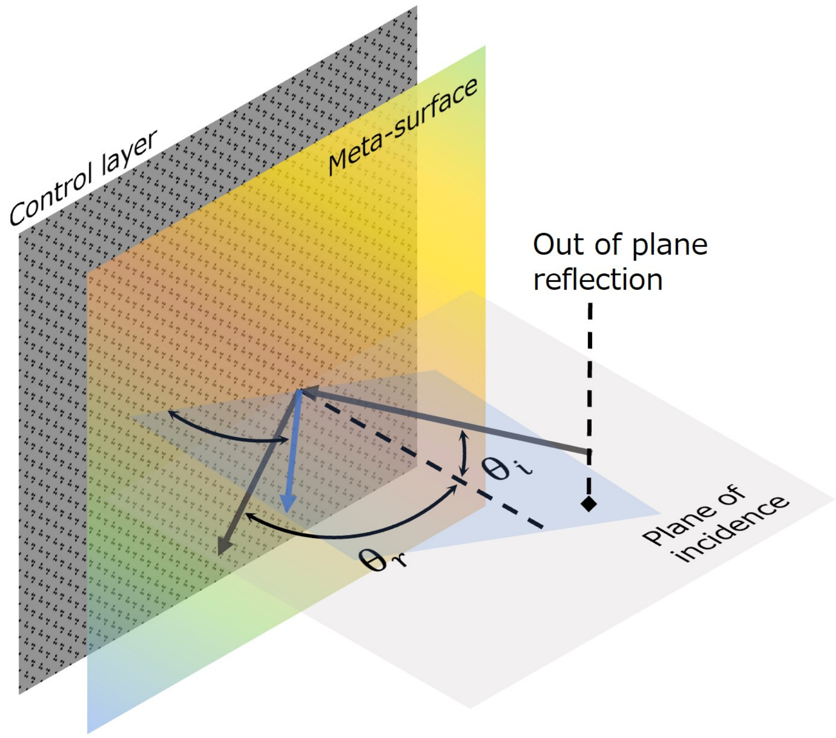

Figure 4.2: Configurable meta-surface based IRSs

4.1. Channel Model

In this section, we analyze the channel model of a micro-mirror based IRS for a FSO link. The parameters of the IRS, such as power density distribution and power efficiency, are evaluated in terms of physical parameters such as orientation, position, and size. The channel of the link is also modeled to account for the geometric and misalignment losses that can occur in long-distance links typical of FSO. We assume that the LoS link between TX and RX is not available, and therefore the communication can only be achieved by using an IRS.

In general, when Light amplification by stimulated emission of radiations (LASERs) are used, the light generated can be assumed to be a Gaussian beam [106,107], which means that the power density distribution over a line perpendicular to the propagation direction has a Gaussian profile. The Gaussian beam traveling in the +z direction can be defined as [108]:

$$E(\mathbf{z}, \mathbf{r}) = E_0 \frac{w_0}{w(z)} \cdot exp\left(-\frac{r^2}{w_x^2(z)}\right) exp\left(-j\phi(\mathbf{z}, \mathbf{r})\right) \tag{4.1}$$

with phase

$$\phi(\mathbf{z}, \mathbf{r}) = kz + k\frac{r^2}{2R(z)} - \psi(z) \tag{4.2}$$

Where E_0 is the energy at origin, $k = 2\pi/\lambda$ is the wave number, and $R(z)$ is the curvature of the wavefront given by:

$$R(\mathbf{z}) = z\left(1 + \left(\frac{z_R}{z}\right)^2\right) + k - \psi(z) \tag{4.3}$$

Also, $w(z)$ is the beamwidth at any distance z:

$$w(\mathbf{z}) = w_0\sqrt{1 + \left(\frac{z_R}{z}\right)^2} \tag{4.4}$$

Being $z_R = \pi w_0^2/\lambda$ the Rayleigh length, and $\psi(z) = tan^-1(z/z_R)$. In this application, the quality factor of the beam is assumed to be one, so no loss in the emitter is considered. More context of the exposed parameters is given in Fig 4.3.

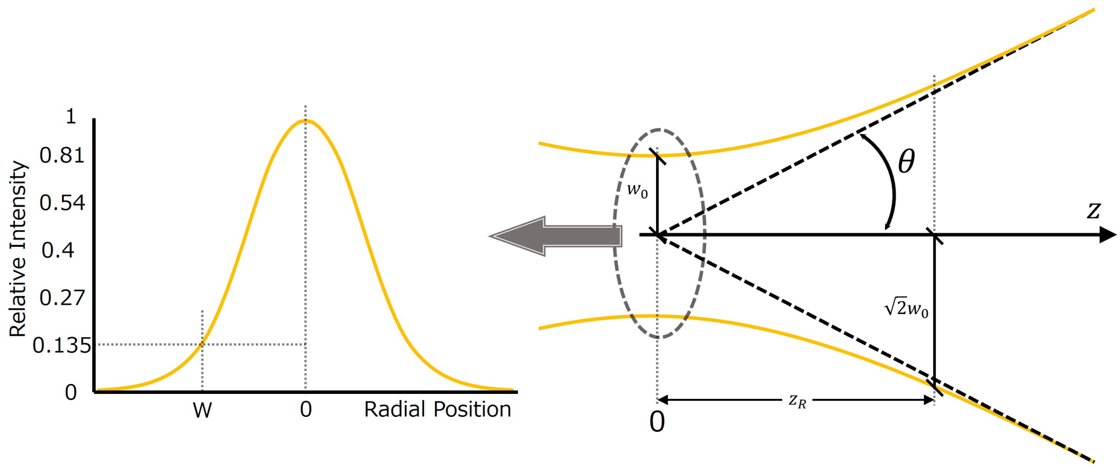

Figure 4.3: Gaussian beam main parameters: beam waist (w_0), Rayleigh range (z_R), and divergence angle (θ)

An approximation of the beamwidth at distances $z \gg z_0$ can be fitted to the half angle θ, where $\theta = \lambda/\pi w_0$. From this equation, it can be deduced that the smaller the waist at the origin (w_0), the higher the divergence and the less directional the beam. For surface emitting LEDs, as mentioned on subsection 2.1.1, the generated light fits a Lambertian pattern, and therefore it is not convenient to use the Gaussian distribution for a light source other than a LASER.

Continuing with the Gaussian beam characteristics, the optical intensity of a given Gaussian beam is the square of the energy magnitude and is a function of the distance and radial position, d and $r = \sqrt{x^2 + y^2}$ and follows [24]:

$$I(\mathbf{d}, \mathbf{r}) = \left|E(\mathbf{d}, \mathbf{r})^2\right| = \frac{2}{\pi\omega^2(d)} exp\left(-\frac{2 \cdot r^2}{\omega^2(d)}\right) \tag{4.5}$$

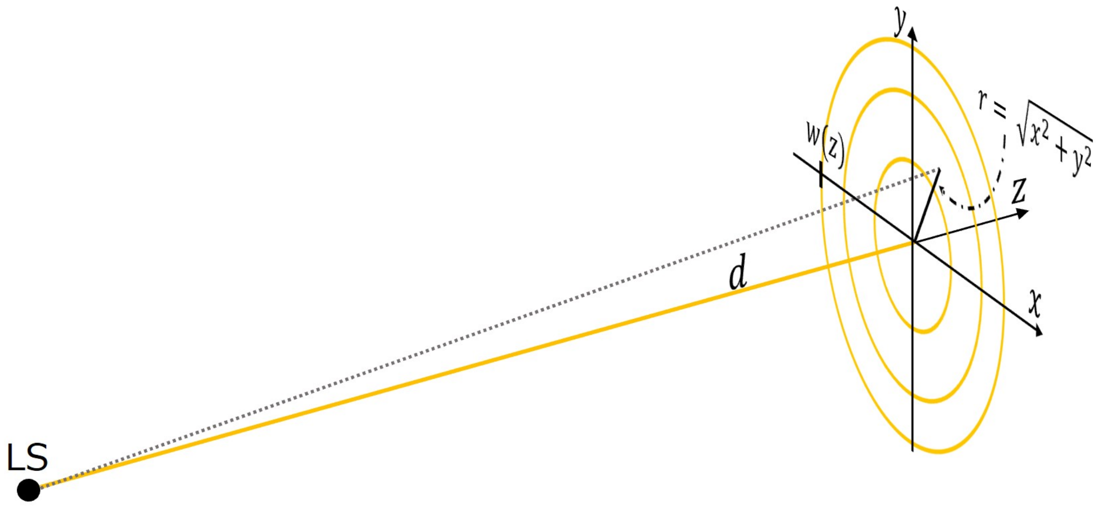

Figure 4.4: Power intensity at a distance d and a radius r from the beam center.

As the maximum intensity is reached at the center of the beam ($r = 0$), then from (4.5) it can be deduced that $I_{max}(d) = 2/\pi\omega^2(d)$.

On the other hand, the received signal at the PD can be modeled as $y[\mathbf{t}] = h \cdot S[\mathbf{t}] + w[\mathbf{t}]$. Where $w[\mathbf{t}] \in \mathbb{R}$ represents the AWGN with zero mean and variance σ^2, $S[\mathbf{t}] \in \mathbb{R}^+$ is the transmitted intensity modulated symbol, and $h \in \mathbb{R}^+$ is the end-to-end channel gain. For the channel model $\mathbf{h}$ we follow the one suggested in [109, 110]:

$$h = h_p h_a h_g \tag{4.6}$$

Where the FSO channel is affected mainly by three factors. h_p represents the atmospheric loss, which is deterministic and follows $\mathbf{h_p} = 10\ exp\left(-\frac{k}{10} d_{total}\right)$, where $\mathbf{d_{total}}$ is the addition of the distance from the TX to the IRS and the distance from the IRS to the RX, and $\mathbf{k}$ is the the attenuation coefficient. $\mathbf{h_a}$, on the other hand, is a random variable that represents the atmospheric turbulence induced by changes in temperature and pressure along the channel. Finally, $\mathbf{h_g}$ represents the fraction of the power reflected on the IRS and collected in the RX lens:

$$h = \int_{\mathcal{A}} I_{ref}(\mathbf{d}, \mathbf{r}) d\mathcal{A} \tag{4.7}$$

Where $\mathcal{A}$ is the area of the Rx lens. Furthermore, the relative position and orientation of the TX with respect to the IRS affect the power distribution reflected. Additionally, the size of the IRS and its position with respect to the RX lens determines the quantity of reflected power that is finally collected by the PD.

4.1.1. Specific proposed system to study

The evaluated system is shown in Fig. 4.5, where the origin of the coordinate system is located at the point where the center of the light beam reaches the surface of the IRS. The IRS is then at a height ($y = 0$), and each mirror has its center at $(x_m, 0)$ and an angle of θ_m. The light source is at (x_l, y_l), and the center of the Rx lens is at (x_p, y_p) with an angle to the **x** axis (ϕ_p) and an area of $2a_p$. Maximum power is received when the Rx mirror is perpendicular to the reflected beam ($\phi_p = -\theta_l + 2\theta_m - \theta_p$), where θ_l and θ_p are the angle formed by the TX and **x** axis, and the angle formed by the RX lens and **x** axis, respectively.

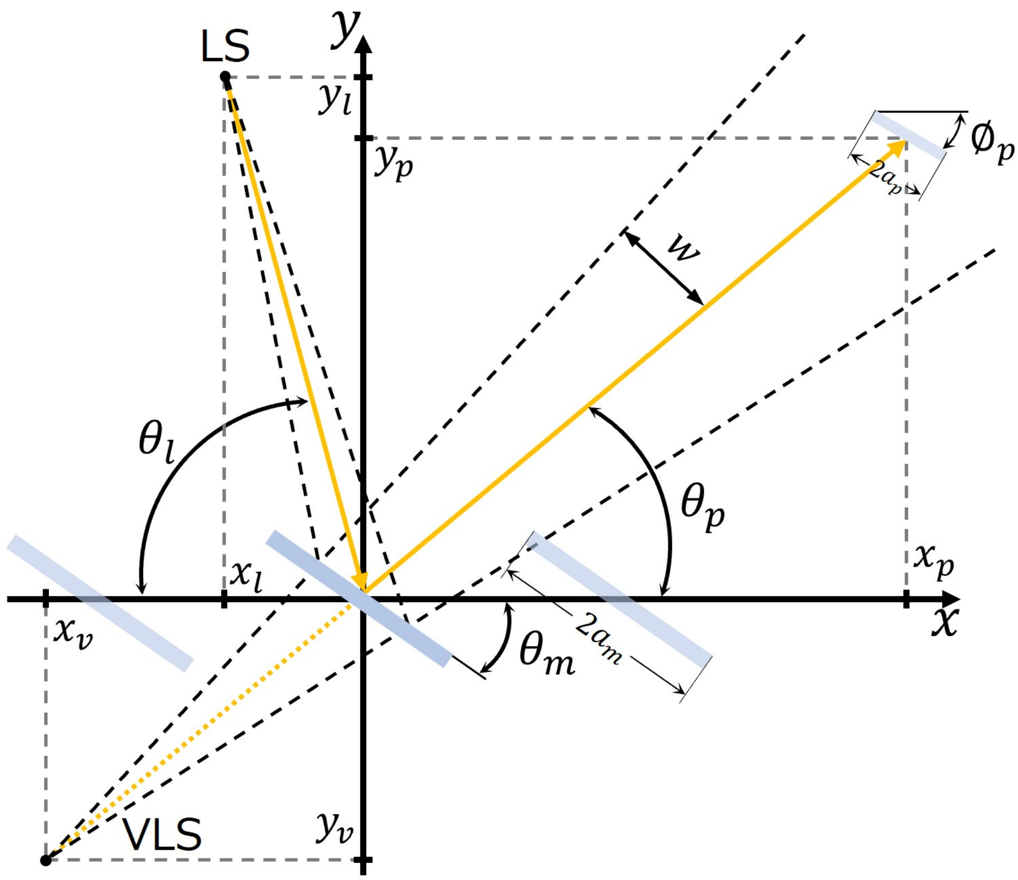

Figure 4.5: Structure of micro-mirror IRS-assisted optical wireless communication system.

The effect of the mirror in the system can be replaced by substituting the light source with an equivalent "virtual" one (**VLS** in Fig. 4.5). This feature simplifies the system analysis and will be used in the following analysis.

The VLS have an angle of $\theta_l - 2\theta_m$ with respect to the **x** axis, and knowing that $(x_l, y_l) = (-cos(\theta_l) \cdot d_l, sin(\theta_l) \cdot d_l)$ the position of the VLS is then:

$$(x_v, y_v) = (-x_l \cdot cos(2\theta_m) - y_l \cdot sin(2\theta_m), -y_l \cdot cos(2\theta_m) + x_l \cdot sin(2\theta_m)) \quad (4.8)$$

4.1.2. Model of the power distribution at the RX

Since the mirrors used in the IRS are of finite size, the VLS beam projected onto the RX is limited to the mirror area. Therefore, (4.5) is limited, and the reflected power outside the micro-mirror is considered to be zero, following:

$$I_{ref}(\mathbf{d},\mathbf{r}) = \begin{cases} I(\mathbf{d},\mathbf{r}), & r \in \mathcal{C} \\ 0, & \text{otherwise} \end{cases} \tag{4.9}$$

Where $\mathcal{C} = \{(x,y)|m_1 \cdot (x - x_v) + y_v \leq y \leq m_2 \cdot (x - x_v) + y_v\}$, being

$$\begin{aligned} m_1 &= \frac{y_v - sin(\theta_m)a_m}{x_v + cos(\theta_m)a_m - x_m} \\ m_2 &= \frac{y_v + sin(\theta_m)a_m}{x_v - cos(\theta_m)a_m - x_m} \end{aligned} \tag{4.10}$$

The maximum reflected power (I_{ref}^{max}) is reached when ($\theta_m = \theta_l - \frac{\pi}{2}$), which is useless in our case because the reflected beam will overlap the incident one. Rotating the mirror to focus the beam into the RX creates a smaller reflecting area as shown in Fig. 4.6. The reflected power is then given by ($I_{ref}^{max} \cdot cos(\frac{\pi}{2} + \theta_m - \theta_l)$).

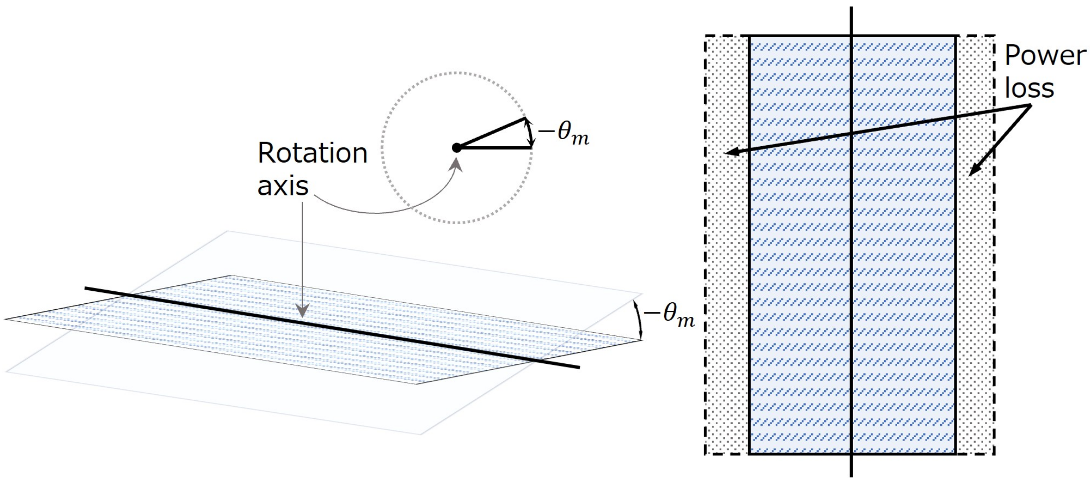

Figure 4.6: Effect of the mirror angle on the effective reflecting area

After having the reflected power, the total power collected at the receiver lens is obtained by (4.7), then:

$$h = sin(\Psi) \int_{\mathcal{A}} I_{ref}(d, sin(\Psi) \cdot r) d\mathcal{A} \tag{4.11}$$

Where $\mathcal{A}$ is the area of the RX lens and $\Psi = -\theta_l + 2\theta_m - \theta_p$, being $sin(\Psi)$ the power losses due to the non-orthogonality of the receiver lens. Assuming that the beam distance ($\mathbf{d}$) is the addition of the TX distance and the RX lens distance

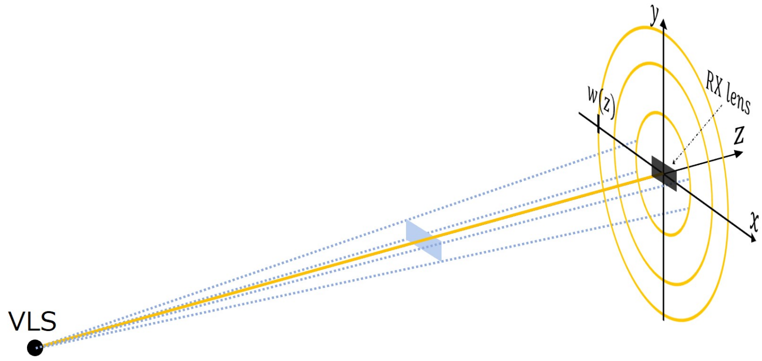

(a) Projection of mirror and lens

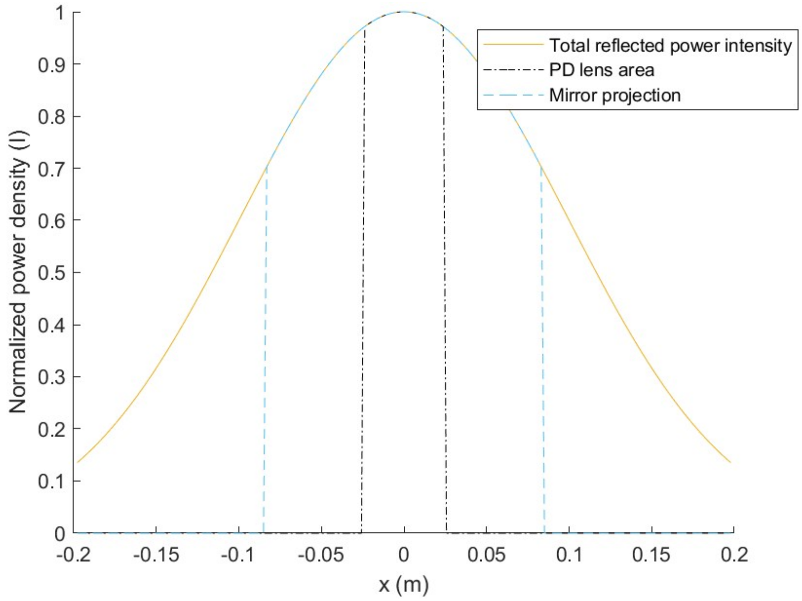

(b) Power intensity

Figure 4.7: Power distribution at the total link distance

regarding the IRS, then $d_{total} = \sqrt{(x_p - x_v)^2 + (y_p - y_v)^2}$. By substituting (4.9) in (4.11) under the condition that $a_p \ll d_{total}$ we obtain:

$$\frac{2sin(\Psi)}{\pi\omega^2(d_{total})} \int_{l_i}^{l_r} exp\left(-\left(\frac{\sqrt{2}\cdot sin(\Psi)}{\omega(d_{total})}\cdot r\right)^2\right)\mathbf{dr} \tag{4.12}$$

This condition is always satisfied for FSO applications because the mirrors have sizes around tens of millimeters [111], and the distances between TX, RX, and IRS are typically in the order of hundreds of meters to kilometers. By using the error function equivalent $erf(p\cdot a) = \frac{2}{\sqrt{\pi}} \cdot p \int_0^a exp\left(-(p\cdot t)^2\right)\mathbf{dt}$ [112] we can reformulate (4.12) for the area from 0 to l_r as:

$$\frac{1}{\sqrt{2\pi}\omega(d_{total})}\left(\frac{2}{\sqrt{\pi}}\frac{\sqrt{2}\cdot sin(\Psi)}{\omega(d_{total})}\right)\int_0^{l_r} exp\left(-\left(\frac{\sqrt{2}\cdot sin(\Psi)}{\omega(d_{total})}\cdot r\right)^2\right)\mathbf{dr}$$

$$= \frac{1}{\sqrt{2\pi}\omega(d_{total})} \cdot erf\left(\frac{\sqrt{2}\cdot sin(\Psi)}{\omega(d_{total})}\cdot l_r\right) \tag{4.13}$$

For the total lens area we finally obtain:

$$h = \frac{1}{\sqrt{2*\pi}\cdot w(d_{total})} \cdot \left| erf(\frac{\sqrt{2}\cdot sin(\phi_p)}{w(d_{total})}\cdot l_r) - erf(\frac{\sqrt{2}\cdot sin(\phi_p)}{w(d_{total})}\cdot l_i)\right| \tag{4.14}$$

Where l_r and l_i are the integration zone at the Rx lens. These values are the limits where the power intensity is effective, and therefore the beam waist ($w(d)$), the projection of the mirror, and the lens area (a_p) at d_{total} are compared in the plane orthogonal to the reflected beam to select the smaller one, which is going to be the one that limits the received power (Fig. 4.7). For multiple micro-mirrors in an IRS, (4.11) can be rewrited as:

$$h = sin(\Psi)\int_{\mathcal{A}} \sum_{m=1}^{M} I_{ref}^{m}(d, sin(\Psi)\cdot r)d\mathcal{A} \tag{4.15}$$

4.1.3. Results and discussion

Table 4.1: System simulation parameters

	Symbol	Value
Wavelength	λ	1550 nm
Beam waist radius	w_0	1 mm
Electric field at origin	λ	60 kV/m
IRS size	L_x	2 m
LS location	(x_l, y_l)	(866 m,500 m)
Lens location	(x_p, y_p)	(300 m,600 m)
Lens radius	a_p	20 cm
Lens angle	ϕ_p	$\frac{\pi}{2}$ rad
μ-mirror radius	a_m	1 cm
μ-mirror location	(x_m, y_m)	(0,0)
Gap between μ-mirror	m_{gap}	1 cm

The IRS model given in (4.15) accounts for the fraction of the transmitted power that is effectively received at the detector. The power distribution of the light source significantly changes the misalignment effect at the receiver side. From the Gaussian beam distribution, it can be seen that the maximum power of the beam travels in the center. Therefore, a movement of this beam with respect to the center of the lens will result in a significant power loss, different from the slight power loss that would be seen if the wavefront were planar. On the other hand, the reflected beam,

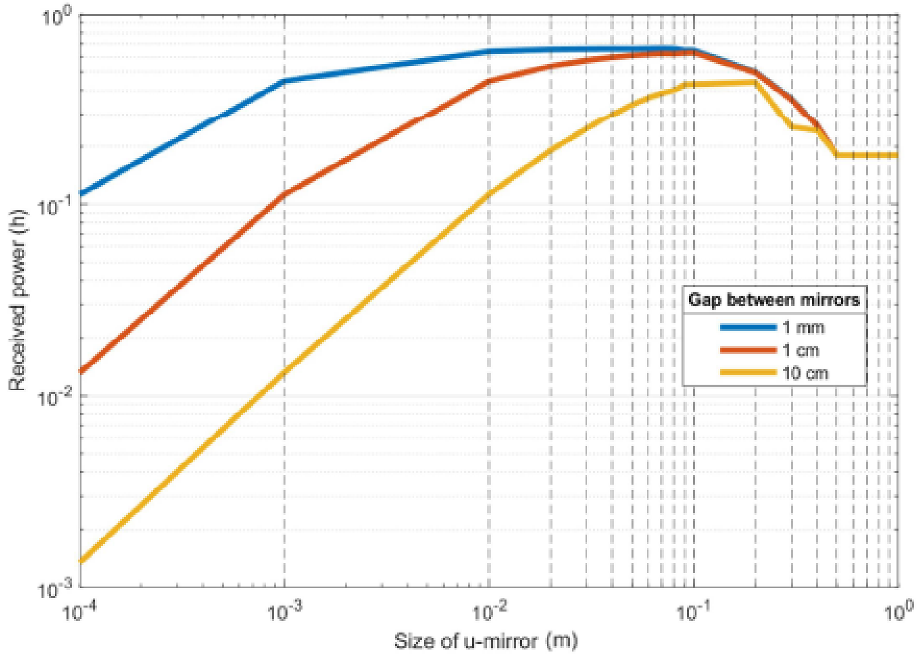

Figure 4.8: Simulation of the evolution of the received power whit respect to the size of each micro-mirror.

even if perfectly aligned with the center of the lens, will have a loss due to the angle of the mirror with respect to the incident beam that cannot be resolved.

We then perform simulations of the system with the parameters shown in Table 4.1. First, the effect of the size and distribution of the micro-mirror elements is evaluated. Fig. 4.8 shows the evolution of the total power at the receiver as the size and number of mirrors are varied, while the total size of the IRS remains the same. The evolution of the power presents a very interesting behavior, which is that the maximum power at the lens is not reached with the larger mirror size. This can be explained because if the mirrors have a size comparable with the IRS the maximum quantity of mirrors that can be allocated will be one. On the other hand, as there are more mirrors in the IRS, it can focus the beam by changing each mirror angle (θ_m) to target the center of the lens (focusing), increasing the total energy collected. Also, as the mirrors become smaller, the gap between them begins to have more impact on the total power that can be reflected, and as each mirror have a power loss area, as shown in Fig. 4.6, the effective reflecting surface is reduced. The size of the receiver lens also affects the size of the micro-mirrors in which the received power is maximum.

Second, since the incident beam has a limited width, there is a point at which increasing the area of the IRS will not improve the reflected energy. Furthermore, the total area received at the IRS is affected not only by the beam width at the light source distance (4.4) but also by the angle of the light source with respect to the IRS.

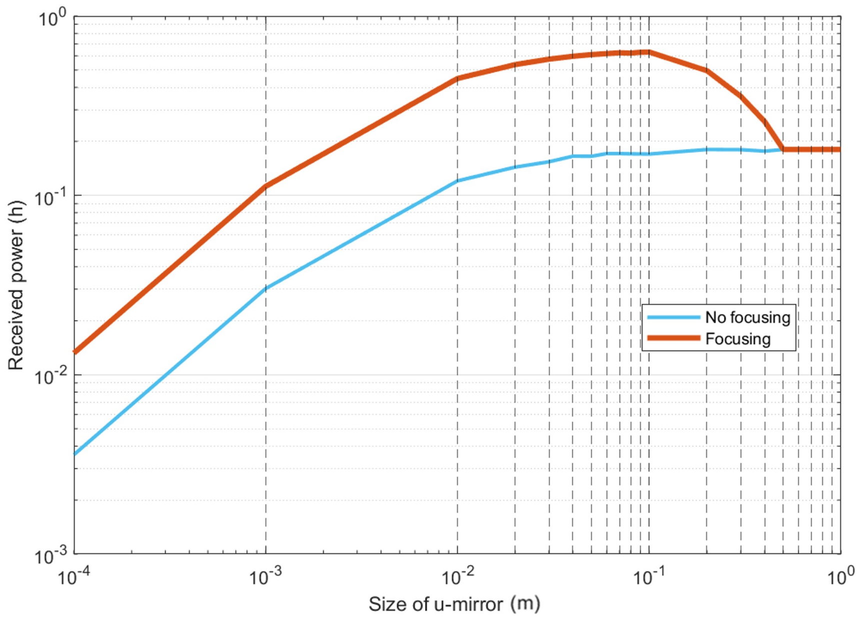

(a) Received power vs. micro-mirrors size and number

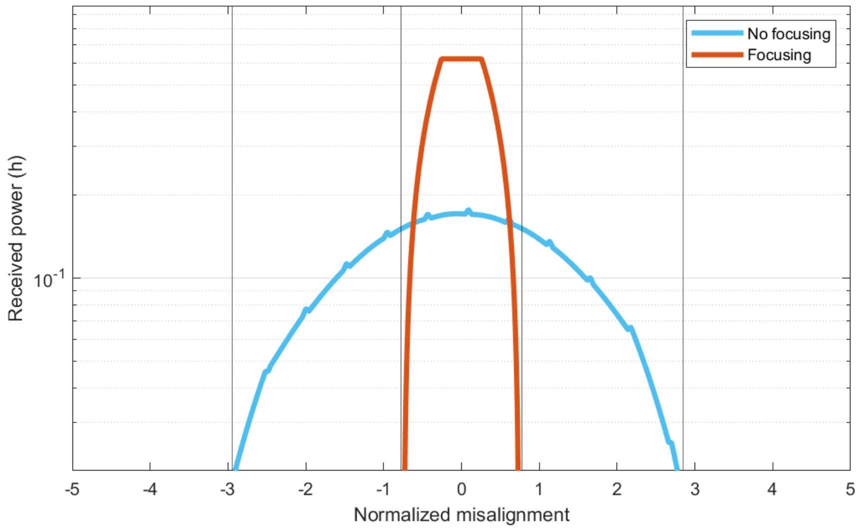

(b) Received power vs. normalized misalignment of the lens

Figure 4.9: Impact of focus or not the beam into the lens by using the micro-mirrors tilt angle.

Fig. 4.9 shows the effect of focusing or not focusing the beam into the lens, in this case for a mirror gap of 1 cm. When not focused, all the micro-mirrors are tilted by the angle ($\theta_m = \frac{tan^{-1}(y_l/x_l) - tan^{-1}(y_p/x_p)}{2}$). It is important to clarify that the smaller the micro-mirrors, the more precise the angle control of each micro-mirror must be. For a IRS of 2 m, eleven mirrors with a radius of 8 cm and a distance between them of 1 cm can be assigned. In this case, the tilt angle precision of each element must be at least $\frac{\pi}{32}$. Also, when the beam is not focused, as mentioned earlier, the total power received in ideal conditions is less compared to the focused beam, but it is more resilient to misalignment effects induced by the displacement of the RX lens or IRS.

5 VLC Prototype: Design and System Implementation

"Information is not knowledge. The only source of knowledge is experience. You need experience to gain wisdom."

Albert Einstein

VLC, is rapidly evolving to help with last-mile communications. This has motivated researchers to propose new approaches that can be affordable and useful in our daily lives. In recent years, VLC applications have been developed for various purposes, such as indoor communications [14, 113], vehicle communications [114], underwater applications [115], aircraft cockpits [116], among other multiple indoor and outdoor solutions. Besides, the market around VLC is also developing and offers unique opportunities to explore different lines of applications.

As a first approach to a cheap, small, and portable VLC system, we propose a prototype for both transmitter and receiver that can be an actual working VLC link, flexible enough to run different end applications.

In this chapter, we will take you through the journey from the initial conceptual design to the final implemented system to get a clear picture of the capabilities and limitations of the prototype.

5.1. Conceptual design

The first goal of the system is to demonstrate that a low-cost VLC solution can cover multiple applications, thus reducing the need for RF solutions. This prototype aims to build a system as a whole, designing and implementing the hardware, low-level logic, and software to demonstrate the data flow of a VLC solution and the opportunities and challenges faced at each stage.

In the early stages of design, the characteristics of the final solution must be made clear. Therefore, the "must have" requirements are listed below:

- An affordable VLC RX. This means that the final RX must have the lowest cost that can be achieved without compromising the main features.
- A low-power portable VLC receiver. As seen in other applications, the main drawback of the VLC receiver is that it requires a LoS channel with the transmitter. Therefore, creating a portable wireless VLC receiver brings flexibility to the final solution, allowing one to place or attach the RX on any surface to maximize the LoS signal.
- A flat and small VLC receiver. The miniaturization of the RX makes it easier for the user to adopt the solution. On the other hand, most of the deployments require a flat surface to mantain the device in limits.
- A flexible user application. Since the prototype is intended to support multiple final applications, the user interface must allow configuration of the behavior that each transmitter triggers in the application.
- An affordable VLC TX. Following the same concept as RX, it is desired to have a cheap solution that can be easily deployed.
- A low-power transmitter. The main applications of this prototype are for indoor use, e.g., an office building, a museum, or a train. Thus, the lights are close to the end user (from a few tens of centimeters to about two meters). For this purpose, the required lighting has a low light output, which refers to LEDs with a power of around 2 or 3 watts.

Following these specifications, the hardware of the prototype is described in the following section.

5.2. Hardware implementation

The solution in terms of hardware can be divided into two big blocks, the transmitter (TX) and the receiver (RX).

5.2.1. Transmitter

To start with the hardware involved in the transmitter, we first need to know the characteristics of the LED since it plays a main role in data transmission. To do this, we start looking for a candidate that can be used in our solution. The LED parameters we were looking for are: Power consumption around 1W, small size, and white light emission (as it will be used for both illumination and communication purposes).

The LED could also be an RGB LED since multiple works show that this type of LEDs can offer a higher bandwidth by using each color as a different channel

[117, 118]. However, our prototype prioritizes the cost and size of the transmitter, which is significantly affected by the need for three drivers (one for each color). In addition, white LEDs have a higher CRI than RGB LEDs, indicating that white LEDs produce better quality light for color accuracy. Therefore, it is better to use white LEDs over RGB LEDs in applications where color accuracy is important, such as art studios, museums, and retail lighting.

On the other hand, the optimal lighting level for indoor illumination varies depending on the space and its function. For example, in a living room or bedroom, the recommended range is between 50-300 lux for general lighting and up to 1000 lux for task lighting. In a dining or conference room, the recommended range is between 150-300 lux. In an art gallery or museum, the range should be between 50-150 lux to protect the artwork [119]. In this way, the relatively low power consumption of the LED makes it suitable for several indoor purposes, and it is easier to scale up the prototype by adding LEDs to achieve higher distances.

Therefore, the chosen LED was the LED LUW CN7N ultra white from OSRAM, which offers a cold light being the yellow component half of the blue one (Fig. 5.1) [120].

As mentioned in subsection 2.1.1, the phosphor layer of the white LEDs has a slow time response, which limits the transmission bandwidth. Therefore, we have tested several LEDs with different color temperatures and have found that cooler LEDs have a higher bandwidth compared to warmer LEDs, with the bandwidth of the warm LEDs being about 1 MHz and the bandwidth of the cool LEDs being

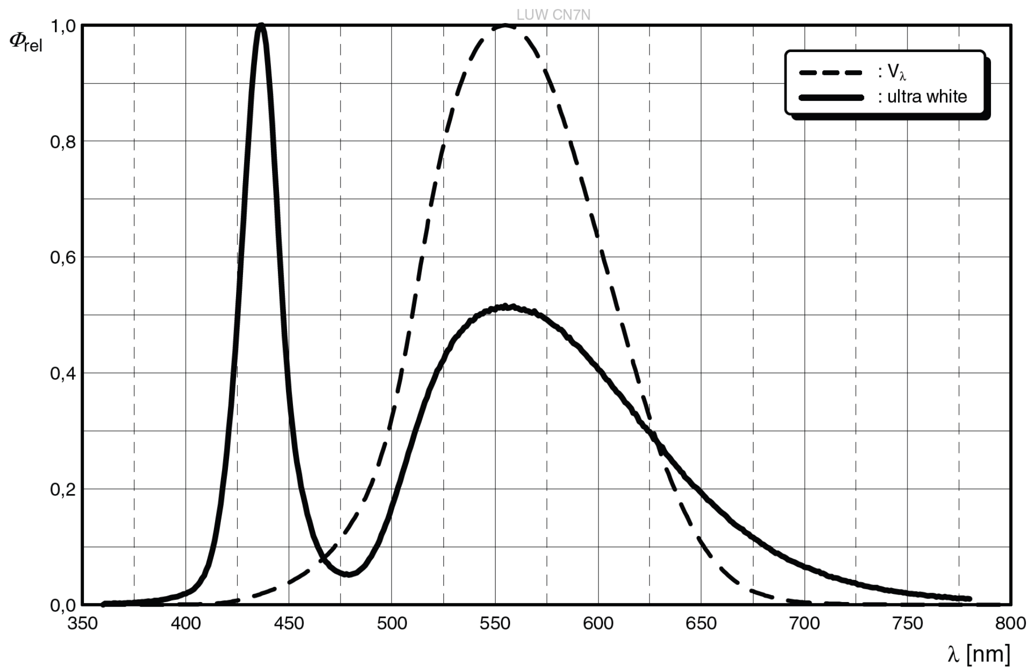

Figure 5.1: Relative spectral emission at TS = 25 °C.

Table 5.1: Comparison between LEDs used in the TX.

	LUW CN7N [120]	LUW H9GP [121]
Color temperature (K)	6160	6500
Forward Current (mA)	100 (min)	100 (min)
	500 (max)	1000 (max)
Half-power angle (°)	80	90
Forward Voltage (V)	2.9 (min)	2.75 (min)
	3.8 (max)	3.75 (max)
Luminous Flux (lm)	71 to 150	82 to 150
Price(€) [2]	2.82	2.89

about 1.5 MHz [1]. This supports the choice of LUW CN7N, as the chosen LED must have low radiation in the yellow component.

Continuing with the LED characteristics, it has a half-power angle of 80° and a maximum luminous flux of 112 lm. In terms of electrical characteristics, it can be driven with currents from 100 mA to 500 mA, with a voltage range from 3.1 to 3.5 V. However, when it comes to knowing the dynamic behavior of the LED, everything becomes blurry. Because the LED is designed to be used in lighting, manufacturers do not focus on measuring and providing dynamic parameters, neither electrically nor optically. Therefore, by applying the method suggested in section 2.2, we can model the electrical behavior of the selected LED, obtaining the value of the three passive elements. Being R_p and, C equal to , 0.0514 Ω and 4.3 nF respectively, and R_s, dependent of the injected current equal to $(0.72\ \Omega/LED_{current})$. It is important to clarify that the equivalent circuit represents the electrical behavior of the LED but does not take into account the electrical-to-optical factor. Also, since the physical dynamics of the LED, such as the phosphor conversion time, are not modeled, the optical bandwidth of the LED is not the same as the electrical bandwidth.

In the course of this work, the LUW CN7N LED reached the end of its life cycle (Discontinued), forcing us to look for other options. OSRAM LEDs has five different life cycle stages, which are in order: full production (), pre-production (), not planned for new designs (), ordering and shipping still possible (), and discontinued (). In this way, a candidate to replace LUW CN7N was searched, selected, and tested. The most suitable LED replacement was the LUW H9GP, which is electrically very similar to the LUW CN7N, allowing the use of the same elements to drive and equalize it. Moreover, the emitted light is cold, and the product is at the beginning of its life cycle (full production). This shows that the electronics, not just the software, must be up to date to avoid obsolescence in the products being designed. A comparison of the main parameters of both LEDs

[1] Measurements were performed using the PDA10A2 Thorlabs PD (150 MHz bandwidth).

[2] Prices obtained from www.mouser.es on 27-May-2021 and 27-Jul-2023 respectively

is given in table 5.1.

After having the characteristics of the selected LED, the driver is designed. In our case, we defined two drivers. One that sets the LED to a working current and allows the input of an AC signal to modulate the polarization point and thus modulate the light intensity. The other takes advantage of knowing the equivalent circuit of the LED and adds an equalization stage that tries to squeeze out the maximum bandwidth that the LED can provide. This second approach allows faster applications but at a higher cost. The driver cost will depend mainly on the quality of the amplifiers chosen and the speed of the microcontroller.

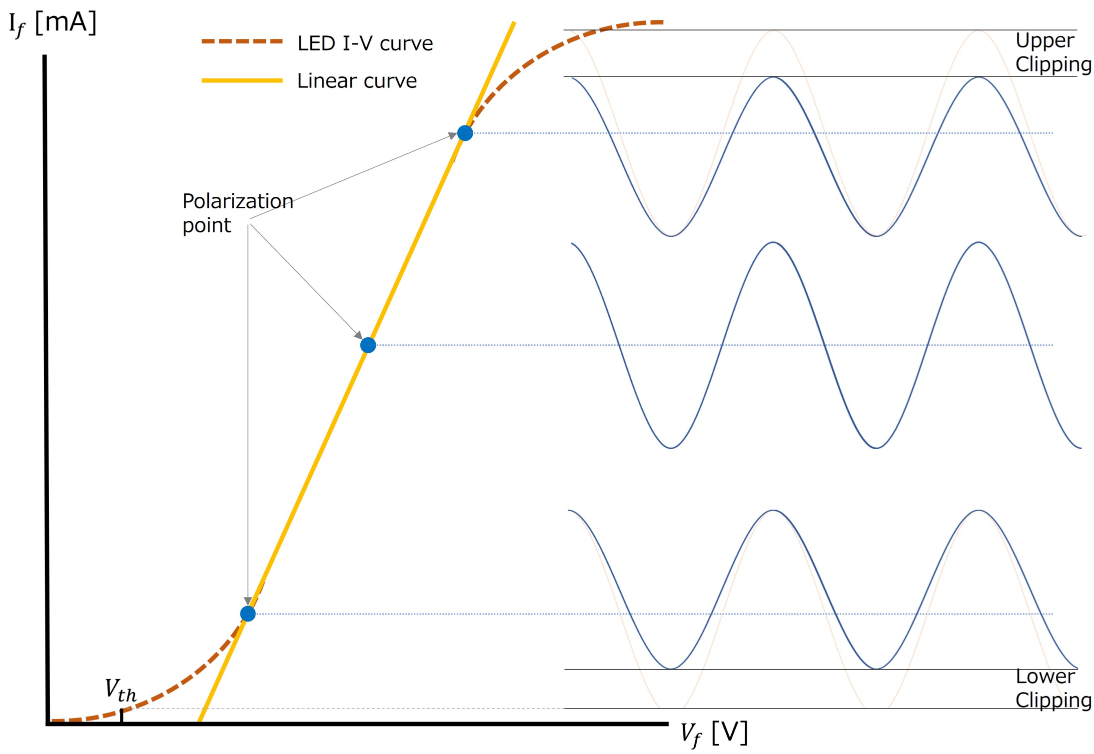

Figure 5.2: Effect of the DC bias on the transmitted signal.

LEDs, unlike other transmitters, do not get better as the power increases. They have an optimum range where information can pass without clipping. This optimum point depends on the IV curve of the LED and the span of the AC signal. Also, the power of the AC signal must be limited to the linear range of the LED to avoid distortion, overheating, and reduction of the lifespan of the LED [122]. To modulate the LED it is better to dimmer the light instead of turning it on and off. To illustrate all these parameters, Fig. 5.2 shows how different polarization points change the quality of the transmitted signal.

In the case of this prototype, we use an n-channel MOSFET configured in a voltage divider biasing arrangement. This configuration is often used to set a bias point for a given AC signal. It can always be assumed that the gate current is 0 A to allow isolation of the voltage divider network from the output section. As explained

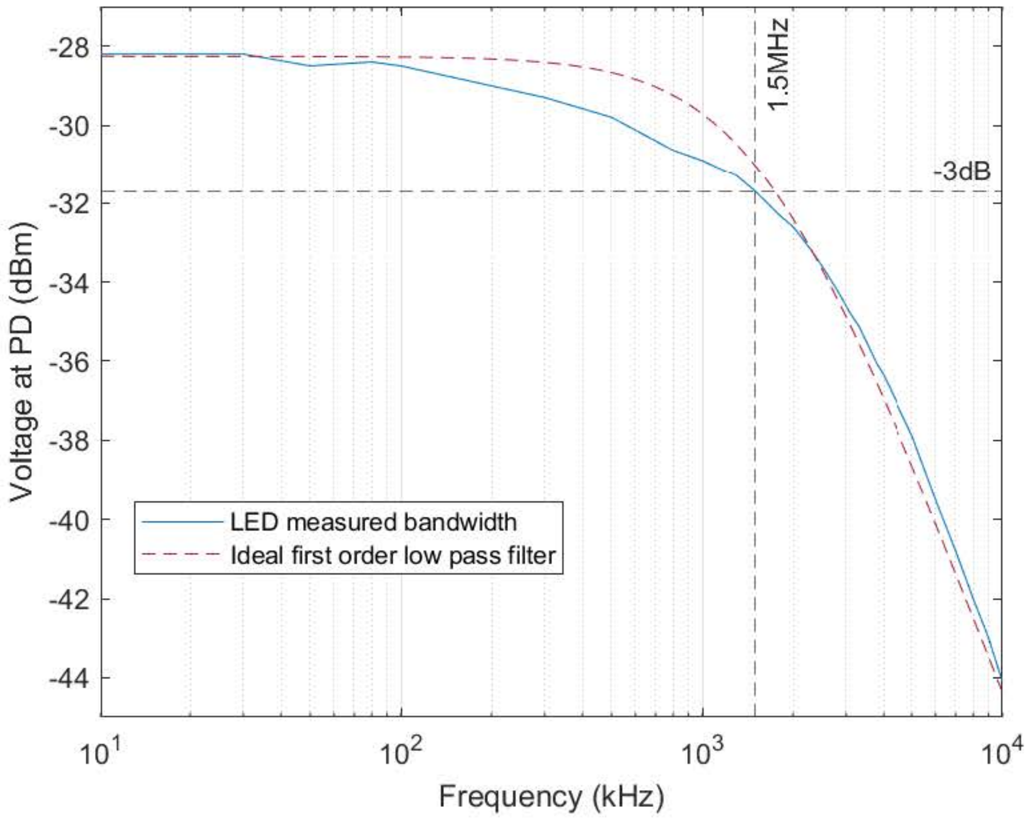

Figure 5.3: Frequency response of the LED LUW CN7N.

previously in subsection 2.3.1, the operating point of the transistor depends mostly on the passive components of the circuit and not on its characteristics, making it resistant to temperature variations and manufacturing effects and thus ensuring an optimal polarization point that maintains the quality of the transmitted information.

The optical frequency response of the LED driven by the MOSFET configured with a voltage divider is measured using the Thorlabs PDA10A2 PD and is shown in Fig. 5.3, where the 3 dB bandwidth is reached at 1.5 MHz. It also models the first driver response, making it suitable for medium-speed applications.

The second driver follows the same configuration for DC biasing the LED but adds two equalization stages. The goal of the equalization process is to expand the range over which the magnitude of the transmitter frequency response remains flat.

The overall bandwidth of the system will significantly greater with the inclusion of a pre-equalization circuitry than it would be with the LED alone.

The optical response of the LED LUW CN7N can be modeled as a low pass filter with a pole at 1.5 MHz, as shown in 5.3. Following this, we designed a passive equalizer followed by an amplification stage to keep the signal in the desired voltage range. The passive equalizer stage is composed of three elements, a resistor (R_1) in parallel with a capacitor and a load resistor (R_2) as depicted in Fig. 5.4. The transfer function of the circuit is then:

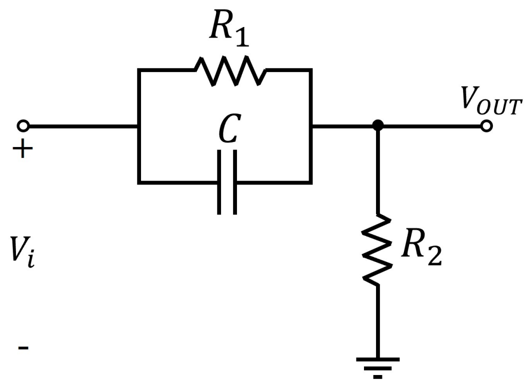

Figure 5.4: Pasive equalization circuit using RC components.

$$H_{equ}(s) = \frac{R_2}{\left[R_1 || \frac{1}{sC}\right] + R_2}$$

$$H_{equ}(s) = \frac{R_2}{R_1 + R_2} \cdot \frac{1 + sR_1C}{1 + s\left(\frac{R_1R_2C}{R_1+R_2}\right)} \tag{5.1}$$

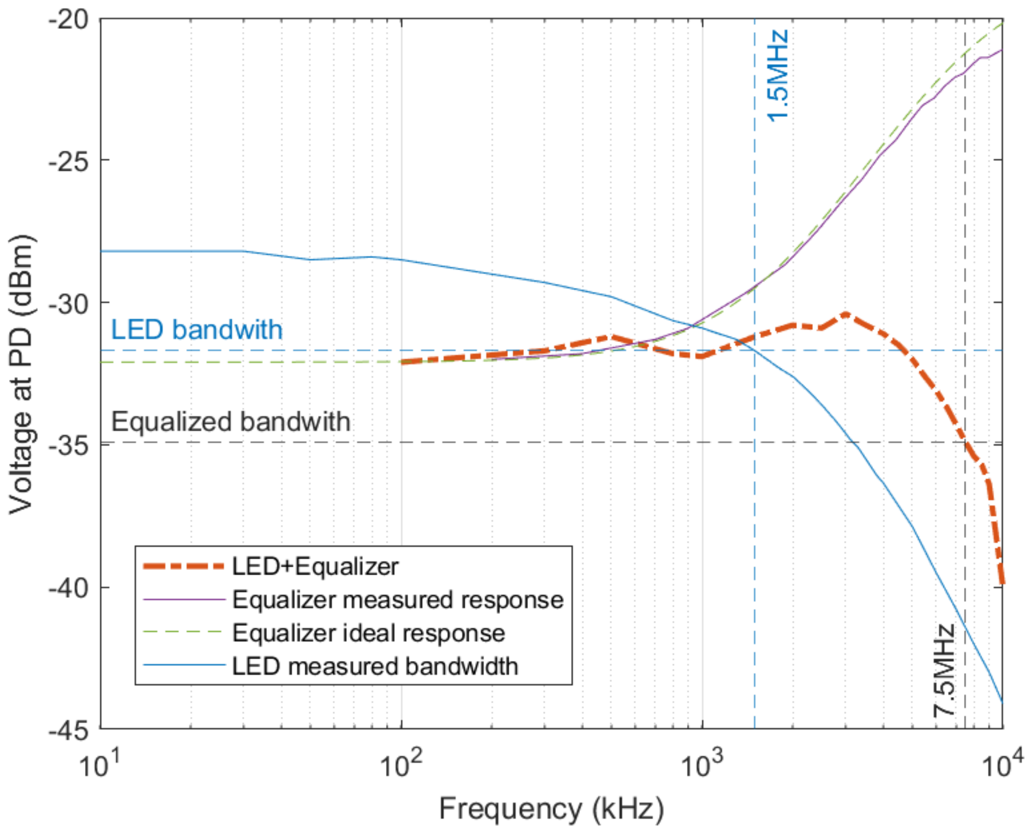

Figure 5.5: Frequency response of the LED LUW CN7N with a passive pre-equalizer.

Where the zero frequency will be $\omega_z = \frac{1}{R_1C}$ and the pole frequency will be $\omega_p = \frac{R_1+R_2}{R_1R_2C}$. The equalizer zero is then calculated to match the pole induced by the LED, and therefore, the response of the system will be dominated by the equalizer pole (ω_p), which in this case was configured to be around 10 MHz. The transfer function with the equalizer and the LED when $\omega_z = \omega_{LED}$ will be then:

$$H_{LED}(s) \cdot H_{equ}(s) = \frac{KR_2}{R_1 + R_2} \cdot \frac{1}{1 + s\left(\frac{R_1 R_2 C}{R_1 + R_2}\right)} \tag{5.2}$$

Where K is the attenuation factor. The optical frequency response of the LED plus the passive equalizer (with $R_1 = 1k\Omega$, $R_2 = 100\Omega$ and $C = 100pF$) and the gain stage is measured again with the Thorlabs PDA10A2 PD and is shown in Fig. 5.5, where the 3 dB bandwidth is reached at 7.5 MHz. In further research, we achieve 20 MHz of bandwidth with the addition of a second passive equalization stage that was adjusted to match the zero with the pole of the first stage and added one pole further away. The circuit used to achieve these results is shown in Fig. 5.6.

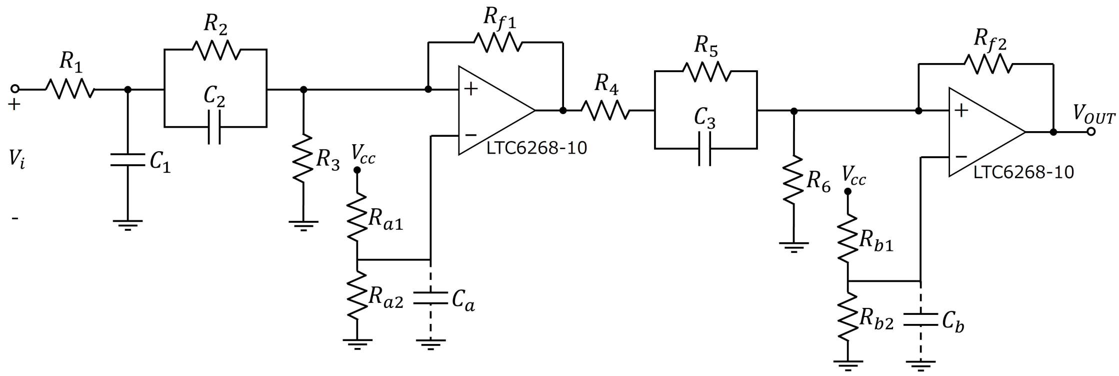

Figure 5.6: Two-stage pre-equalizer.

Now that the LED and its driver are covered, it is time to discuss the power source. Since the prototype is designed to be easily deployable, the most common way to power the LEDs as a light source is through the facility's power supply. In Europe, the power supply is standardized to 220 VAC at 50 Hz. Therefore, the first step is to convert the AC to DC and reduce the input voltage to a working range, ideally between 12 and 9 volts. The main limitations of the AC/DC converter are its size and its price, as the prototype should be small while providing the minimum power needed to turn on the microcontroller and power one or two LUW CN7N LEDs (about 2 W). The chosen AC/DC converter was the PBO-3C-9 from CUI INC. This converter is an ultra-compact open-frame power supply that has dimensions of just 26.4x12.58x11 mm. As the solution is intended to cover multiple applications, the PBO-3C-9 also offers operational and safety regulatory certificates that include 60601 (medical), 60335 (household appliances), and 62368 (audio, video, and information and communication technologies).

The additional components were selected according to the vendor's suggestions to comply with the standards for indoor civil/general applications, resulting in the Printed Circuit Board (PCB) with dimensions of 41.5x18x 28.5 mm.

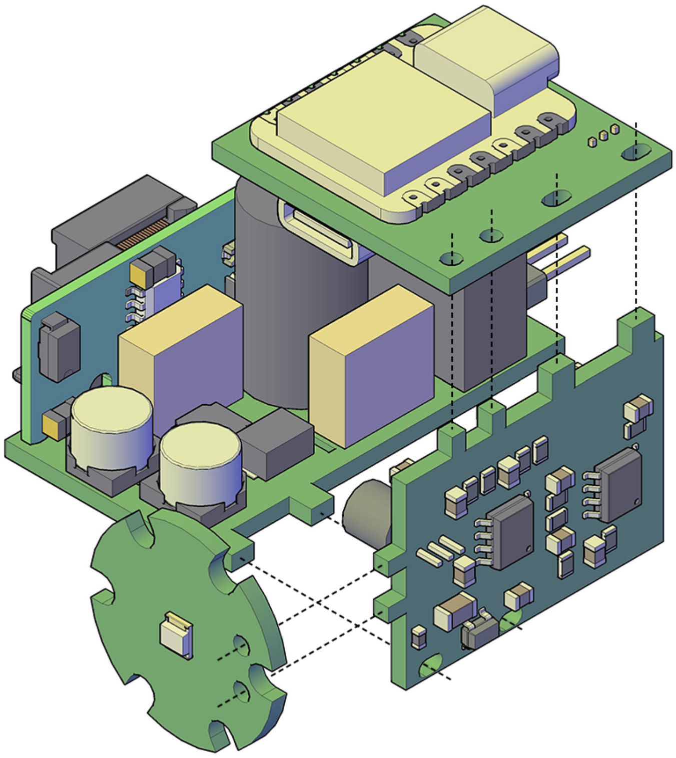

Figure 5.7: Exploded view of the PCBs that compose the TX.

The selected microcontroller is the Seeed XIAO SAMD21, which is the smallest microcontroller with a ready-to-use ATSAMD21G18A-MU. The Seeed XIAO allows fast reconfiguration, ideal for the prototyping stage. Yet this element will be replaced with an ad hoc chip that reduces the size, cost, and power consumption of the final product (mass-production). The microcontroller will be further discussed in the software implementation section, as it is responsible for communication control and message storage. Finally, all mentioned elements are connected in a 3D PCB arrangement for space optimization. The AC/DC converter board provides a 9 VDC

(a) **(b)**

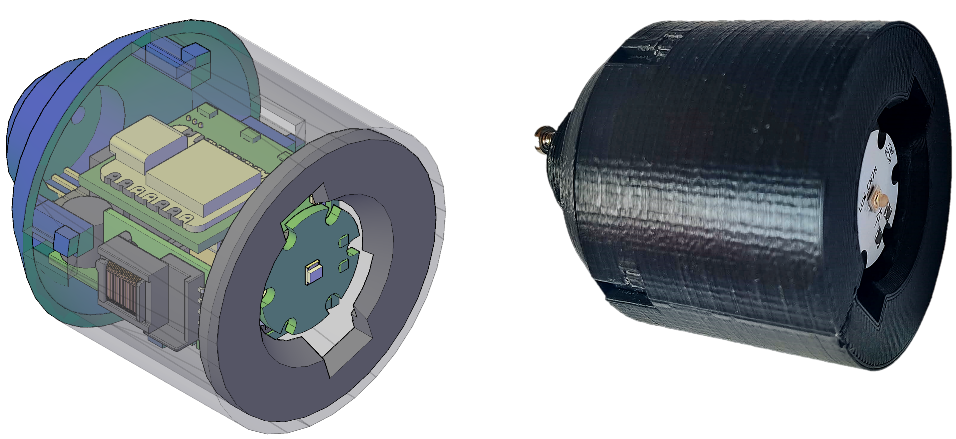

Figure 5.8: Final TX device a) Render of the design, b) Actual element.

output to the driver board. The driver board has a DC/DC converter that reduces the 9 VDC to the 5 VDC needed for both the op-amps and the microcontroller. The driver board also has two outputs, which are the modulated signal with the DC offset for the LED board and a 5 VDC output for the microcontroller board. The microcontroller board sends the modulated signal back to the driver board.

The design is compatible with standard GU10 and GUZ10 LED connection, and the PCB of the LED has typical dimensions used by LED manufacturers to bring flexibility and compatibility at the moment of selecting the desired reflector/lens. In the case of this prototype, we used the round reflector F15558 MIRELLA-G2-S which has a spot beam of 15°.

5.2.2. Receiver

The other major part of the hardware is related to the receiver. Optical signals arriving at the receiver's PD are detected, amplified, and recovered. Photodetectors work on the principle of the photoelectric effect, which involves the emission of electrons (electric current) from a material when it is exposed to light. PIN (P-type - Intrinsic - N-type) photodiodes or phototransistors are the most commonly used options for this purpose because of their high response speed, good sensitivity, excellent dynamic range, high stability, robustness, and low cost. Typically, the current generated is very low, requiring a front-end amplifier to boost the signal strength before further processing.

The photodiode chosen is the BP 104 S-Z from OSRAM. The BP 104 S-Z is a silicon PIN photodiode with an active area of $4.84mm^2$ and a spectral sensitivity of 0.62 A/W but at a wavelength of 850 nm (near Infrared (IR)). The PD sensitivity for VLC must ideally be around 450 nm (blue light) to match the spectral emission of the white LED. However, as PD technology has evolved to meet the requirements of fiber-optic communication, the market has focused on the most common wavelengths used for fiber transmission (850 nm, 1300 nm, and 1550 nm), with 850 nm being the oldest and most widely adopted technology [123]. In that way, the efficiency of the photodetector at 450 nm is around 30%.

In VLC systems, a large-area PD should be used at the receiver to maximize optical signal detection. However, large-area PDs have large intrinsic capacitances, resulting in reduced receiver bandwidth. Since the selected photodiode has a small area, its junction capacitance C_j (subsubsection 2.1.2.2) is only 50 pF when no reverse voltage is applied, which is good enough to be used as an input to the transimpedance stage. The problem of the amount of light collected by the small active area is overcome by adding a lens at the receiver end.

As mentioned in subsection 2.3.2, the TIA feedback must be calculated taking into account the input capacitance (PD) and the amplifier GBW to avoid instability. We have chosen two different TIA, one with a high open loop bandwidth, low noise,

Table 5.2: Comparison between amplifiers used as TIA in the RX.

	LMH6703 [124]	OPA381 [125]
GBW(MHz)	1800	18
Slew rate(V/µs)	4200	12
Input Bias Current (I_B)(pA)	$2 * 10^6$	3
Supply current (I_S)(mA)	11	0.8
Shutdown pin	Yes	No
Price(€) [2]	4.33	1.92

and low distortion output, which allows us to obtain a good voltage level without compromising the overall system bandwidth. The second is a low-power amplifier with a reduced open loop bandwidth compared to the first but with advantages in terms of cost and power consumption. A brief comparison of the main aspects of both for this prototype is given in table 5.2, with the less optimal performance highlighted in red.

The resulting worst case C_{in} for the LMH6703 and OPA381 is 51 pF and 53.5 pF, respectively. It is desirable to maintain the LED bandwidth when using the OPA381 and at least the equalized bandwidth in the case of the LMH6703. Since both amplifiers are supplied with the same voltage, the maximum feedback resistance for both can be obtained by applying (2.21), which results in 28 KΩ. The trans-impedance bandwidth can be obtained by applying (2.20), resulting in 14.2 MHz for the LMH6703 and 1.38 MHz for the OPA381.

Since the bandwidth obtained for the OPA381 at maximum resistance is not sufficient to cover the LED bandwidth, the feedback resistor is changed to a 10k resistor, resulting in a bandwidth of 2.3 MHz. The feedback resistor for the LMH6703 is also changed to 20k. A good approximation of the feedback capacitor can then be obtained by using 2.19, where C_f is 0.5 pF and 7.4 pF for the LMH6703 and OPA381, respectively. C_f creates a pole that can reduce the final bandwidth. The larger C_f, the closer the pole, so it is ideal to choose the lowest value that will provide stability.

The TIA output is then connected to the analog pin of the receiver microcontroller and a comparator (LMV7219M5X). The comparator output is also connected to a General-purpose Input/Output (GPIO) pin of the microcontroller. The microcontroller used is the one contained in the EMB1061 SoC. This element takes the information received from the photodiode and generates an array of bits to be transmitted via BLE. The details of this process will be further discussed in the sub-section subsection 5.3.2.

The selected lens is desired to have the smallest focal length, which means that

[2] Prices obtained from www.mouser.es on 1-May-2023

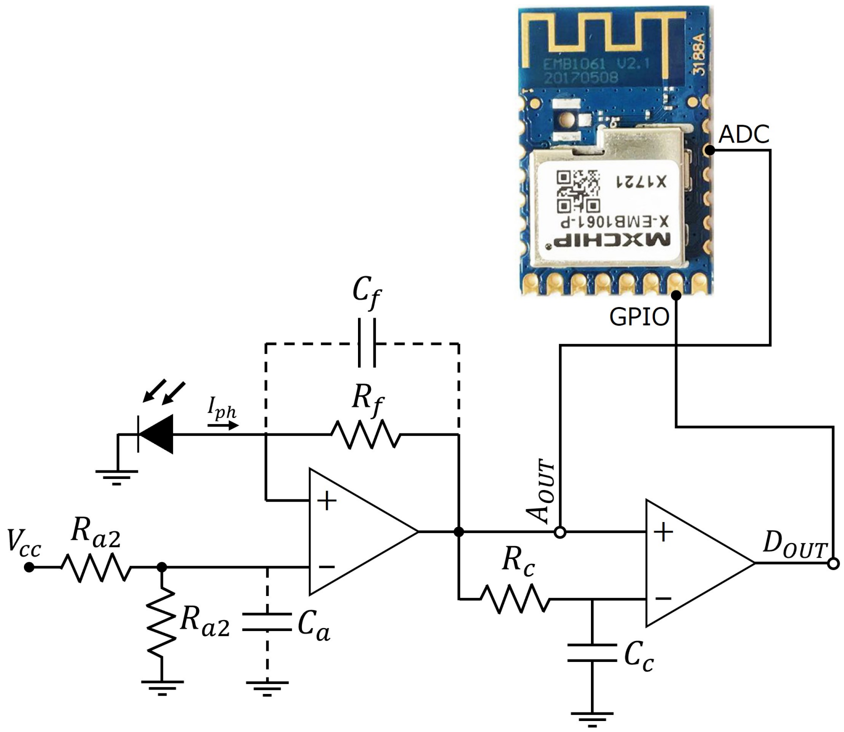

Figure 5.9: Circuit diagram of the receiver signal conditioning and the connection with the EMB1061 SoC.

the lens is closer to the PD (small size) while having the biggest diameter possible to capture as much light as possible. In that way, to augment the signal received by the photodetector, we use a Fresnel lens of a focal length of 10 mm and a diameter of 13 mm (sold by Knightoptical) [126].

The design of the receiver PCB layout is also important because the current generated by the PD is so small that any noise induced by any other pad can be greater than the signal itself. With this in mind, we keep the photodiode as

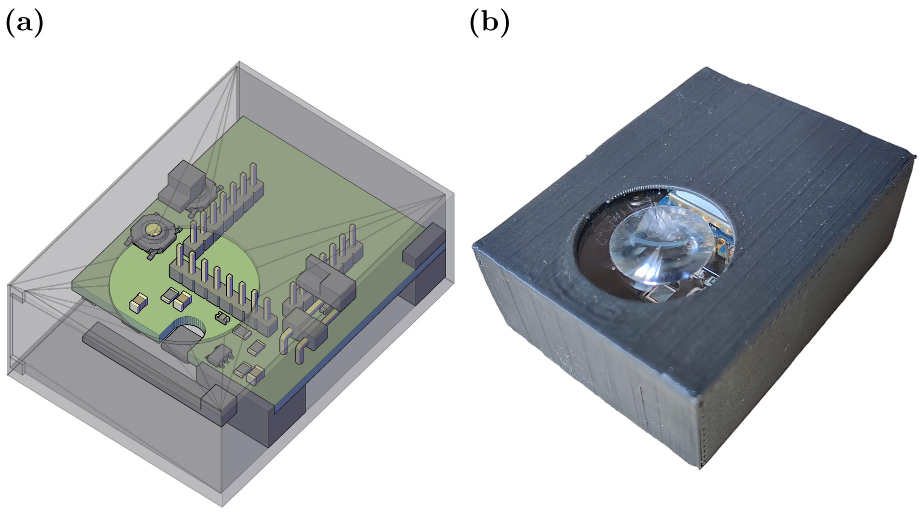

Figure 5.10: Final RX device a) Render of the design, b) Actual element.

close as possible to the amplifier, and, following the manufacturer's instructions, the feedback elements (R_f and C_f) are also close to the opamp. As the source is only positive and is supplied by a battery (clean signal), only one capacitor is required to ground the positive supply. The copper area around the amplifier and the PD amplifier signal are cropped to avoid undesired inductions.

The selected amplifiers are pin-compatible, which means that the same PCB design will work with the selected amplifier simply by selecting the correct passive components. The result is a small PCB measuring only 18 x 18 mm. An alternative design to achieve an even more compact and reduced prototype was to integrate the RX into the EMB1061 System on chip (SoC) board, as shown in Fig. 5.10.

The receiver is powered by a single CR2032 cell battery and can be turned on and off with a small switch located on the side. The final dimensions of the receiver device are 34.5 mm in width, 46.6 mm in length, and 17.6 mm in height.

5.3. Software implementation

The software that runs the system has been programmed using various tools. The seeeduino XIAO is programmed through the built-in Universal Serial Bus (USB) type-C using the cpp language. The EMB1061 is programmed using a self-designed PCB (DevBoard) which allows the connection of an ST-LINK (or J-TAG) for debugging (through the Serial Wire Debug (SWD) pins). The DevBoard also contains a USB to UART interface that allows serial communication through a USB type-C. The DevBoard can be powered from the USB type-C port or from a cell battery to allow unwired testing.

There is no DevBoard available on the market for the EMB1061 SoC that allows direct programming and serial communication, and therefore this design will provide a flexible platform not only for this prototype but for future implementations. Fig. 5.11 shows the actual PCBs and its size difference. The mobile application is developed using Android Studio IDE, coded using Java-based language and XML.

5.3.1. Transmitter microcontroller (Seeeduino XIAO)

The seeeduino XIAO hosts an ATSAMD21G18A-MU that provides multiple clocking options with a 48 MHz digital Frequency-Locked Loop (FLL) (DFLL48M). This maximum speed is preconfigured in the device setup process, so we do not need to go into details.

Even if the main system clock runs at 48 MHz, a GPIO output can be switched at a maximum of 350 kHz using predefined functions (digitalWrite) and 450 kHz writing directly to the registers. For this prototype, and as it could not be otherwise, all functions write directly to the registers, and the associated logic was kept to a minimum, taking advantage of arithmetic properties. After adding all the necessary

(a) DevBoard. **(b)** RX board.

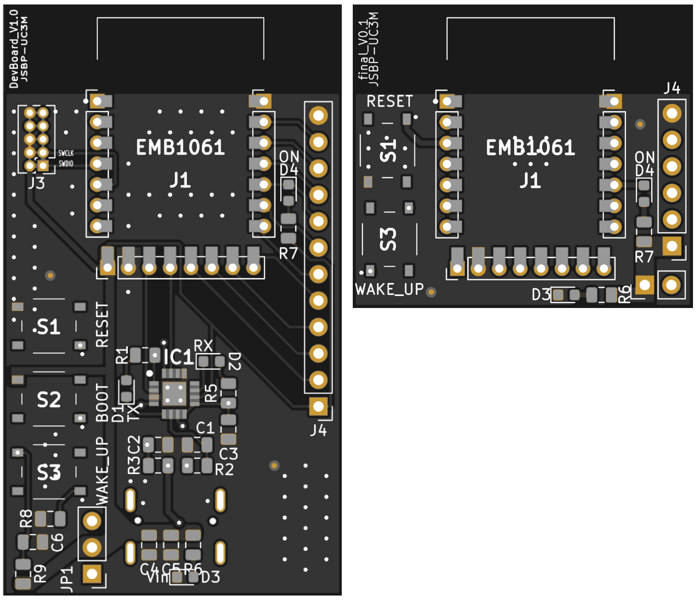

Figure 5.11: EMB1061 SoC PCB.

logic to send all the information (coded in 8b10b when needed), the maximum achievable speed was 260kHz, as shown in Fig. 5.12.

Even though the TX hardware is capable to support switch speeds of 1.5 MHz (or 20 MHz equalized) with low distortions, the microcontroller used cannot explode all of the available bandwidth. Nevertheless, the transmission speed (260 kHz) is sufficient for the target applications of this prototype. If more bandwidth is needed, it is only necessary to replace the microcontroller with a faster one, leaving the rest of the TX intact as shown in Fig. 5.7.

The PHY layer of the IEEE 802.15.7 standard for VLC systems defines three different modulation schemes: OOK, PPM, and CSK. In the case of this prototype, we use an NRZ-OOK modulation scheme, which adds simplicity to the system. The protocol also defines some Run Length Limiting (RLL) line coding to limit the total number of equal bits that can pass before a transition. This coding helps to avoid data recovery and flicker problems that can occur with long sequences of equal bits. The RLL coding also helps maintain a DC-balanced signal, which in VLC represents a constant brightness level of the light source required to maintain the lighting quality of the beacon. IEEE 802.15.7 proposes three different RLL encoding formats: Manchester, 4b6b, and 8b10b. The Manchester code expands each bit into a coded 2-bit symbol, so that a '0' bit is transmitted as '01', and a '1' is transmitted as '10'. It is easy to see that the Manchester encoding cuts the bit rate in half, but its implementation is straightforward. The 8b10b maps an 8-bit word into a 10-bit balanced word, the goal is that the difference between the number of zeros and ones in a 20-bit word is no greater than two in the worst case, and there will never be more than five equal bits in a row.

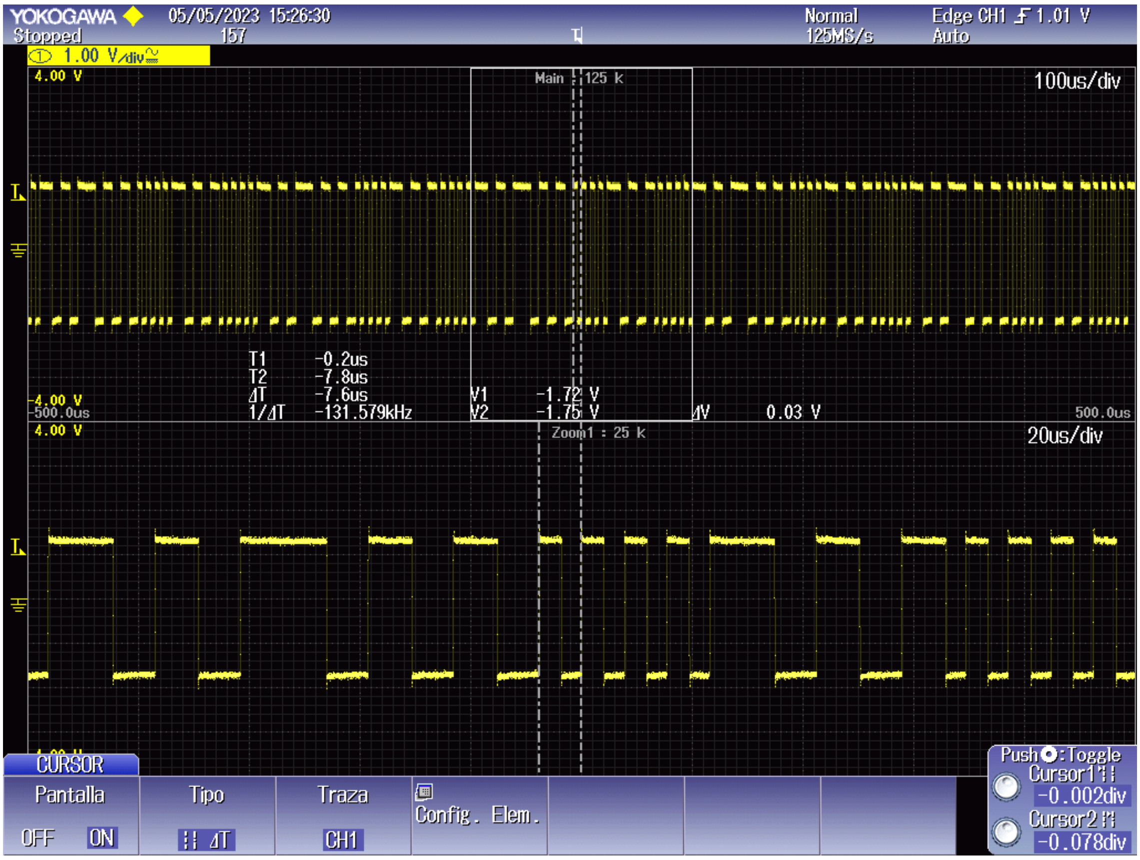

Figure 5.12: Signal measured at the GPIO of the seeeduino XIAO.

Table 5.3: Running disparity (RD) rules for 8b10b run length limiting (RLL) code.

Previous RD	Code word disparity	Chosen disparity	Next RD
-1	0	0	-1
-1	± 2	+2	+1
+1	0	0	+1
+1	± 2	-2	-1

Since, in the long run, the number of zeros and ones must be equal, the code takes into account the Running Disparity (RD) of the previous 10-bit word to encode the next one, as shown in table 5.3, making the implementation more complex compared to the other two RLL. The 8-bit word is split in two to create the 10-bit encoded-word. The lower 5 bits are encoded into 6 bits, and the upper 3 bits are encoded into a 4-bit word, which is then concatenated to produce the 10-bit balanced word. The 8b10b RLL was the one implemented in this prototype, creating a library in cpp that is capable of doing the encoding and decoding of any word in a fast way. The 4b6b, like the 8b10b, takes a 4-bit unbalanced word and maps it to a 6-bit balanced one. The encoding overheads for each of the three RLL codes described above are compared in the table 5.4.

When it comes to the frame structure, the prototype data frame is defined as

Table 5.4: Coding overhead for different run length limiting (RLL) codes [127].

Word size	RLL code	Codeword length	Coding overhead
	Manchester	16	100%
N=8	4b6b	12	50%
	8b10b	10	25%

proposed by IEEE 802.15.7. It has three different blocks at the PHY level: The Synchronization Header (SHR), the Physical Header (PHR), and the Physical Service Data Unit (PSDU). The SHR, in turn, is divided into the Fast Locking Pattern (FLP), which will be the pattern used to identify the beginning of the packet, and the Topology-dependent Pattern (TDP), which contains the information related to the codification that the data will have. The PHR defines the size of the PSDU.

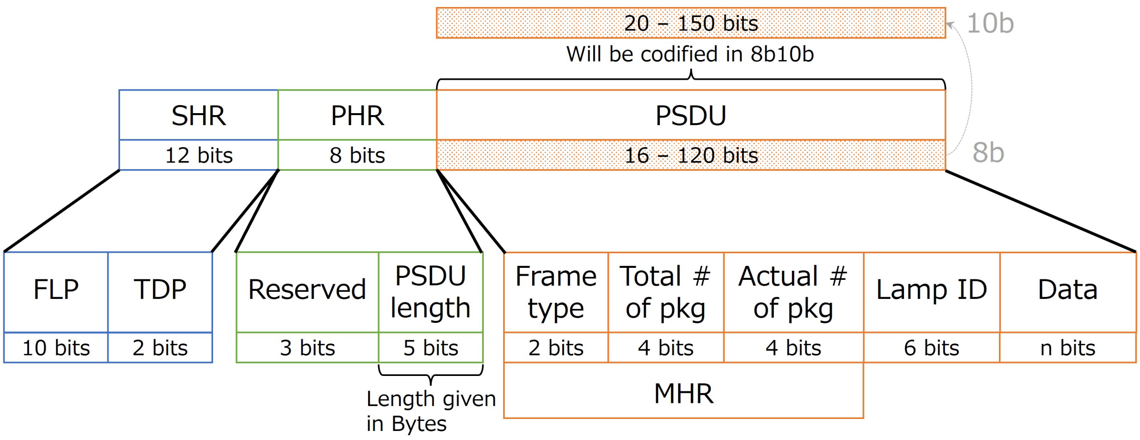

Figure 5.13: Prototype VLC frame structure.

These two blocks, the SHR and the PHR, are not encoded with the RLL. The PSDU contains the transmitted data together with the MAC Header (MHR). The MHR contains all information related to the MAC layer, e.g., the frame type, the MAC security, and the packet number. The frame structure used in the prototype and the assigned bits are shown in Fig. 5.13.

5.3.2. Receiver SoC (EMB1061)

To examine the SoC receiver, it is first necessary to clarify why this module is used and not another. In the following explanation of how to set up the device, it can be noticed that the process is not as simple as with other "more popular" widely used devices.

One of the key parameters of the solution is competitive cost, and in this aspect, the module is unbeatable, costing only three euros [3], which is extremely cheap compared to other modules, where the cheapest (with fewer features) are around seven euros [3,4], more than double the price. It also offers an integrated M0 processor, 160 kB of Flash, and 24 kB of RAM, among multiple clocks and communication protocols. It is even FCC-approved. Another aspect that makes it suitable for this solution is that it has an ultra-low power consumption profile, with the manufacturer claiming that the device can operate for more than three and a half years on a single CR2032 cell in connected mode.

In order to create a working BLE application we needed to configure some things before, in our case as we used the open source code editor Visual Studio Code (VS-code) we must add the extensions that allow to compile, program and debug the SoC. First, as the code was done in cpp, both c and cpp extensions must be installed. Then, the BlueNRG-12 DK must be installed to have access to all the tools required to configure the SoC. In order to compile the project on VScode, the cortex-debug extension by marus25 is installed. Finally, for debugging porpuses the Open On-Chip Debugger (OpenOCD) is also installed. It is relevant to highlight that all the tools used to write down, compile program and debug the EMB1061 are open source so no license is required making the development and future commercialization process cheaper.

In the first run, it is possible to have errors in the object files (.o). If it is the case, open the BlueNRG1.ld file and add the following missing references:

$$
\begin{gathered}
.ARM.exidx : \{ \_\_\_exidx\_start = .; \_\_\_exidx\_end = .; \} \\
.ARM.cxa : \{ \_\_\_cxa\_end\_cleanup = .; \\
\_\_\_gxx\_personality\_v0 = .; \; abort = .; \}
\end{gathered}
$$

Another problem may occur when initializing the BlueNRG stack (**BlueNRG _Stack_Initialization**). The method is defined in the BlueNRG-12 DK and is therefore not modified by us, although the method returns the out-of-memory flag. To correct this, the DK files must be modified to define the correct size of the Bluetooth stack. A post has been made to Stack Overflow to help any developer with the same problem.

The EMB1061 is programmed using the DevBoard (Fig. 5.11) before it is inserted into the RX board. Programming can be done in two ways. First, through the integrated USB type C using the RF-Flasher utility (ST), which allows reading, mass erasing, writing, and programming the flash memory of the ST wireless SoC devices. Second, by using the ST-LINK ports, which also support the debugging process. To program the device through the ST-LINK link, we need a stand-alone debugger and programmer from ST. In our case, we used the STLINK-V3MINI (replaced by the STLINK-V3MINIE), which is a tiny debugger of only 15 x 30 mm

[3]Prices obtained from www.mouser.es on 9-Jun-2023

[4]Some devices took as reference were RN4871U-V/RM118, CYBT-343026-01, BLE112-E-V1

and very cheap.

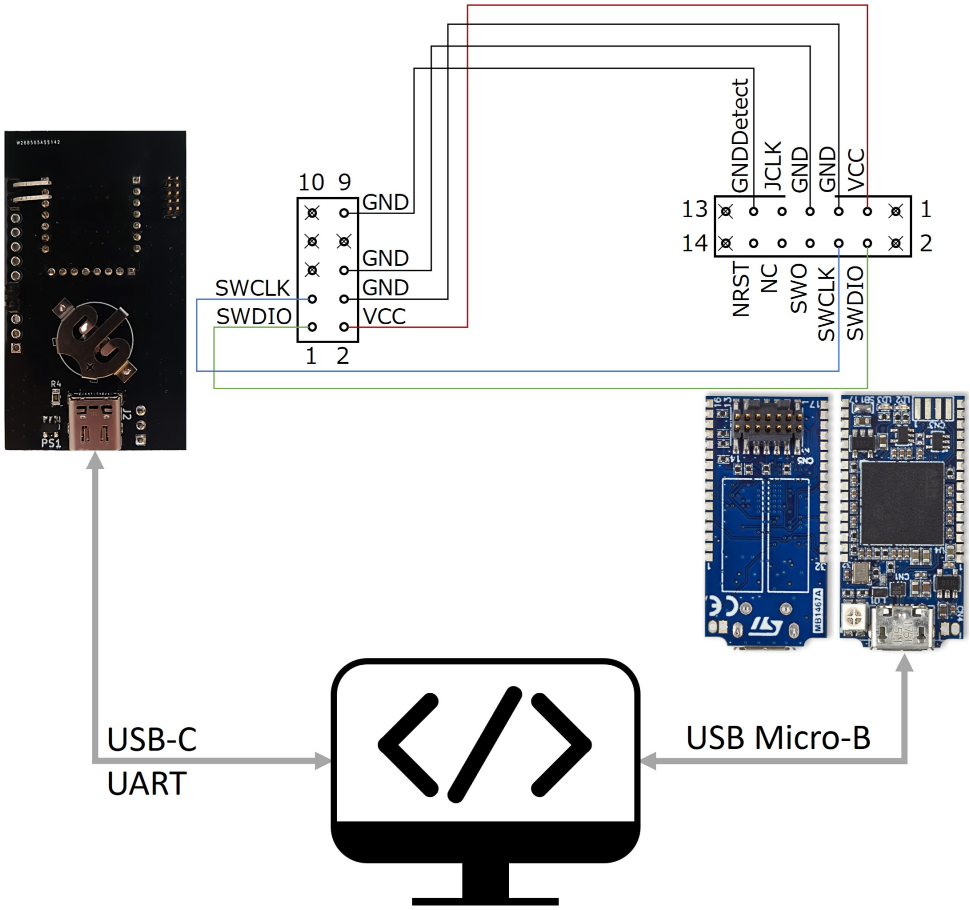

Figure 5.14: Debugging connection.

The EMB1061 module's connection methods are slow, so data is not sent to the mobile device until the BLE characteristic size is full. In this way, the receiver starts in the **START_ADVERTISING** state and does not record any received information. In the case of this prototype, we use the default ATT_MTU length, which is 23 for LE [128] (Vol 3, Part G, 5.2.1) and therefore, as the characteristic size is defined by *ATT_MTU-3* octets, the characteristic length will be 20 bytes (160 bits).

The receiver **MAC address** is *EB:64:55:**:**:***, and the advertised name is **Light Dongle**.

The BLE is configured to have a client-server architecture, and therefore, the profile used is the Generic Attribute Profile (GATT). The GATT profile is supported by the Attribute protocol (ATT) and defines a framework for data exchange. The EMB1061 will act as the GATT server in this prototype. Each and every attribute is identified with a unique Universal Unique Identifier (UUID) that is known and allows to address the transmitted information. In the case of this prototype, the defined UUIDs are:

Service UUID: *0000aaf0-0000-1000-8000-00805f9b34fb*
Characteristic 1 UUID: *0000aaf1-0000-1000-8000-00805f9b34fb*
Characteristic 2 UUID: *0000aaf2-0000-1000-8000-00805f9b34fb*

The device can host more services and characteristics if required. The top level of the hierarchy is a profile. A profile contains services, which at the same time are the container of the characteristics [128] (Vol 1, Part A, 6.4-6.5). Services are identifiers to organize the different characteristics and are typically associated with a specific feature. Characteristics are items of data that contain a value related to a particular device state or some environmental value collected by a sensor. Characteristics can also contain optional information about the received value, such as type, properties, or permissions.

- The GATT profile contains:
  - Services, which in turn contain:
    * Features, which may include:
      · Descriptors.

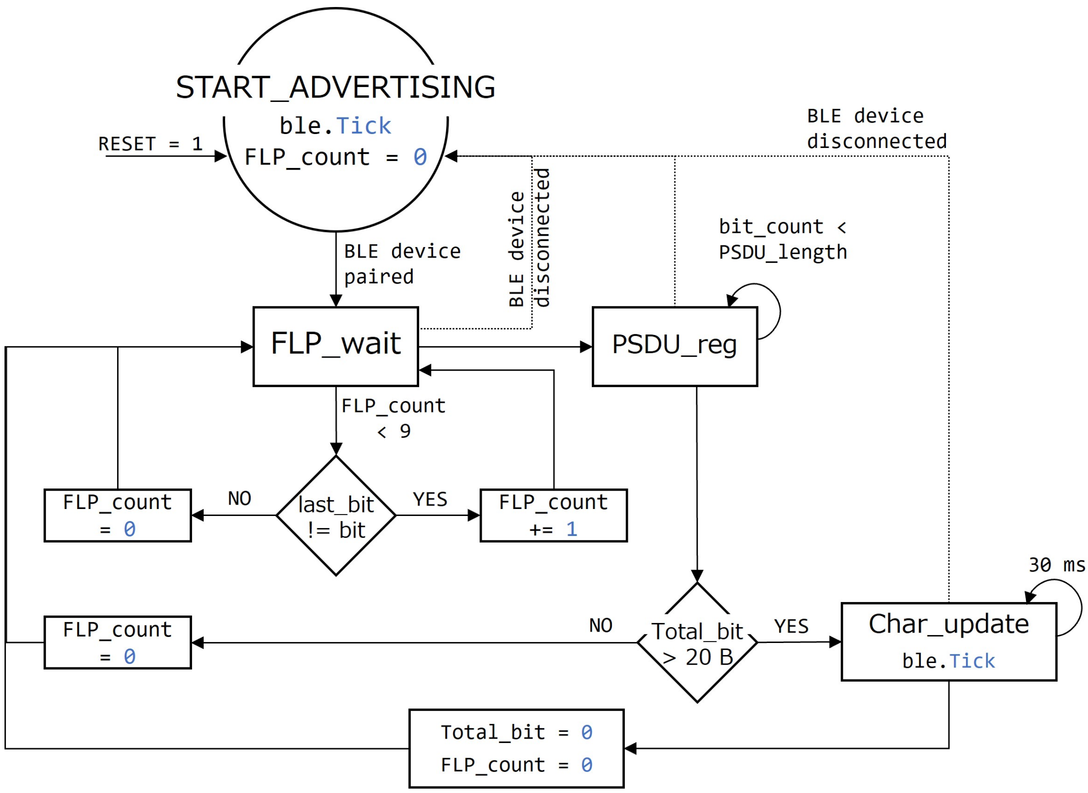

Figure 5.15: Flow diagram of the receiver.

When a device is connected to the Light Dongle, the state changes to **CONNECTED**, and data collection begins. The device waits for the FLP, i.e., it counts the changes in the GPIO state and goes to the next stage only after the value of the signal has changed ten times in a row. After the FLP, the device registers the length of the PSDU and defines the total number of bits to be registered for each packet. All the PSDU bits are registered in the characteristic and then transmitted to the mobile device without decoding the 8b10b. This process should be done before the BLE transmission to maximize the information that can be sent to the mobile device, but, in this case, since we are exploding the maximum sampling speed, any extra process will reduce the VLC speed. Finally, when all the PSDU bits are registered, the device returns to the waiting phase until the next FLP appears. When the 20 bytes of the characteristic are completed, the sampling process is stopped to send the information through BLE to allow the communication process to run without problems. The device remains in this state for 30 ms and then returns to wait for a new FLP. The flow diagram of the receiver is shown in Fig. 5.15.

5.3.3. Light Way: Android application

The application design process begins with conceptualizing the number of different screens, the information displayed on each screen, and the interaction between them. Even more specific aspects were considered, such as which screen the application would return to with the **back** button. Once the mockups were created and all requirements were verified, the application was developed in the Android Studio IDE.

Figure 5.16: Application icon and version.

To provide a clear understanding of what the application is supposed to do, the application requirements are listed first. Functional requirements specify what the system should do and therefore are always mandatory. Functional requirements ensure that the system meets the user's expectations.

Table 5.5: Light Way android application functional requirements.

ID	Statement
FR01	The system shall ask for the required user permissions if not already accepted
FR02	The user can choose the accessibility preference when first accessing the application or in the settings

ID	Statement
FR03	The user can select a BLE device compatible with the application when first accessing it or in the settings
FR04	The system shall direct users to BLE device selection when the application opens if no compatible device is connected
FR05	The system shall direct users to the main menu when the initial configuration process is complete and a compatible device is connected
FR06	In Settings, the user can select the language, set accessibility preferences, enable notifications, pair a BLE device, and find help
FR07	The system shall display a list of available BLE devices
FR08	The user can select a BLE device from the device list
FR09	The system shall connect to any compatible BLE device and maintains the connection
FR10	The system shall notify the user if a non-compatible device is chosen, and the selected device will not be paired
FR11	The user can return to the main menu using the "Back" button available on all screens
FR12	The user can select "Where am I?" to access information about their current location and surrounding information and locations
FR13	In the "Where am I?" screen, the system shall display the location of the nearest beacon
FR14	The user can select any nearby location displayed, and the system will guide the user to it
FR15	The user can search for any location, and the system shall guide the user to it, updating the information at each beacon
FR16	The system shall redirect the user to the "Where am I?" screen when the user reaches the desired location point
FR17	In settings, the system shall allow the user to disconnect the BLE device at any time
FR18	The system shall guide the user form its location to the emergency exit (or emergency assembly point)
FR19	The system shall display the device list when the user touches the "offline" status message
FR20	The system shall have the option to clear the data and behave as a first run

On the other hand, non-functional requirements define how the system is going to guarantee its quality. Non-functional requirements define how the system will meet the functional requirements and are not mandatory, but recommended.

Table 5.6: Light Way android application non-functional requirements.

ID	Statement
NFR1	Accessibility preference can be changed by the user at any time
NFR2	The system shall be developed with accessibility guidelines
NFR3	The system shall have a compatible BLE device connected to provide location and navigation information
NFR4	The system shall have at least Android 11 (API 30) installed.
NFR5	After selecting a BLE device the system shall redirect the user to the next application screen within 2s.
NFR6	The system shall display a notification message when no BLE device is connected
NFR7	The system shall have a responsive design to ensure proper display on any Android device
NFR8	The system shall have English and Spanish alphabets.
NFR9	The system displays a status icon, online or offline, depending on the device connection status
NFR10	The system shall support the connection of augmented reality glasses via USB-C
NFR11	The system shall update the layout to make the augmented visualization comfortable and useful
NFR12	The system shall perform 8b10b decoding of the received BLE data
NFR13	The system shall be able to retrieve the beacon ID information from the received data
NFR14	The system shall be able to retrieve the associated information from the received data
NFR15	The system shall be able to identify the package received and whether all the packages sent have already been received
NFR16	The system shall be able to launch the application when an augmented reality device is connected via USB-C when notifications are enabled
NFR17	The system shall remember the selected configurations

The application flow and screens are shown in Fig. 5.17. This gives a clear idea of what the user will find in the different stages of the application and what can be accessed. Each screen is then briefly described to explore the functionality and user interaction.

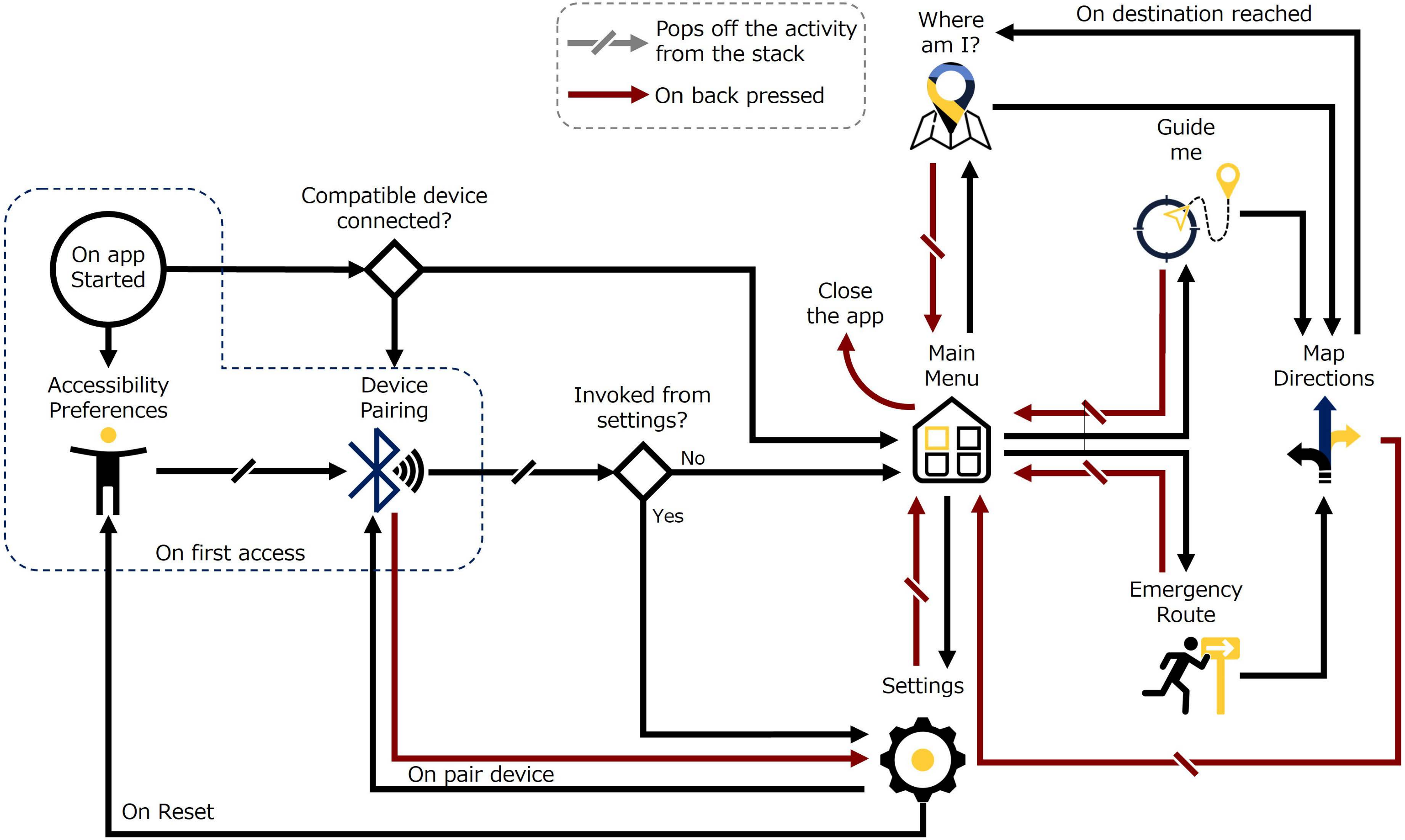

Figure 5.17: Flow diagram of the Light Way android application.

The first time the user accesses the application, the accessibility preferences are displayed for easy configuration without having to navigate to the settings. The user cannot proceed unless a preference is selected. In this first version of the application, the available options are *TalkBack*, which prompts the system to read the screen information and allow voice commands, *Close Caption*, which adds captions to any audible information the application presents to the user, and *Default*, which leaves the application without the aforementioned features as can be seen in Fig. 5.18. The preferences screen also allows to change the application language, which in version 1.0 could be English or Spanish.

(a)

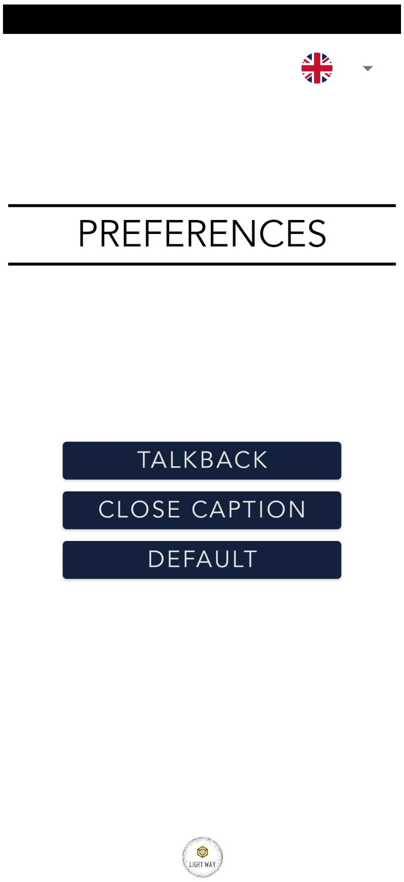

(b)

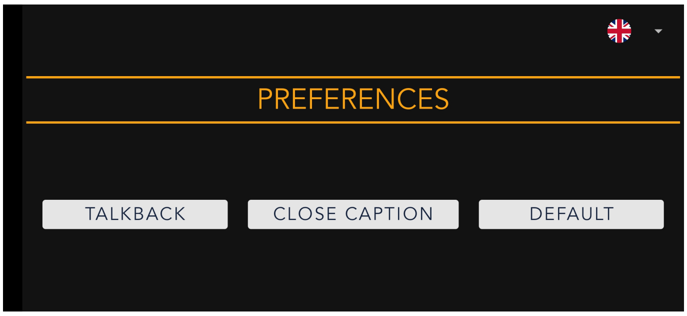

Figure 5.18: Accessibility Preferences screen.

The application provides a different visualization when the AR glasses are connected to the device. As in the case of this project, the AR glasses do not have their own Operative System (OS) and rely on the device to project any information that is currently on the screen. The black background is ideal because the projected image is made with LEDs. Therefore, black means that the LED is turned off, and all the surrounding area is visible in the black spots. On the other hand, there is white, which blocks the view and draws the user's attention to the projection. Then all relevant information and user interactions are displayed in white or bright colors. Also, the screen remains in landscape mode because the information is easy to read on AR glasses.

After selecting the accessibility preference, the user is presented with a list of available BLE devices. At this screen, if the user has not granted the necessary permissions to allow Bluetooth scanning, the application will prompt the user to grant them. If the user denies the permissions, the application cannot acquire any BLE devices, and the user cannot proceed. If the user grants the permissions but the device's Bluetooth is not turned on, the application prompts the user to enable this functionality. Once permissions are granted, and Bluetooth is turned on, the available BLE devices are displayed, showing their name, MAC address, and signal strength as shown in Fig. 5.19. If the user wishes to refresh the device prompt, the list can be swiped down to reload it, or the user can press the **Refresh** button to the right of the title.

(a) **(b)**

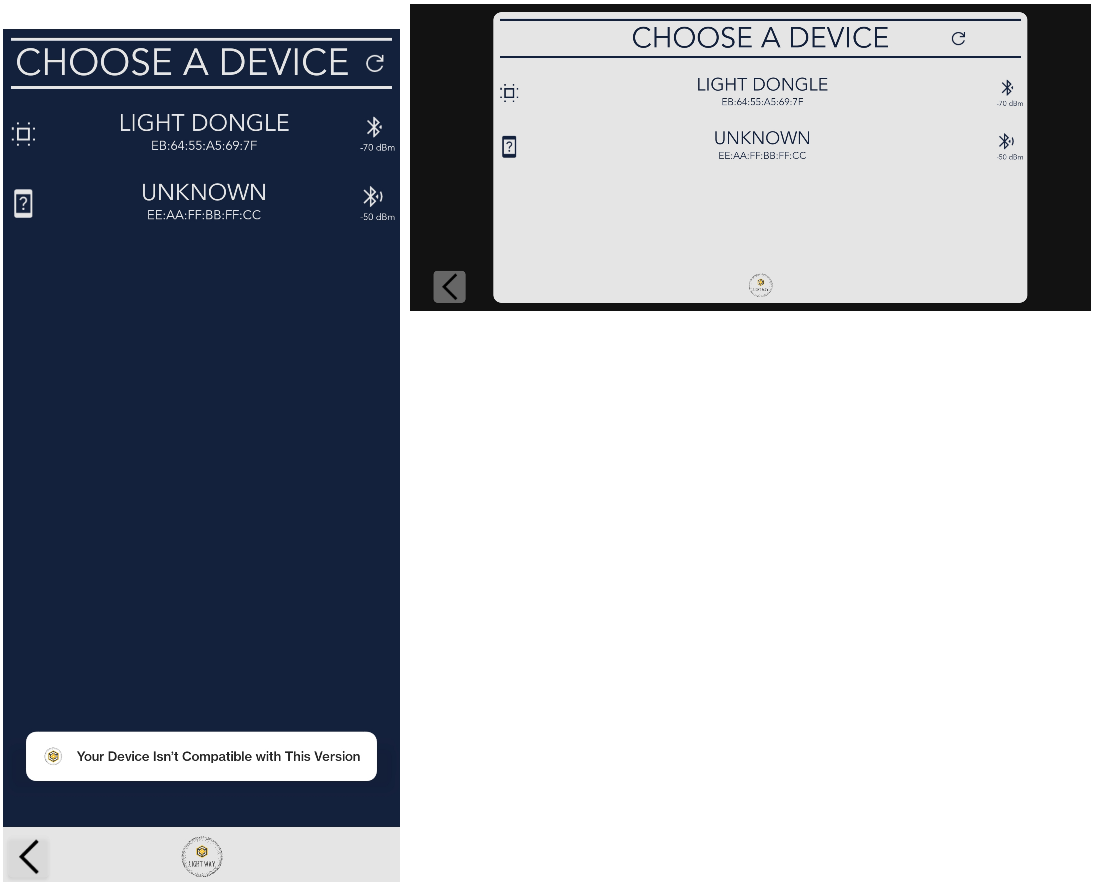

Figure 5.19: Device Pairing screen.

If the user chooses a non-compatible device, the system will alert the user, and the connection is not established.

After the initial configuration process, the user will find the main screen, which displays all the navigation options that the system can provide. The available functions are to tell the user where he is and the nearby locations, to guide the user to a desired location, to follow the emergency route, or to access the application settings. This screen also provides a connection status of the BLE device; if the device is disconnected for any reason, the status changes from online to offline (• online • offline), and the user can easily invoke the BLE device list by touching the status text when no device is paired ("offline"). The main screen has large icons that are easily accessible and highlighted in AR mode as shown in Fig. 5.20.

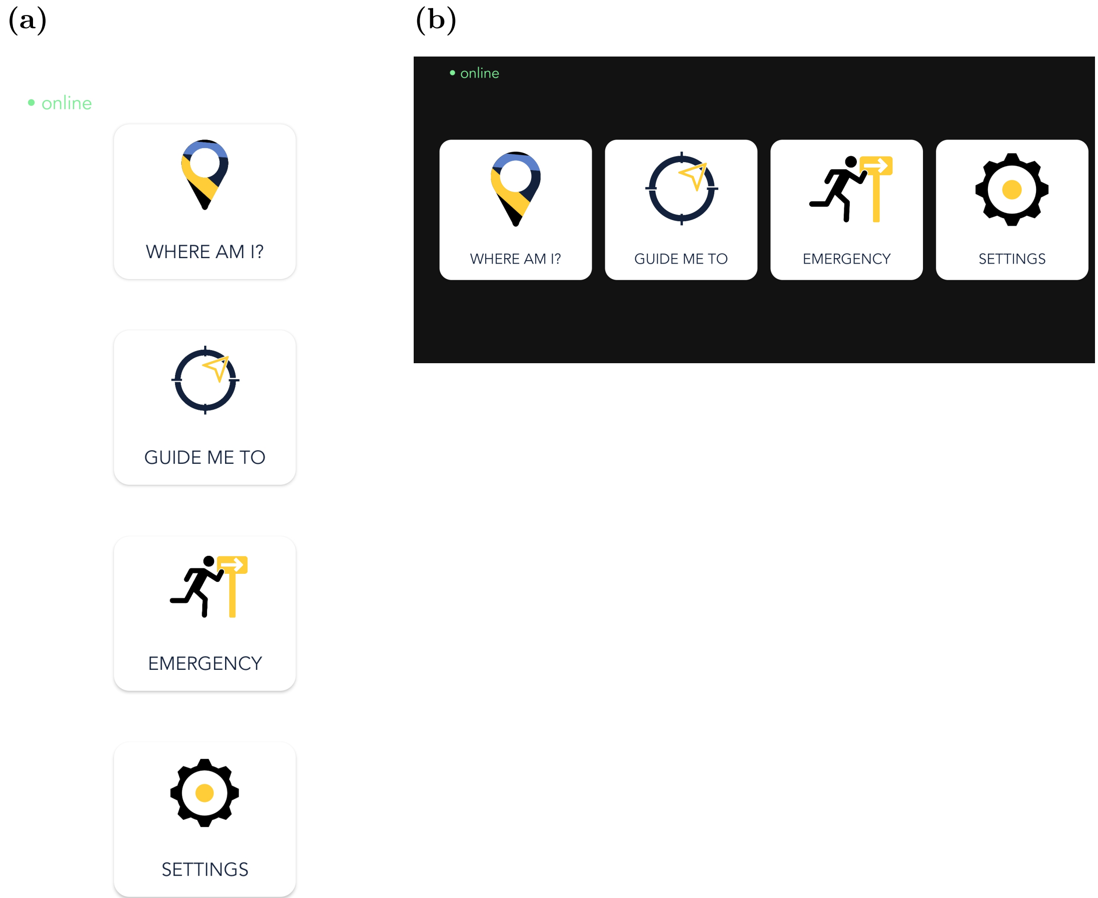

Figure 5.20: Main Menu screen.

If the user select the "Where am I?" option, the system will prompt a map of where the user is. In the map the user will be located with a floating location symbol that the application move depending on the received optical information. The optical information also have the relevant surroundings information that will also be shown to the user in a list with the title "near me" as shown in Fig. 5.21. The user can select any of the listed information and the system will guide the user to the new location (directions screen Fig. 5.23).

If no device is connected, the application will display a message indicating that the location information will not be available until a compatible BLE device is connected. As in the main screen, the user can access the near device list by simply touching the offline status message. The user can return to the main screen at any moment by touching the **back** button.

(a)

(b)

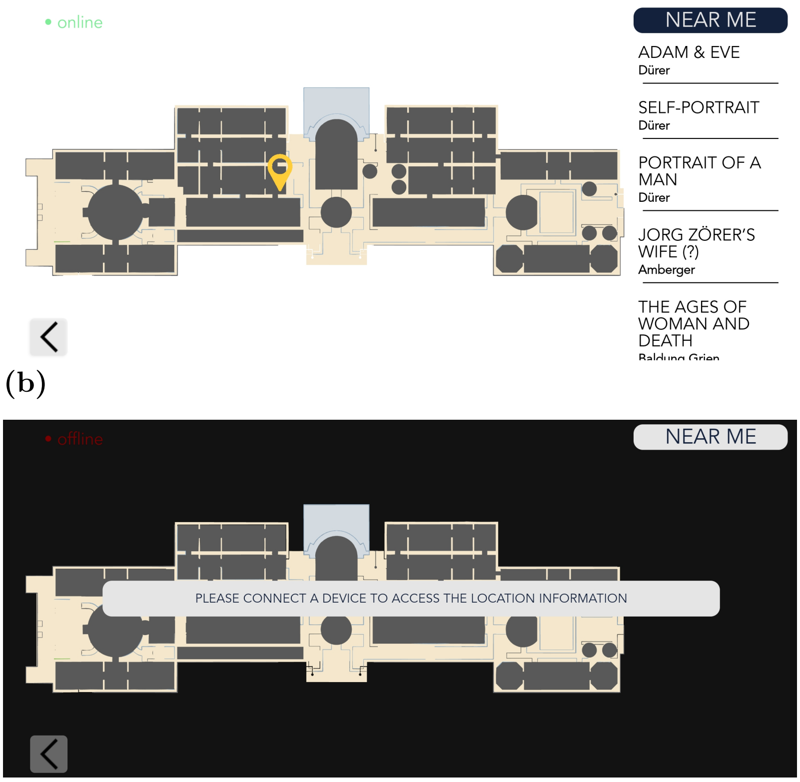

Figure 5.21: "Where am I?" screen.

If the user select the "Guide me to" option, the system show a map with the actual location of the user and a search bar where the user can type the location where he want to go as shown in Fig. 5.22. The system then guide the user to the new location obtaining the information from the beacons that the user is pasing by. When the user reach the new location the system will automatically redirect him to the "Where am I?" screen Fig. 5.21 where the user can find himself in the map and acces to near information. The user can return to the main screen at any moment by touching the **back** button.

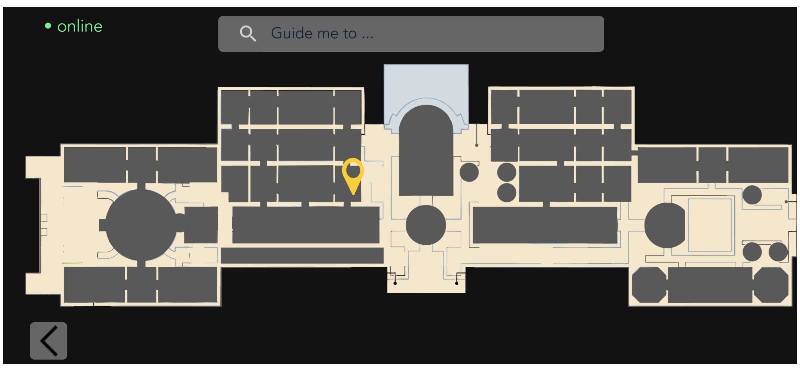

Figure 5.22: "Guide me to" screen.

When the user selects the "Emergency" option, the system automatically takes the user to the directions screen. The system will guide the user from any location to the nearest emergency exit or staging area. The directions screen displays arrows indicating the path, as shown in Fig. 5.23, and is updated when the user passes under a beacon; the information is also communicated to the user by sound. A small map in the upper right corner shows the user's location and the estimated route. The user can end the guide at any time by pressing the **back** button, which will return the user to the main screen.

(a)

(b)

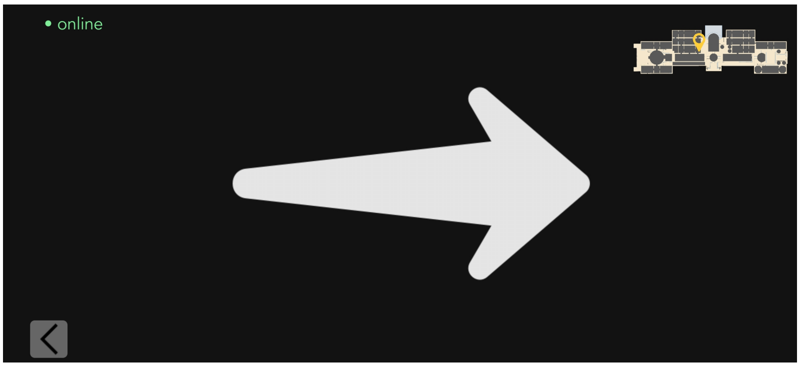

Figure 5.23: Directions screen.

With the previous three options, the user can access all the information that the application can offer with VLC localization, but the system, needs to be configurable, and therefore there is a need for a settings screen. In the settings, the user will be able to change the accessibility method, the application language, pair a BLE device, or enable/disable notifications. In the *BLuetooth Device* option, the user can see the currently connected device, if any, and can disconnect it by pressing the **unpair** button. On the other hand, if no device is connected, the system offers a **pair** button that will redirect the user to the device screen to select a compatible one to connect to. Also, the notifications will allow the system to open the application when a AR device is connected through the USB-C port of the device.

If the device is going to be used by a new user, the settings screen offers a **reset** button that will clear all the settings preferences and will return the user to the preferences screen (Fig. 5.18) as if the application is running for the first time, following all the process previously described.

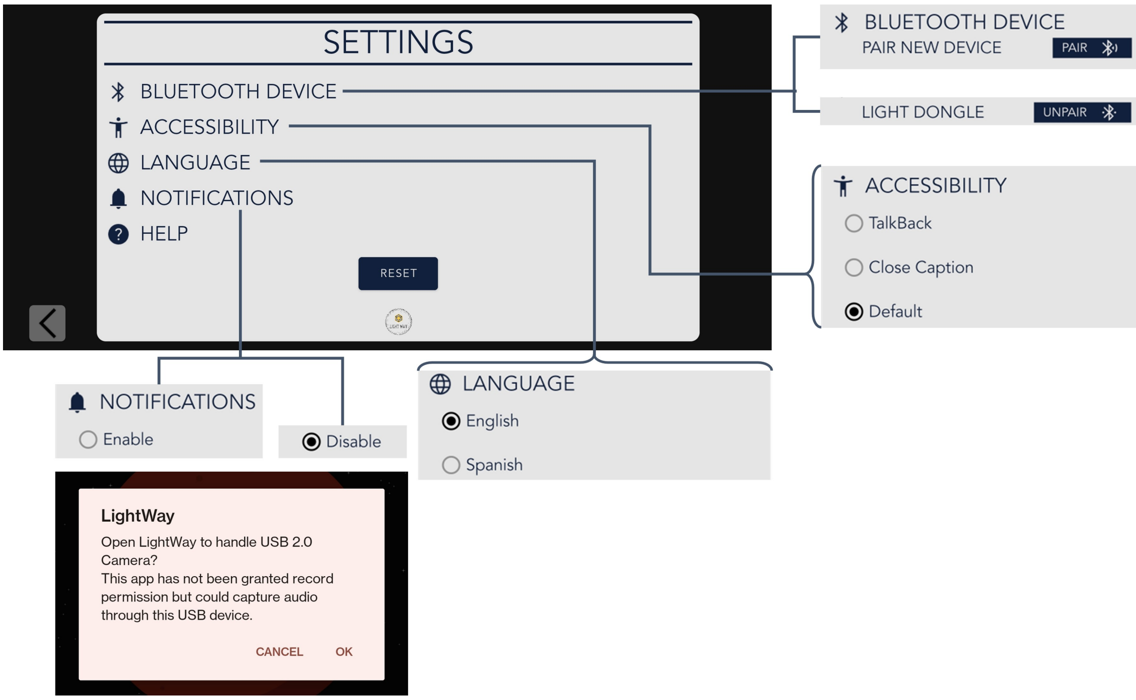

Figure 5.24: "Settings" screen.

5.4. System Characteristics

Once all the elements (transmitter, receiver, and mobile application) were developed, the system was tested to measure the limits of its functionality. First, we measure the lux emitted by each of the different lamps constructed and its variation over distance. For this experiment, the measurements were made with the Mavolux 5032 c USB luxmeter from Gossen.

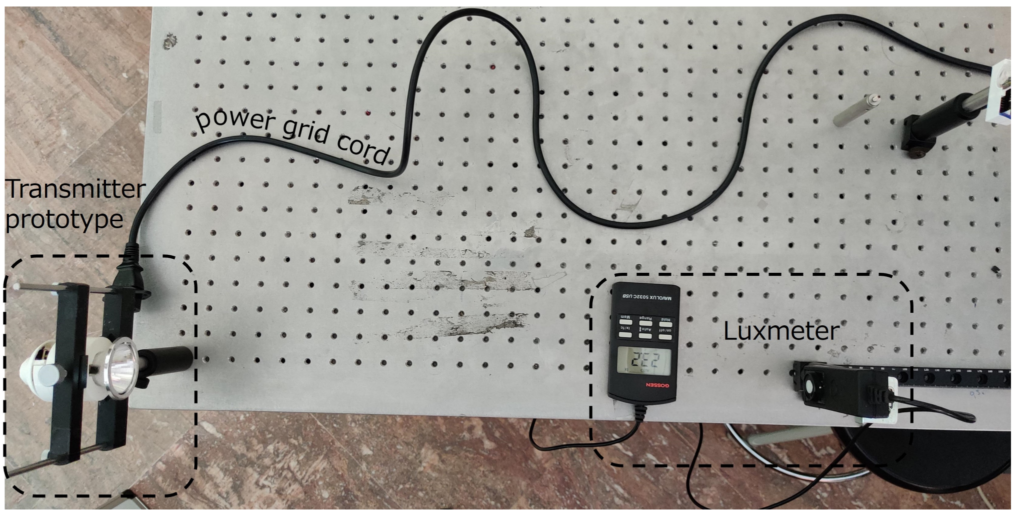

Figure 5.25: Experimental setup for the lux measurements.

The transmitter, already packaged as shown in Fig. 5.8, with the reflector F15558 MIRELLA-G2-S coupled to the LED, is mounted in a static position on an optical table and aligned with the center of the sensitive area of the luxmeter. The luxmeter, on the other hand, is also mounted on the optical table via a riel to perform the distance measurements, as shown in Fig. 5.25.

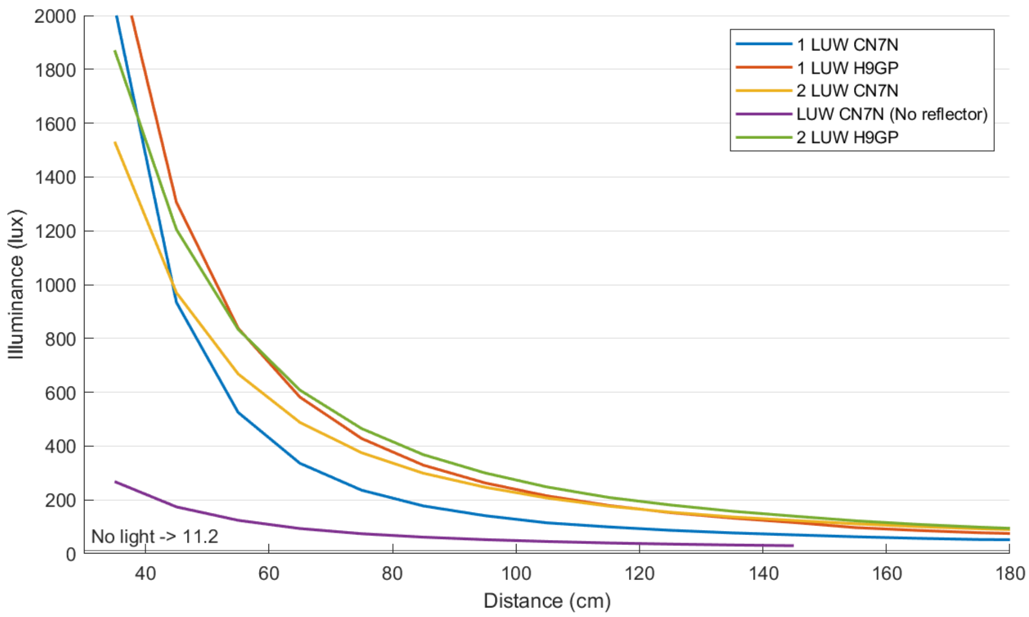

Figure 5.26: Illuminance evolution at different distances for multiple LED configurations.

From the experimental results, it can be seen that the LEDs LUW-H9GP provides more illumination than the LUW-CN7N for the same distance and configuration. In addition, the amount of light reaching the luxmeter is very low when no reflector is coupled to the LEDs. The behavior of all the measurements fits the expected as the illumination intensity on a surface is inversely proportional to the square of its distance from the light source.

Following the same configuration shown in Fig. 5.25 and replacing the luxmeter with the receiver, the received signal is measured at two points. One is after the trans-impedance stage, which is the analog signal, and the other is after the comparator, which is the signal to be fed into the GPIO. These two measurement points are shown in Fig. 5.9. The measured frequency is no longer the maximum that the transmitter can offer (260 kHz) but the maximum that the receiver SoC can sample without error, which is 233.7 kHz. The measurements were perform with the oscilloscope and without the receiver SoC connected and with the transmitter that contain two LUW-CN7N LEDs.

The maximum distance where the signal can be measured at the comparator output was 170 cm, which is sufficient for the target applications of this prototype. Likewise, the system has a minimum operating distance at which the received signal is large enough to saturate the receiver elements; in this case, this minimum distance

(a) Compared digital output (b) TIA analog output

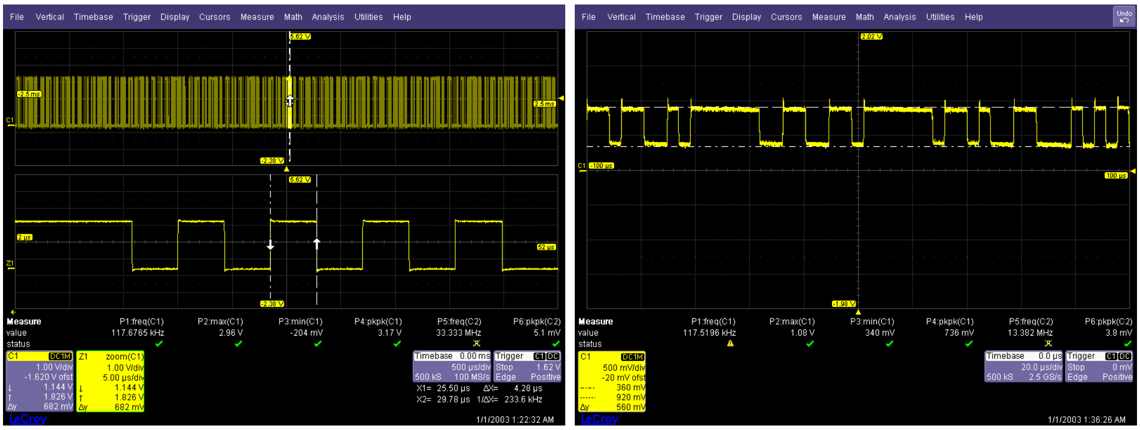

Figure 5.27: Measurements taken with the receiver at a distance of 40 cm from the transmitter.

(a) Compared digital output (b) TIA analog output

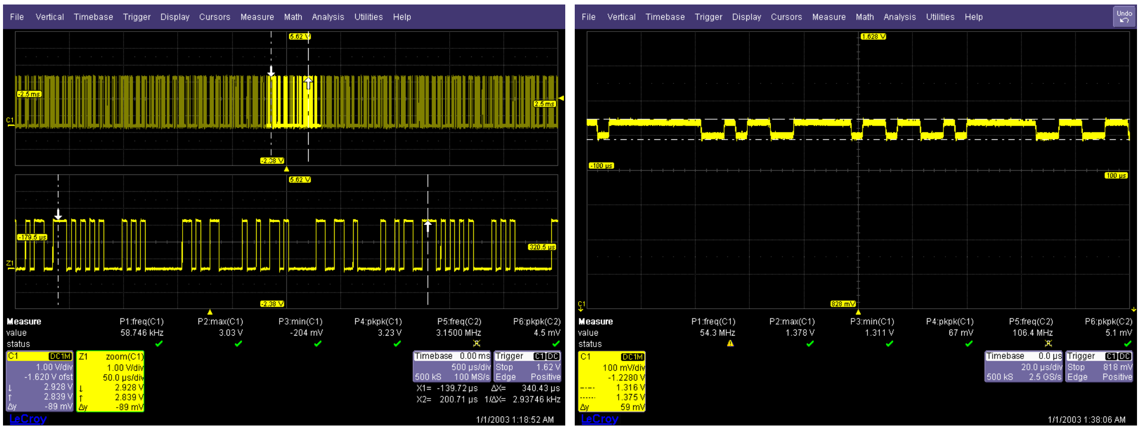

Figure 5.28: Measurements taken with the receiver at a distance of 157 cm from the transmitter.

is reached at 27.5 cm, resulting in an effective operating distance of 142.5 cm. The minimum and maximum working distances were tested with the oscilloscope and also with the received BLE signal.

Then, after verifying that the transmitted signal is well received and defining the range of distances within which the receiver will respond to the transmitter variations, the SoC is put in place. This is used to test that the collection and transmission of the data is done correctly. Using the defined frame structure and known data, we compared the received messages with the transmitted ones. To do this, we used two applications, one available in the Play Store called LightBlue developed by "Punch Through Design", which allows to access all the related information of a BLE device, including reading the characteristic values, and the other developed by us, which also retrieves all the related information of the device and allows to subscribe to a characteristic. This last application also allows us to plot the received data to make them easily comparable with the expected wave.

(a) (b) (c) (d)

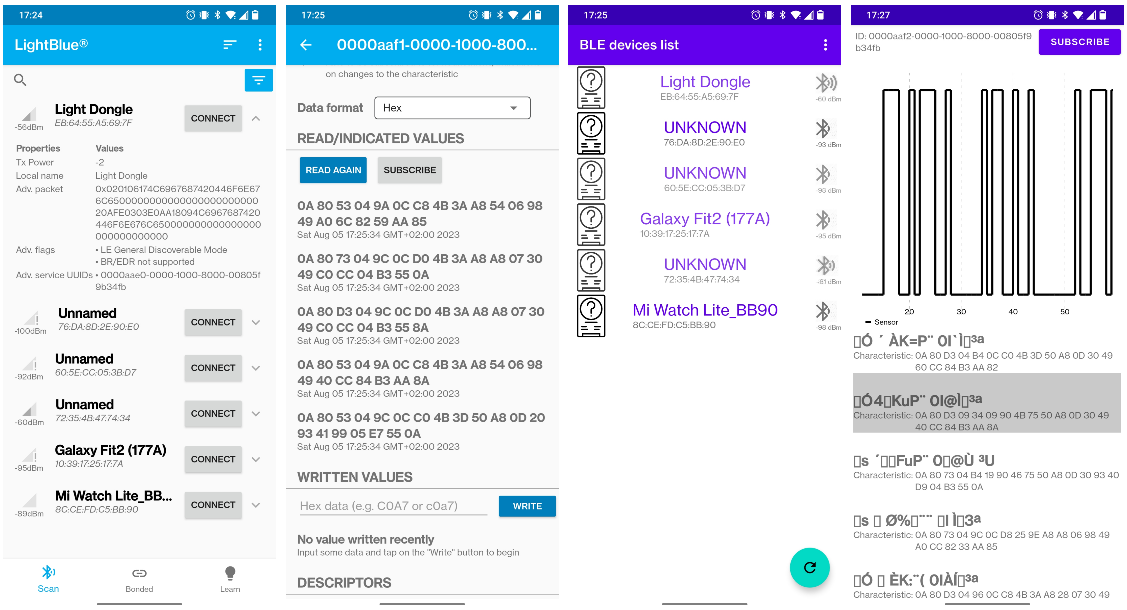

Figure 5.29: LightBlue (a) device identification and (b) data collection and BLE plot (own application) (c) device identification and (d) data collection and plot.

To retrieve the received data from the hex values displayed by the LightBlue application, we take screen captures and pass them through a Optical Character Recognition (OCR) and then compare the resulting bits with the one sent. All this code was written in the Phyton language using the **pytesseract** library as the OCR.

From this data comparison, it was noticed that the system was missing a bit once in a time, which caused a shift in all subsequent information received. In other words, the system ignores one bit every 20 or 40 bytes, but this has a significant effect on the bits that follow. This problem occurs because the sampling clock and transmission clock are not perfectly synchronized. In this prototype, the sampling frequency was adjusted to the instruction time in the main loop, and the transmitter frequency was performed by an internal clock interrupt. But at the transmitter, depending on whether the packet is encoded or not, the instructions that the system takes to update the new data to be transmitted change, causing a small drift in the transmission clock. This time drift is large enough to miss a bit or to sample the same bit twice.

To overcome this, the system can operate at two different communication rates. One, the previously mentioned, operates at nearly 234 kbps but has the bit-slip problem, requiring smaller packages and some resynchronization bits, and the other operates at 118 kbps and is synchronized to the sampling frequency, ensuring two samples per bit and therefore avoiding the missing of bits.

In summary, the system integrates a variety of technologies and tools to provide

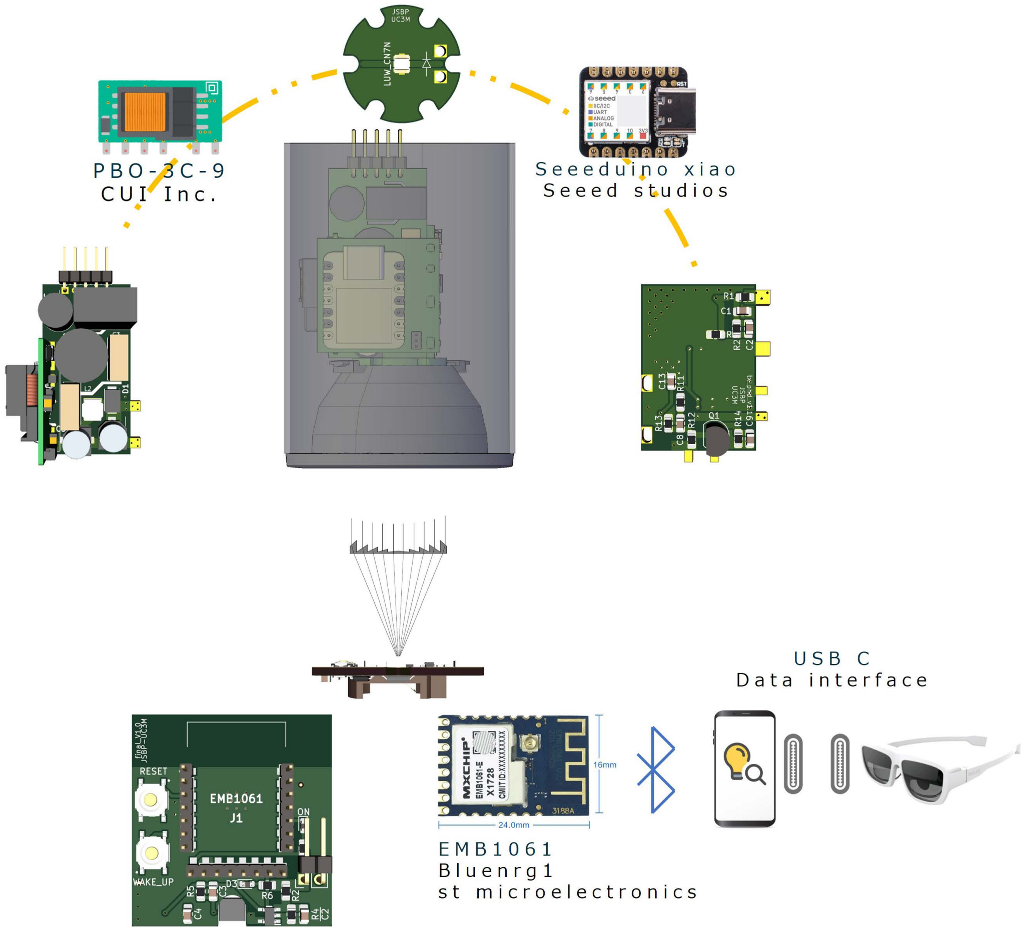

Figure 5.30: Prototype system diagram.

a solution with smooth user interaction. The system, in a nutshell, is shown in Fig. 5.30, where all the different elements of the transmitter, receiver, and smart device can be seen. The smartphone can be easily replaced by any device that supports Android OS in the context of this prototype. But VLC system integration with other types of OS is completely feasible, as it is only necessary that the device supports BLE to develop a high-level application that captures the Bluetooth information and presents it to the user in a useful way. The different elements shown in Fig. 5.30 are modular, which means that if an update of one or more modules is needed, the rest can be left unchanged, and the system will work as expected.

5.4.1. Applications

The prototype supports multiple location applications. The system is flexible enough to allow for different site maps and beacon assignments. An initial setup process is required to define the information that each beacon will transmit and the location associated with the lamp identifier. This could be done by the administrator using a management application, but it is beyond the scope of this solution. Each time the solution is deployed in a new location, administrators must provide the maps to be placed in the navigation application.

The receivers are plug-and-play, do not require any configuration by the user, and it is enough to turn them on and walk under a beacon to start interacting with the environment. This allows the solution to be used by any person, even with sensory disabilities, and to work effectively for any user. The initial configuration allows the system to adapt to the user's needs, making the application easy and practical to use. The idea is to bring all the functionalities that the user needs while leaving the VLC behind the scene.

In this context, the prototype will be suitable for large indoor environments where the localization of the user plays a key role in the interaction with the environment. A good example could be a museum, as shown in the screenshots of the application. In the museum, the location information will make the visit more enjoyable, allowing the user to maximize the things that are of interest to them and allowing them to notice new things. It also makes the guides more accessible since there is no need to interact with the device to get information about the surroundings, such as an explanation of the painter's work inspiration or history.

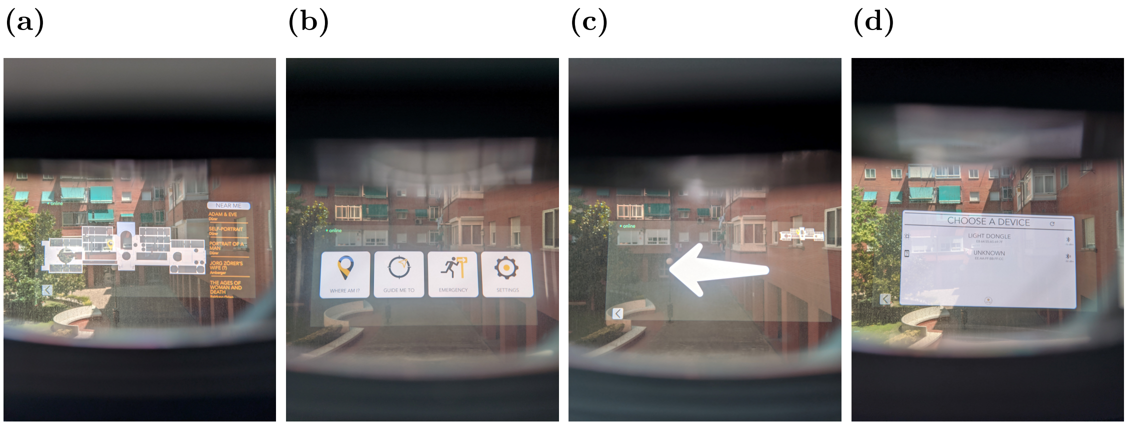

Figure 5.31: Capture of what the user sees through the AR glasses (a) on the "Where am I" screen, (b) on the Menu screen, (c) on the Directions screen, and (d) on the Device selection screen.

Another good scenario could be a shopping mall, where the user can be guided to the desired stores, saving time and even offering the user special local promotions. This prototype can also work in supermarkets where the item location varies from one to another and sometimes difficult the shopping process. Since the application also has TalkBack, visually impaired people can easily locate any product they want, making the shopping experience as smooth as possible.

The system also supports AR glasses, which opens up application possibilities. In the case of this prototype, the glasses are used to guide the user to his desired destination, making it easy to interact with the environment while receiving the information, as shown in Fig. 5.31. But the limit is not there, AR can offer to target information to each user, enriching his experience. Also, the information can be transformed in a way that each person can receive it, e.g., a deaf person can access all the supermarket messages on his screen or, in a museum, he can receive all the guide information in text or animated images, improving his experience and closing the information access gap.

6 Final Conclusions and Future Work

"There is no real ending. It's just the place where you stop the story."

Frank Herbert

6.1. Conclusions

The interest in VLC technology increased significantly, at first in a theoretical approach, but day by day, it is changing into a practical technology that is not a substitute for the current wireless technologies but a potentiator; working as a secure, confined, and electromagnetic interference-free complementary communication channel that contributes to the development of other concepts such as IoT, Smart Cities, Accessible Cities, and Indoor Localization among others. Therefore, this thesis work is oriented to design and develop a working VLC prototype that is able to receive data through visible light and use this data to offer quality information to the end user.

However, LEDs manufacturers and distributors focus on the lighting qualities (static parameters) of the product as it is intended for that purpose. As a result, information on the dynamic capabilities of the LEDs is rare and, in most cases, non-existent. Taking this into account, in chapter 2, we have proposed a method that allows the electrical characterization of high-power phosphor-based white LEDs, resulting in useful information about the electrical behavior of the LEDs and the formulation of an equivalent electrical circuit that can be used, for example, in the simulation of LED equalization circuits. The equalization process is the key to exploding the maximum frequency capabilities of the device, resulting in more bandwidth. Yet, since the electrical bandwidth of the LEDs is much higher than the optical bandwidth, it can be said that the bandwidth limitation of the white phosphor-based LEDs is not electrical but optical.

Another important aspect to make the prototype a reality is the modulation format to be used. The modulation format will determine how the transmitter will encode the data but also how resistant that data will be to the noise induced by the unguided channel. Thus, the modulated format chosen for this system is NRZ-OOK because it offers a very high bandwidth efficiency with a relatively simple and low resource-consuming implementation. This modulation is susceptible to ISI, and this problem is exacerbated when non-LoS signals are large enough to deform the transmitted symbol. But in the case of this prototype and its intended applications, since the light source has a low illumination level, the effect of non-LoS signals in the received data can be neglected. Also, since the bandwidth of the LED used (1.5 MHz without equalization) is several times greater than the communication speed (234 kbps), the square shape of the symbols is not lost, allowing better recovery at the receiver end.

Although we choose NRZ-OOK as the modulation format for this prototype, we also explore other types of modulation formats that may be more appropriate in other implementations where computational resources are not a constraint and the system seeks to achieve maximum transmission speed while keeping BER to a minimum. It is the case with OFDM modulation. However, even though this modulation format is well known and has been implemented in other wireless channels, its implementation on VLC channels requires adaptation to the specificities of visible light communication. In this matter, in chapter 3, we explore the challenges of the time synchronization process when the transmitted signal must be purely real, and a phase estimation and correction that fits best the constellation behavior at the receiver side in a VLC channel. The time synchronization process is achieved post-FFT with an accuracy of 99.99% of the received packets in an OFDM system with hermitian symmetry, tested not only in simulation with synthetic data but also in a real working VLC system. The same applies to the phase estimation and correction, where the addition of a deterministic noise in the phase shift estimation together with a non-deterministic noise induced by the channel and the clock shift leads to a better recovery of the information. With this method, the BER of the system was reduced by almost half (from 0.058% with the classical implementation to 0.028% with our proposed equation).

However, even if the non-LoS paths can cause errors in the received bits, their effect on the communication itself is not always negative. Let us explain this in more detail. In OWC, the main constraint that limits the flexibility of the communication is the necessity of a LoS path between sender and receiver, which makes this kind of communication very susceptible to obstacles. Here is where the non-LoS information becomes relevant because when the LoS path is blocked, the only way to receive the transmitted information is through reflections. In this way, researchers have found in IRSs a way to optimize the non-LoS path to make it as efficient as the LoS path. In chapter 4, we explore analysis to evaluate the performance of a micromirror based IRS in FSO. Unlike VLC, FSO uses LASERs instead of LEDs, which changes the shape of the wavefront, being a Gaussian or Lambertian distribution, respectively. In the case study, an evaluation of the performance of the IRS as a function of the size of the mirrors and the gap between them while keeping the total size of the IRS constant suggests that not always the smaller the elements, the better. There is an efficient point where the ratio of the element gap to the element size reaches the maximum redirection of power to the receiver. This type of surface can be translated to VLC applications but requires further exploration since VLC channels have different characteristics than FSO, e.g., the link distance, the beam aperture, the amount of energy, among others.

Finally, with all the knowledge gained in exploring the different elements that play a role in a VLC channel, we have enough tools to develop our own prototype. The benefits of doing an actual implementation of a complete VLC system, going through how hardware, firmware, and software are concurrently designed and implemented, help to identify challenges that can only be seen in a practical implementation, resulting in an enriched knowledge and higher impact. In chapter 5, we went through all the stages of design. First, we focused on the hardware, as it is the base on which the rest of the prototype layers are built. On the transmitter side, the LED is the element that limits the maximum speed achievable, mainly because the maximum bandwidth of the device without any equalization process is only 1.5 Mhz, which may be enough for IoT applications but is a limit for applications with high data requirements such as video transmission. It is worth mentioning that the phosphor layer of the white LED has a lot to do with this bandwidth, as its reconversion time is lower than that of the blue LED itself. Yet, filtering out the yellow component of the received light will reduce the total power, which is not desirable in low-output power applications. In this way, we designed and implemented an equalization circuit that extends the transmission bandwidth up to 20 MHz. The design of the transmitter is modular so that the power supply, the driver stage, or the LEDs can be easily changed. To verify that, the transmitter was tested with two different LEDs with one or two LEDs per PCB. The selected microcontroller must be able to handle all the data processing to encode and structure the packets to be sent. This element can be connected to a data source, or it can be configured offline, which means that the information sent is static, but not that the information representation on the receiver side must always be the same. In the case of this prototype, we implement an offline configuration that demonstrates that this configuration is flexible enough to be used in a variety of solutions, requiring only an initial setup. The maximum transmission speed of this prototype was about 260 kHz, which is less than the maximum capabilities of the LED. Therefore in our implementation, the limit was the maximum speed at which the microcontroller could switch a GPIO while performing data management and not the physical limit of the LED.

Something similar happened on the receiver side. The photodetector, responsible for converting the received light into an electrical signal, is not the bandwidth limiter. In this case, since the receiver needs to be powered by a small battery, power consumption, and size were major constraints. Therefore, we designed two alternatives, one with a powerful amplifier that has a GBW of 1.8 GHz and introduces low noise to the signal, allowing a higher gain while ensuring a large bandwidth at the expense of power consumption, or the other that is cheaper and has a low power consumption but offers only 18 MHz of GBW. In any case, the chosen amplifiers are pin compatible, so we can have a design that will work differently depending on the elements chosen. The final maximum transmission speed achieved with the entire system was 234 kbps (but the packet size must be kept small as it suffers from bit-slip). The system can also be configured to operate at 118 kbps (where the system does not lose a bit of information). The prototype also let us know that the post-processing of the data does not need to be performed strictly in the receiver SoC, but it can be passed to a more powerful unit afterward, as in this case is the smart device.

The implemented prototype demonstrates that VLC can be used alongside other technologies to bring new solutions to the market. The prototype integrates multiple technologies such as VLC, AR, BLE, and smart devices, suggesting that VLC solutions will require a multidisciplinary focus to reach and cover user needs. It is also noteworthy that VLC based solutions open a new alternative in terms of indoor localization and destination information and can help make indoor environments more accessible to everyone.

6.2. Future Work

It is clear that the prototype is still in the early stages of an actual product and therefore requires more testing and the involvement of users with different needs to test the solution in real scenarios. That said, we have some clear lines in which the researchers can use this work to continue to gain knowledge and mature the system to make it a viable product.

VLC transmitters require support for high-resolution dimming methods to maintain illumination levels when no data is being transmitted and to avoid flickering when the communication state is idle. In the case of this prototype, the information is transmitted continuously, so there is no need for this pattern, but it limits the transmitter's flexibility. Continuing with the transmitter, the prototype was focused on developing a light bulb that is directly connected to the power line and has the communication microcontroller built in, but in most cases, the LED will already be in place, and it is not necessary to have a new bulb. In these cases, it might be interesting to create an element that is directly connected to the lamps and modulates the emitted light.

Even if the final size of both receiver and transmitter is small, the transmitter, for example, is not yet the size of commercial LED bulbs. The receiver could also be made smaller by changing the lens to one with a shorter focal length or even by exploring the implementation of photodetectors with built-in lenses. The receiver PCB could also be replaced with a flexible one, making the user adaptation better since the receiver element can be attached to any available surface without changing the aesthetics. As more researchers and companies are interested in VLC, the market is evolving to create new types of photodiodes, not only sensitive to IR but also PDs that are more sensitive to the blue wavelength. Therefore, the prototype should be tested with other types of PDs that are likely to increase the received signal, making it suitable for applications at greater distances or applications with lower illumination levels. Currently, the developed VLC receiver only supports BLE connection to the user terminal. At least support for a USB-C connection, which can be used for both data transfer and charging, should be added.

Regarding the power source, in this prototype, we use a CR2032 battery which is not rechargeable. The EMB1061 SoC implements capabilities for battery monitoring, so it will be interesting to replace the coin battery with a lithium battery that can be recharged and the battery level can be transmitted to the smart device through BLE to keep the user updated. In addition, the EMB1061 SoC can be replaced with a custom one that better meets the receiver's needs and leaves out the elements that are not needed. This will significantly reduce the size and improve the performance of the receiver, allowing the exploration of new options, such as integrating the receiver into the frame of AR glasses or a headset. However, the cost of development will be high in the early stages.

In terms of high-level application, it can be designed an application for administrators. This application will allow to assign and modify the information associated with the receiver data. In this way, there is no need to change the code built into the lamp, it is enough to update the associated value on a server, and when any user receives the data contained in a lamp, the application will retrieve the desired information. On the other hand, the AR experience can be enhanced by adding support for hand gestures to interact with the application. This is an element that most AR glasses companies include in their Application Programming Interface (API). Indoor localization can be improved by using the integrated Inertial Measurement Unit (IMU) to provide directional information as well; in addition, most AR glasses contain their own IMU that can track the user's visual orientation and thus provide more specific information about what is being viewed.

Bibliography

[1] Cisco, "Cisco annual internet report," Cisco, Tech. Rep., 2020.

[2] M. A. Khalighi and M. Uysal, "Survey on free space optical communication: A communication theory perspective," *IEEE Communications Surveys & Tutorials*, vol. 16, no. 4, pp. 2231–2258, 2014.

[3] P. Warnke, K. Cuhls, U. Schmoch, L. Daniel, L. Andreescu, B. Dragomir, R. Gheorghiu, C. Baboschi, A. Curaj, M. Parkkinen, and et al., *100 Radical innovation breakthroughs for the future*. European Commission EC, 2019. [Online]. Available: https://publica.fraunhofer.de/handle/publica/299710

[4] L. E. M. Matheus, A. B. Vieira, L. F. M. Vieira, M. A. M. Vieira, and O. Gnawali, "Visible light communication: Concepts, applications and challenges," *IEEE Communications Surveys & Tutorials*, vol. 21, no. 4, pp. 3204–3237, 2019.

[5] A. Steiner and N. Ishii, "The rapid transition to energy efficient lighting: An integrated policy approach," The United Nations Environment Programme, Tech. Rep., 2013.

[6] H. Haas, J. Elmirghani, and I. White, "Optical wireless communication," *Philos Trans A Math Phys Eng Sci*, vol. 378, no. 2169, p. 20200051, Mar. 2020.

[7] N. T. Le, M. Hossain, and Y. M. Jang, "A survey of design and implementation for optical camera communication," *Signal Processing: Image Communication*, vol. 53, pp. 95–109, 2017. [Online]. Available: https://www.sciencedirect.com/science/article/pii/S0923596517300188

[8] M. A. S. Sejan and W.-Y. Chung, "Secure vlc for wide-area indoor iot connectivity," *IEEE Internet of Things Journal*, vol. 10, no. 1, pp. 180–193, 2022.

[9] S. Fuada, E. Setiawan, T. Adiono, and W. O. Popoola, "Design and verification of soc for ofdm-based visible light communication transceiver systems and integration with off-the-shelf analog front-end," *Optik*, vol. 258, p. 168867, 2022. [Online]. Available: https://www.sciencedirect.com/science/article/pii/S0030402622002601

[10] pureLiFi, "Lifi-xc," https://www.purelifi.com/products/lifi-xc/, 2019, [Accessed 07-Jul-2023].

[11] H. Le Minh, D. O'Brien, G. Faulkner, L. Zeng, K. Lee, D. Jung, Y. Oh, and E. T. Won, "100-mb/s nrz visible light communications using a postequalized white led," *IEEE Photonics Technology Letters*, vol. 21, no. 15, pp. 1063–1065, 2009.

[12] O. R. B. Sayco and A. C. Gordillo, "Design and implementation for a usrp–based visible light communications transceiver," in *2019 UNSA International Symposium on Communications (UNSA ISCOMM)*. IEEE, 2019, pp. 1–5.

[13] R. Martinek, L. Danys, and R. Jaros, "Visible light communication system based on software defined radio: Performance study of intelligent transportation and indoor applications," *Electronics*, vol. 8, no. 4, p. 433, 2019.

[14] J. Torres, A. Montes, S. Mendoza, P. Fernández, J. S. Betancourt Perlaza, L. Escandell Varela, C. del Valle, and J. Sánchez-Pena, "A low-cost visible light positioning system for indoor positioning," *Sensors*, vol. 20, p. 5145, 09 2020.

[15] A. Galisteo, D. Juara, Q. Wang, and D. Giustiniano, "Openvlc1.2: Achieving higher throughput in low-end visible light communication networks," in *2018 14th Annual Conference on Wireless On-demand Network Systems and Services (WONS)*, 2018, pp. 117–120.

[16] E. F. Schubert, *Light-Emitting Diodes*, 2nd ed. Cambridge University Press, 2006.

[17] A. G. Bell, "On the production and reproduction of sound by light," *American Journal of Science*, vol. 20, no. 118, pp. 305–324, Oct. 1880.

[18] Statista, "Number of internet of things (iot) connected devices worldwide from 2019 to 2021, with forecasts from 2022 to 2030," https://www.statista.com/statistics/607716/worldwide-artificial-intelligence-market-revenues/ last accessed 4 Feb. 2020, 2022.

[19] V. Georlette, S. Bette, S. Brohez, R. Pérez-JIménez, N. Point, and V. Moeyaert, "Outdoor visible light communication channel modeling under smoke conditions and analogy with fog conditions," *Optics*, vol. 1, pp. 259–281, 11 2020.

[20] R. L. Boylestad and L. Nashelsky, *Electronic devices and circuit theory*, 2nd ed. New York, NY SE -: Prentice-Hall and Englewood Cliffs, N.J., 1978.

[21] M. Auf der Maur, K. Lorenz, and A. Di Carlo, "Band gap engineering approaches to increase ingan/gan led efficiency," *Optical and Quantum*

Electronics, vol. 44, no. 3, pp. 83–88, Jun 2012. [Online]. Available: https://doi.org/10.1007/s11082-011-9536-x

[22] J. W. Precker, "Simple experimental verification of the relation between the band-gap energy and the energy of photons emitted by leds," *European Journal of Physics*, vol. 28, no. 3, p. 493, mar 2007. [Online]. Available: https://dx.doi.org/10.1088/0143-0807/28/3/010

[23] M.-H. Chang, D. Das, P. Varde, and M. Pecht, "Light emitting diodes reliability review," *Microelectronics Reliability*, vol. 52, no. 5, pp. 762–782, 2012, reliability of High-Power LED Packaging and Assembly. [Online]. Available: https://www.sciencedirect.com/science/article/pii/S0026271411003283

[24] B. E. A. Saleh and M. C. Teich, *Fundamentals of photonics*, 3rd ed., ser. Wiley series in pure and applied optics. Hoboken, NJ: Wiley, 2019.

[25] A. French, *An Introduction to Quantum Physics*. CRC Press, 2018. [Online]. Available: https://books.google.es/books?id=NlUPEAAAQBAJ

[26] Z. Ghassemlooy, L. Nero Alves, S. Zvanovec, and M. A. Khalighi, *Visible light communications : theory and applications*. Boca Raton, FL: CRC Press, Taylor & Francis Group, 2017.

[27] S. Muthu, F. Schuurmans, and M. Pashley, "Red, green, and blue leds for white light illumination," *IEEE Journal of Selected Topics in Quantum Electronics*, vol. 8, no. 2, pp. 333–338, 2002.

[28] S. Pimputkar, J. S. Speck, S. P. DenBaars, and S. Nakamura, "Prospects for led lighting," *Nature Photonics*, vol. 3, no. 4, pp. 180–182, Apr 2009. [Online]. Available: https://doi.org/10.1038/nphoton.2009.32

[29] C. Wang, H.-Y. Yu, and Y.-J. Zhu, "A long distance underwater visible light communication system with single photon avalanche diode," *IEEE Photonics Journal*, vol. 8, no. 5, pp. 1–11, 2016.

[30] S. Dimitrov and H. Haas, *Optical wireless communication*. Cambridge University Press, 2015, pp. 12–56.

[31] T. P. Lee, "Effect of junction capacitance on the rise time of led's and on the turn-on delay of injection lasers," *The Bell System Technical Journal*, vol. 54, no. 1, pp. 53–68, 1975.

[32] S. W. R. Lee, *From LED to Solid State Lighting: Principles, Mate rials, Packaging, Characterization, and Applicatio ns: Principles, materials, packaging, characterization, and applications*. Nashville, TN: John Wiley & Sons, 2021.

[33] X. Li, Z. Ghassemlooy, S. Zvanovec, M. Zhang, and A. Burton, "Equivalent circuit model of high power leds for vlc systems," in *2019 2nd West Asian Colloquium on Optical Wireless Communications (WACOWC)*, 2019, pp. 90–95.

[34] S. C. Tokgoz, N. Anous, S. Yarkan, D. Khalil, and K. A. Qaraqe, "Performance improvement of white led-based vlc systems using blue and flattening filters," in *2019 International Conference on Advanced Communication Technologies and Networking (CommNet)*, 2019, pp. 1–6.

[35] J. Grubor, S. C. J. Lee, K.-D. Langer, T. Koonen, and J. W. Walewski, "Wireless high-speed data transmission with phosphorescent white-light leds," in *33rd European Conference and Exhibition of Optical Communication - Post-Deadline Papers (published 2008)*, 2007, pp. 1–2.

[36] S.-W. Wang, F. Chen, L. Liang, S. He, Y. Wang, X. Chen, and W. Lu, "A high-performance blue filter for a white-led-based visible light communication system," *IEEE Wireless Communications*, vol. 22, no. 2, pp. 61–67, 2015.

[37] E. M. Hussein, "Chapter one - mechanisms," in *Radiation Mechanics*, E. M. Hussein, Ed. Oxford: Elsevier Science Ltd, 2007, pp. 1–65. [Online]. Available: https://www.sciencedirect.com/science/article/pii/B9780080450537500021

[38] T. Santhanakrishnan, H. Devassy, and A. S. Chandrakanta, "Exploiting the non-uniform characteristics of silicon photodiode in vibration monitoring," in *2020 IEEE 4th Conference on Information & Communication Technology (CICT)*, 2020, pp. 1–6.

[39] F.-M. Wu, C.-T. Lin, C.-C. Wei, C.-W. Chen, H.-T. Huang, and C.-H. Ho, "1.1-gb/s white-led-based visible light communication employing carrier-less amplitude and phase modulation," *IEEE Photonics Technology Letters*, vol. 24, no. 19, pp. 1730–1732, 2012.

[40] J. L. Moll, S. Krakauer, and R. Shen, "P-n junction charge-storage diodes," *Proceedings of the IRE*, vol. 50, no. 1, pp. 43–53, 1962.

[41] W. Chen and S. Liu, "Pin avalanche photodiodes model for circuit simulation," *IEEE Journal of Quantum Electronics*, vol. 32, no. 12, pp. 2105–2111, 1996.

[42] J. Kahn and J. Barry, "Wireless infrared communications," *Proceedings of the IEEE*, vol. 85, no. 2, pp. 265–298, 1997.

[43] H. Jiang and P. Yu, "Equivalent circuit analysis of harmonic distortions in photodiode," *IEEE Photonics Technology Letters*, vol. 10, no. 11, pp. 1608–1610, 1998.

[44] H. Corporation, "Si-based Photodiodes," pp. 1–4, 2014.

[45] P. D. S. PHOTODIODE, "Photodiode characteristics and applications."

[46] S. Sze and M. Lee, *Semiconductor Devices: Physics and Technology*, ser. Semiconductor Devices, Physics and Technology. Wiley, 2012. [Online]. Available: https://books.google.es/books?id=RdnjAgAAQBAJ

[47] X. Li, Z. Ghassemlooy, S. Zvanovec, and L. N. Alves, "An equivalent circuit model of a commercial led with an esd protection component for vlc," *IEEE Photonics Technology Letters*, vol. 33, no. 15, pp. 777–779, 2021.

[48] J. S. Betancourt Perlaza, J. C. Torres Zafra, M. Morales Céspedes, I. Martínez-Sarriegui, C. I. del Valle, and J. M. Sánchez Pena, "An enhanced method for dynamic characterization of high-power leds for visible light communication applications," *Electronics*, vol. 11, no. 3, 2022.

[49] S. Zhao, J. Xu, and O. Trescases, "Burst-mode resonant llc converter for an led luminaire with integrated visible light communication for smart buildings," *IEEE Transactions on Power Electronics*, vol. 29, no. 8, pp. 4392–4402, 2014.

[50] F. A. Dahri, F. A. Umrani, A. Baqai, and H. B. Mangrio, "Design and implementation of led–led indoor visible light communication system," *Physical Communication*, vol. 38, p. 100981, 2020. [Online]. Available: https://www.sciencedirect.com/science/article/pii/S187449071930388X

[51] M. Sohail, P. Saengudomlert, and K. Sterckx, "Linear analog current modulation on light emitting diodes in optical wireless communications," in *2014 International Electrical Engineering Congress, iEECON 2014*, 03 2014.

[52] C.-S. A. Gong, Y.-C. Lee, J.-L. Lai, C.-H. Yu, L. R. Huang, and C.-Y. Yang, "The high-efficiency led driver for visible light communication applications," *Scientific Reports*, vol. 6, no. 1, p. 30991, Aug 2016. [Online]. Available: https://doi.org/10.1038/srep30991

[53] J. M and M. Jamro, *Optical Fiber Communications: Principles and Practice*, ser. Prentice Hall Internacional series in optoelectronics. Financial Times/Prentice Hall, 2009. [Online]. Available: https://books.google.es/books?id=7HtqsEOMkXUC

[54] H. Elgala, R. Mesleh, and H. Haas, "A study of led nonlinearity effects on optical wireless transmission using ofdm," in *2009 IFIP International Conference on Wireless and Optical Communications Networks*, 2009, pp. 1–5.

[55] A. Kassem and I. Darwazeh, "A high bandwidth modified regulated cascode tia for high capacitance photodiodes in vlc," in *2019 IEEE International Symposium on Circuits and Systems (ISCAS)*, 2019, pp. 1–5.

[56] L. N. Alves and R. L. Aguiar, "Design techniques for high performance optical wireless front-ends," in *Proceedings of the Conference on Telecommunications-ConfTele*, 2003.

[57] M. Demirtaş, M. A. Erişmiş, and S. Güneş, "Analysis and design of a transimpedance amplifier based front-end circuit for capacitance measurements," *SN Applied Sciences*, vol. 2, no. 2, p. 280, Jan 2020. [Online]. Available: https://doi.org/10.1007/s42452-020-2104-x

[58] T. Wang and B. Erhman, "Compensate transimpedance amplifiers intuitively," Texas Instruments, Tech. Rep. SBOA055A, March 2005.

[59] C. Martinsons, "Photobiological safety," in *Handbook of Advanced Lighting Technology*. Springer, 2017, pp. 865–895.

[60] "Herodotus, The Histories, Book 10, chapter 45, section 6-12," https://www.perseus.tufts.edu/hopper/text?doc=Perseus%3Atext%3A1999.01.0126%3Abook%3D3%3Achapter%3D43%3Asection%3D1, [Accessed 08-Jun-2023].

[61] P. A. V. Oppenheim and P. G. Verghese, "Chapter 12: Pulse amplitude modulation (pam), quadrature amplitude modulation (qam)," in *Introduction To Communication, Control, And Signal Processing*, Cambridge MA, 2010, MIT OpenCourseWare. [Online]. Available: https://ocw.mit.edu/courses/6-011-introduction-to-communication-control-and-signal-processing-spring-2010/d2df3fc906190f978ad666c9c63cdc5d_MIT6_011S10_chap12.pdf

[62] Z. Ghassemlooy, W. Popoola, and S. Rajbhandari, *Optical Wireless Communications: System and Channel Modelling with MATLAB®, Second Edition*. CRC Press, 2019. [Online]. Available: https://books.google.es/books?id=v02WDwAAQBAJ

[63] A. Majumdar, *Advanced Free Space Optics (Fso): A Systems Approach*, ser. The international biological programme. Springer, 2014. [Online]. Available: https://books.google.es/books?id=J2P1sgEACAAJ

[64] Y. Fujiwara, "Self-synchronizing pulse position modulation with error tolerance," *IEEE Transactions on Information Theory*, vol. 59, no. 9, pp. 5352–5362, sep 2013. [Online]. Available: https://doi.org/10.1109%2Ftit.2013.2262094

[65] Y. Fan and R. J. Green, "Comparison of pulse position modulation and pulse width modulation for application in optical communications," *Optical Engineering*, vol. 46, no. 6, p. 065001, 2007. [Online]. Available: https://doi.org/10.1117/1.2746010

[66] J.-H. Yoo, B. W. Kim, and S.-Y. Jung, “Modelling and analysis of m-ary variable pulse position modulation for visible light communications,” *IET Optoelectronics*, vol. 9, no. 5, pp. 184–190, 2015. [Online]. Available: https://doi.org/10.1049/iet-opt.2014.0107

[67] “Ieee standard for local and metropolitan area networks–part 15.7: Short-range wireless optical communication using visible light,” *IEEE Std 802.15.7-2011*, pp. 1–309, 2011.

[68] J.-H. Yoo and S.-Y. Jung, “Modeling and analysis of variable ppm for visible light communications,” *EURASIP Journal on Wireless Communications and Networking*, vol. 2013, no. 1, p. 134, May 2013. [Online]. Available: https://doi.org/10.1186/1687-1499-2013-134

[69] H. Farahneh, F. Hussain, and X. Fernando, “Performance analysis of adaptive OFDM modulation scheme in VLC vehicular communication network in realistic noise environment,” *EURASIP Journal on Wireless Communications and Networking*, vol. 2018, no. 1, p. 243, dec 2018. [Online]. Available: https://jwcn-eurasipjournals.springeropen.com/articles/10.1186/s13638-018-1258-3

[70] C. Jing, X. Tang, X. Zhang, L. Xi, and W. Zhang, “Time domain synchronous ofdm system for optical fiber communications,” *China Communications*, vol. 16, no. 9, pp. 155–164, 2019.

[71] N. J. Jihad and S. M. Abdul Satar, “Performance study of aco-ofdm and dco ofdm in optical camera communication system,” in *2020 2nd Al-Noor International Conference for Science and Technology (NICST)*, 2020, pp. 63–67.

[72] “Ieee standard for information technology–telecommunications and information exchange between systems local and metropolitan area networks–specific requirements part 11: Wireless lan medium access control (mac) and physical layer (phy) specifications,” *IEEE Std 802.11-2012 (Revision of IEEE Std 802.11-2007)*, pp. 1–2793, 2012.

[73] J. Armstrong, “Ofdm for optical communications,” *Journal of Lightwave Technology*, vol. 27, no. 3, pp. 189–204, 2009.

[74] H. Rohling, *OFDM: Concepts for Future Communication Systems*, ser. Signals and Communication Technology. Springer Berlin Heidelberg, 2011. [Online]. Available: https://books.google.es/books?id=r3oD87z4E7UC

[75] C.-R. Sheu and C.-C. Huang, “A novel guard interval based isi-free sampling region detection method for ofdm systems,” in *IEEE 60th Vehicular Technology Conference, 2004. VTC2004-Fall. 2004*, vol. 1, 2004, pp. 515–519 Vol. 1.

[76] S. A. Salehi, R. Amirfattahi, and K. K. Parhi, "Pipelined architectures for real-valued FFT and hermitian-symmetric IFFT with real datapaths," *IEEE Transactions on Circuits and Systems II: Express Briefs*, vol. 60, no. 8, pp. 507–511, 2013.

[77] H. Lin and P. Siohan, "Ofdm/oqam with hermitian symmetry: Design and performance for baseband communication," in *2008 IEEE International Conference on Communications*, 2008, pp. 652–656.

[78] J. S. Betancourt P., R. Lozada Domínguez, and E. San Millan Heredia, "Phase characterization and correction in a hardware implementation of an ofdm-based system for vlc applications," *IEEE Photonics Journal*, vol. 15, no. 2, pp. 1–7, 2023.

[79] X. Ling, J. Wang, X. Liang, Z. Ding, and C. Zhao, "Offset and power optimization for dco-ofdm in visible light communication systems," *IEEE Transactions on Signal Processing*, vol. 64, no. 2, pp. 349–363, 2016.

[80] J. Pradhan, P. Holey, V. K. Kappala, and S. K. Das, "Performance analysis of aco-ofdm noma for vlc communication," *Optical and Quantum Electronics*, vol. 54, no. 8, p. 531, Jul 2022. [Online]. Available: https://doi.org/10.1007/s11082-022-03939-7

[81] D. Tsonev, S. Sinanovic, and H. Haas, "Novel unipolar orthogonal frequency division multiplexing (u-ofdm) for optical wireless," in *2012 IEEE 75th Vehicular Technology Conference (VTC Spring)*, 2012, pp. 1–5.

[82] W. A. Martins, F. Cruz–Roldán, M. Moonen, and P. S. Ramirez Diniz, "Intersymbol and intercarrier interference in ofdm transmissions through highly dispersive channels," in *2019 27th European Signal Processing Conference (EUSIPCO)*, 2019, pp. 1–5.

[83] J. I. Montojo and L. B. Milstein, "Effects of imperfections on the performance of ofdm systems," *IEEE Transactions on Communications*, vol. 57, no. 7, pp. 2060–2070, 2009.

[84] R. Lozada D., J. S. Betancourt P., and E. San Millán H., "Time synchronization technique hardware implementation for ofdm systems with hermitian symmetry for vlc applications," *IEEE Access*, vol. 11, pp. 42 222–42 233, 2023.

[85] M. Sliskovic, "Sampling frequency offset estimation and correction in OFDM systems," *Proceedings of the IEEE International Conference on Electronics, Circuits, and Systems*, vol. 1, no. 1, pp. 437–440, 2001.

[86] P. Xiao, C. Cowan, T. Ratnarajah, and A. Fagan, "Time synchronization algorithms for IEEE 802.11 OFDM systems," *IET Conference Publications*, vol. 2009, no. 562 CP, pp. 287–290, 2009.

[87] M. Morelli, C.-C. J. Kuo, and M.-O. Pun, "Synchronization techniques for orthogonal frequency division multiple access (ofdma): A tutorial review," *Proceedings of the IEEE*, vol. 95, no. 7, pp. 1394–1427, 2007.

[88] M. Shaw and M. Fairchild, "Evaluating the 1931 cie color-matching functions," *Color Research & Application*, vol. 27, no. 5, pp. 316–329, 2002. [Online]. Available: https://onlinelibrary.wiley.com/doi/abs/10.1002/col.10077

[89] N. Murata, Y. Kozawa, and Y. Umeda, "Digital color shift keying with multicolor led array," *IEEE Photonics Journal*, vol. 8, no. 4, pp. 1–13, 2016.

[90] E. Monteiro and S. Hranilovic, "Design and implementation of color-shift keying for visible light communications," *Journal of Lightwave Technology*, vol. 32, no. 10, pp. 2053–2060, 2014.

[91] A. R. Ndjiongue, H. Ferreira, and A. H. Vinck, "Segmental analysis of the transmission in csk systems based on the euclidean distance," in *IEEE AFRICON 2015*, 09 2015.

[92] V. L. C. Association, "About vlca," https://j-photonics.org/vlca/en/vlca/, [Accessed 25-Jun-2023].

[93] R. D. Roberts, S. Rajagopal, and S.-K. Lim, "Ieee 802.15.7 physical layer summary," in *2011 IEEE GLOBECOM Workshops (GC Wkshps)*, 2011, pp. 772–776.

[94] N. Serafimovski, T. Baykas, V. Jungnickel, and H. Bims, "Status of ieee 802.11 light communication tg," https://www.ieee802.org/11/Reports/tgbb_update.htm, [Accessed 25-Jun-2023].

[95] I.-T. Recommendations, "High-speed indoor visible light communication transceiver - System architecture, physical layer and data link layer specification," https://www.itu.int/ITU-T/recommendations/rec.aspx?rec=13781, [Accessed 25-Jun-2023].

[96] J. Electronics and I. T. I. Association, "Av&it technology standardizationvisible light communications," https://www.jeita.or.jp/cgi-bin/standard_e/list.cgi?cateid=1&subcateid=50, [Accessed 25-Jun-2023].

[97] B. Lin, Z. Ghassemlooy, J. Xu, Q. Lai, X. Shen, and X. Tang, "Experimental demonstration of compressive sensing-based channel estimation for mimo-ofdm vlc," *IEEE Wireless Communications Letters*, vol. 9, no. 7, pp. 1027–1030, 2020.

[98] F. Miramirkhani and M. Uysal, "Channel modeling and characterization for visible light communications," *IEEE Photonics Journal*, vol. 7, no. 6, pp. 1–16, 2015.

[99] C. Chen, D. A. Basnayaka, X. Wu, and H. Haas, “Efficient analytical calculation of non-line-of-sight channel impulse response in visible light communications,” *Journal of Lightwave Technology*, vol. 36, no. 9, pp. 1666–1682, 2018.

[100] A. Yesilkaya, H. Abumarshoud, and H. Haas, *Optical Wireless Communications Using Intelligent Walls*. Wiley-IEEE Press, 2023, pp. 233–274.

[101] A. R. Ndjiongue, T. M. N. Ngatched, O. A. Dobre, and H. Haas, “Digital ris (dris): The future of digital beam management in ris-assisted owc systems,” *Journal of Lightwave Technology*, vol. 40, no. 16, pp. 5597–5604, 2022.

[102] P. Brandl, S. Schidl, A. Polzer, W. Gaberl, and H. Zimmermann, “Optical wireless communication with adaptive focus and mems-based beam steering,” *IEEE Photonics Technology Letters*, vol. 25, no. 15, pp. 1428–1431, 2013.

[103] Y. Kaymak, R. Rojas-Cessa, J. Feng, N. Ansari, M. Zhou, and T. Zhang, “A survey on acquisition, tracking, and pointing mechanisms for mobile free-space optical communications,” *IEEE Communications Surveys and Tutorials*, vol. 20, no. 2, pp. 1104–1123, 2018.

[104] M. E. Motamedi, *MOEMS: Micro-opto-electro-mechanical Systems*. SPIE press, 2005, vol. 126.

[105] H.-T. Chen, A. J. Taylor, and N. Yu, “A review of metasurfaces: physics and applications,” *Reports on Progress in Physics*, vol. 79, no. 7, p. 076401, jun 2016. [Online]. Available: https://dx.doi.org/10.1088/0034-4885/79/7/076401

[106] H. Wang, Z. Zhang, B. Zhu, J. Dang, L. Wu, and Y. Zhang, “Approaches to array-type optical irss: Schemes and comparative analysis,” *Journal of Lightwave Technology*, vol. 40, no. 12, pp. 3576–3591, 2022.

[107] M. Najafi and R. Schober, “Intelligent reflecting surfaces for free space optical communications,” in *2019 IEEE Global Communications Conference (GLOBECOM)*, 2019, pp. 1–7.

[108] R. Paschotta, *Field guide to lasers*. SPIE press Bellingham, WA, 2008, vol. 12.

[109] M. Najafi, B. Schmauss, and R. Schober, “Intelligent reflecting surfaces for free space optical communication systems,” *IEEE Transactions on Communications*, vol. 69, no. 9, pp. 6134–6151, 2021.

[110] H. Ajam, M. Najafi, V. Jamali, B. Schmauss, and R. Schober, “Modeling and design of irs-assisted multilink fso systems,” *IEEE Transactions on Communications*, vol. 70, no. 5, pp. 3333–3349, 2022.

[111] mirrorcle Technologies, "Integrated mems mirrors," https://www.mirrorcletech.com/wp/products/mems-mirrors/dual/integrated/, [Accessed 03-Jun-2023].

[112] E. W. Ng and M. Geller, "A table of integrals of the error functions," *Journal of Research of the National Bureau of Standards B*, vol. 73, no. 1, pp. 1–20, 1969.

[113] S. Schmid, T. Richner, S. Mangold, and T. R. Gross, "Enlighting: An indoor visible light communication system based on networked light bulbs," in *2016 13th Annual IEEE International Conference on Sensing, Communication, and Networking (SECON)*, 2016, pp. 1–9.

[114] M. Meucci, M. Seminara, T. Nawaz, S. Caputo, L. Mucchi, and J. Catani, "Bidirectional vehicle-to-vehicle communication system based on vlc: Outdoor tests and performance analysis," *IEEE Transactions on Intelligent Transportation Systems*, vol. 23, no. 8, pp. 11 465–11 475, 2022.

[115] C. Wang, H.-Y. Yu, and Y.-J. Zhu, "A long distance underwater visible light communication system with single photon avalanche diode," *IEEE Photonics Journal*, vol. 8, no. 5, pp. 1–11, 2016.

[116] S. Joumessi-Demeffo, S. Sahuguède, A. Julien-Vergonjanne, and P. Combeau, "Performance trade-offs of an optical wireless communication network deployed in an aircraft cockpit," *IEEE Open Journal of the Communications Society*, vol. 1, pp. 849–862, 2020.

[117] W. H. Gunawan, Y. Liu, C.-H. Yeh, and C.-W. Chow, "Color-shift-keying embedded direct-current optical-orthogonal-frequency-division-multiplexing (csk-dco-ofdm) for visible light communications (vlc)," *IEEE Photonics Journal*, vol. 12, no. 5, pp. 1–5, 2020.

[118] E. Monteiro and S. Hranilovic, "Design and implementation of color-shift keying for visible light communications," *Journal of Lightwave Technology*, vol. 32, no. 10, pp. 2053–2060, 2014.

[119] D. L. DiLaura and I. E. S. o. N. America, *The lighting handbook : reference and application*, 10th ed. New York, NY SE -: Illuminating Engineering Society of North America, 2011.

[120] OSRAM, "Luw-cn7n," https://look.ams-osram.com/m/70b541a08c64e64/original/LUW-CN7N.pdf, 2019.

[121] ——, "Luw-h9gp," https://look.ams-osram.com/m/579681cd0687ea48/original/LUW-H9GP.pdf, 2020.

[122] H. Elgala, R. Mesleh, and H. Haas, "An led model for intensity-modulated optical communication systems," *IEEE Photonics Technology Letters*, vol. 22, no. 11, pp. 835–837, 2010.

[123] E. Leitgeb, T. Plank, M. S. Awan, P. Brandl, W. Popoola, Z. Ghassemlooy, F. Ozek, and M. Wittig, "Analysis and evaluation of optimum wavelengths for free-space optical transceivers," in *2010 12th International Conference on Transparent Optical Networks*. IEEE, 2010, pp. 1–7.

[124] T. Instruments, "Lmh6703," https://www.ti.com/lit/gpn/lmh6703, 2005.

[125] T. Instruments, "Opa381," https://www.ti.com/lit/gpn/opa381, 2004.

[126] knight optical. Fresnel lens standard range 10mm f.l. x 13mmdia aperture. [Online]. Available: https://www.knightoptical.com/stock/default/fresnel-lens-standard-range-10mmf-lx13mmdia-aperture.html

[127] Y. Han, Y. Kim, and B. Kim, "Bit-shuffle coding for flicker mitigation in visible light communication," *IEEE Access*, vol. PP, pp. 1–1, 10 2019.

[128] B. ®, "Bluetooth core specification version 5.3," https://www.bluetooth.org/DocMan/handlers/DownloadDoc.ashx?doc_id=521059, 2021, [Accessed 27-Jul-2023].